# Feasibility Study on the Operation of an Iron Heat Treatment Furnace with Hydrogen Fuel

Muhammad Rasyid Salam

TUDelft

Witteveen+Bos

NEFIT INDUSTRIAL

# Feasibility Study on the Operation of an Iron Heat Treatment Furnace with Hydrogen Fuel

by

## Muhammad Rasyid Salam

in partial fulfilment of the requirements for the degree of

**Master of Science**

in Sustainable Energy Technology

at the Delft University of Technology,
to be defended publicly on Friday September 25, 2020 at 14:00 PM.

*This thesis is confidential and cannot be made public until Mar 25, 2021.*

An electronic version of this thesis is available at http://repository.tudelft.nl/.

**TUDelft**

i

# Abstract

The work presented in this report investigates the effect of replacing natural gas fuel in a radiant tube burner in an industrial furnace with hydrogen fuel. The flue gas is fully contained inside the radiant tube burner and does not come into contact with the iron products inside the furnace. The burner interacts with the process side of the furnace only by heat transfer. Therefore, the investigation could be divided into a study of two separate systems: the burner and the furnace systems. In the first part, the burner system was evaluated. The impact of changing the fuel of the burners from natural gas to hydrogen on heat-, flow- and radiation of the existing burner was studied. Moreover, the NOx generation has been considered. The investigations were performed using Reynolds Average Navier Stokes (RANS), Computational Fluid Dynamics (CFD) approach using detailed chemistry. Natural gas combustion was simulated as the basis for comparison. The result shows that the CFD model could estimate the NOx emission of the base case well. Next, the combustion with hydrogen was compared. The result suggests that the thermal efficiency of the burner is slightly higher with hydrogen fuel. On the other hand, the NOx emission is significantly higher. A modified burner including internal flue gas recycle was proposed and studied. The result shows that the modified burner can be operated at the same power and the same level of NOx emission as the existing system. Furthermore, different burner power could be applied in order to comply with the NOx emission limit or to increase processing speed. In the second part, a heat transfer analysis of the furnace has been performed. The model agrees well with measured data of furnace atmosphere temperature. The result suggests that having a higher burner power could increase the processing speed and reduce the energy requirement per ton of iron products.

# Acknowledgement

# Table of Contents

# List of Figures

# List of Tables

# List of Symbols

## Latin symbols

| | | |
|---|---|---|
| $L_c$ | characteristic length | m |
| $\mu$ | dynamic viscosity | Pa.s |
| $\nu$ | kinematic viscosity | $m^2/s$ |
| $Pr$ | Prandtl number | [-] |
| $Gr$ | Grashof number | [-] |
| $\beta$ | thermal expansion (the volumetric coefficient of expansion) | $K^{-1}$ |
| $\alpha$ | thermal diffusivity | $m^2/s$ |
| $\kappa$ | gray gas radiative absorption coefficients | $m^{-1}$ |
| $t$ | time dimension | s |
| $x$ | space dimension | m |
| $Y$ | species mass fraction | [-] |
| $J_I$ | diffusion flux of species I | m/s |
| $h$ | enthalpy | J |
| $\dot{Q}_r$ | radiative heat source term | J/s |
| $J_q$ | energy flux | $W/m^2$ |
| $T$ | temperature | K |
| $T_a$ | activation temperature | K |
| $p$ | pressure | Pa |
| $R_u$ | universal gas constant | $m^3\,Pa\,K^{-1}mol^{-1}$ |
| $W$ | Molecular weight | kg/mol |
| $k$ | turbulent kinetic energy | $m^2/s^2$ |
| $X$ | Mole fraction | [-] |
| $Z$ | mixture fraction | [-] |
| $P$ | probability density function | [-] |
| $c_p$ | specific heat capacity | kJ/kg-K |
| $E_a$ | activation energy | kJ/mol |
| $G$ | total incident radiation | $W/m^2$ |
| $a$ | absorption coefficient | $m^{-1}$ |
| $Re$ | Reynolds number | [-] |
| $A$ | area | $m^2$ |
| $F$ | radiation view factor | [-] |
| $\langle Nu \rangle$ | Nusselt number | [-] |

| | | |
|---|---|---|
| $D$ | diameter | m |
| $R_{fan}$ | fan rotation speed | rpm |
| $H$ | Height | m |
| $N_B$ | total number of burners | [-] |
| $N_W$ | total number of wall partition | [-] |
| $N_L$ | total number of loads | [-] |
| $Q$ | thermal energy (heat) | J |
| $\dot{Q}$ | Energy rate / power | J/s |
| $V$ | volume | m3 |
| $Nr$ | conduction – radiation number | [-] |
| $E_b$ | the total blackbody emissive power | W/m$^2$ |

## Greek symbols

| | | |
|---|---|---|
| $\rho$ | density | kg/m$^3$ |
| $u$ | velocity | m/s |
| $\tau_{ij}$ | viscous stress tensor | N/m$^2$ |
| $\dot{\omega}$ | Chemical source term | kg/m$^3$-s |
| $\mathcal{D}$ | mass diffusivity | m$^2$/s |
| $n_s$ | Number of species | [-] |
| $\lambda$ | thermal conductivity | W/m-K |
| $\alpha$ | Thermal diffusivity | m$^2$/s |
| $\phi$ | instantaneous quantity | |
| $\Phi$ | Equivalence ratio | [-] |
| $\delta_{ij}$ | kronecker delta | [-] |
| $\mu_t$ | turbulent viscosity | m$^2$/s |
| $Sc_t$ | turbulent Schmidt number | [-] |
| $Pr_t$ | turbulent Prandtl number | [-] |
| $Pr$ | Prandtl number | [-] |
| $\varepsilon$ | turbulent dissipation rate | m$^2$/s$^3$ |
| $\chi$ | Scalar dissipation rate | 1/s |
| $\xi$ | Conserved scalar | |
| $\Gamma$ | total species diffusion coefficient | kg/m-s |
| $\sigma$ | Stefan-Boltzmann constant | W/m$^2$K$^2$ |
| $\sigma_s$ | scattering coefficient | m$^{-1}$ |
| $\lambda$ | thermal conductivity | W/m-K |
| $\varepsilon_g$ | Emissivity of gas | [-] |

| $\dot{s}$ | volumetric rate of energy conversion | J/m3 |
| $\Delta V$ | finite volume | $m^3$ |
| $\varepsilon_r$ | emissivity | [-] |

## Subscript / Indices

| $I$ | species |
| $t$ | turbulent |
| $pos$ | load position in the furnace, position of atmosphere zone |
| $p$ | burner index |
| $q$ | wall index |
| $k$ | thermal conductivity |
| $r$ | radiant |
| $h$ | convective |
| $B$ | burner |
| $W$ | wall |
| $A$ | atmosphere |
| $L$ | load |

## Overbar symbols

| " | Fluctuations with respect to conditional mean |
| ' | Fluctuations with respect to unconditional mean |
| $\sim$ | Favre average |
| $-$ | Average |

# Acronym

| | |
|---|---|
| CFD | Computational Fluid Dynamics |
| GHG | Greenhouse gas |
| IEA | International Energy Agency |
| 2DS | 2-Degree Scenario |
| CCS | Carbon capture storage |
| GJMW | White-heart malleable iron |
| RANS | Reynolds Averaged Navier Stokes |
| RSM | Reynolds Stress Model |
| PDF | Probability Density Function |
| NOx | Nitric Oxide |
| RTE | Radiant Transfer Equation |
| WSSG | Weighted Sum of Gray Gases |
| EWT | Enhanced Wall Treatment |
| LHV | Lower Heating Value |
| FGR | Flue Gas Recycle |
| ODE | Ordinary Differential Equation |
| LNG | Liquefied Natural Gas |

# Introduction

In this chapter, the thesis is introduced by first describing the motivation of the work in the relation to sustainable energy technology development in Section 1.1. Then, the context of the problem is introduced in Section 1.2. Next, the research objectives are presented in Section 1.3. Finally, the report outline is described in Section 1.4.

## 1.1 Motivation: Decarbonizing the Industrial Sector

The industrial sector contributes to 35% of the world's total energy consumption in 2017 [1]. Due to the nature of the energy demand, the industrial sector is expected to have the least response to decarbonization compared to the other sectors. In many climate-friendly scenarios and projections, the greenhouse gas (GHG) emission of the industrial sector will not reduce as fast as the other sectors. A scenario made by International Energy Agency (IEA) in order to comply with a maximum 2°C increase in earth's temperature shows the most likely reduction in $CO_2$ emission per sector of energy consumption. Figure 1.1 presents the projected GHG emission by 2060 by this scenario. In this scenario, the power sector has been deeply decarbonized by 2060. Meanwhile, the contribution of the industry sector does not change considerably and becomes the sector with the largest source of GHG emissions.
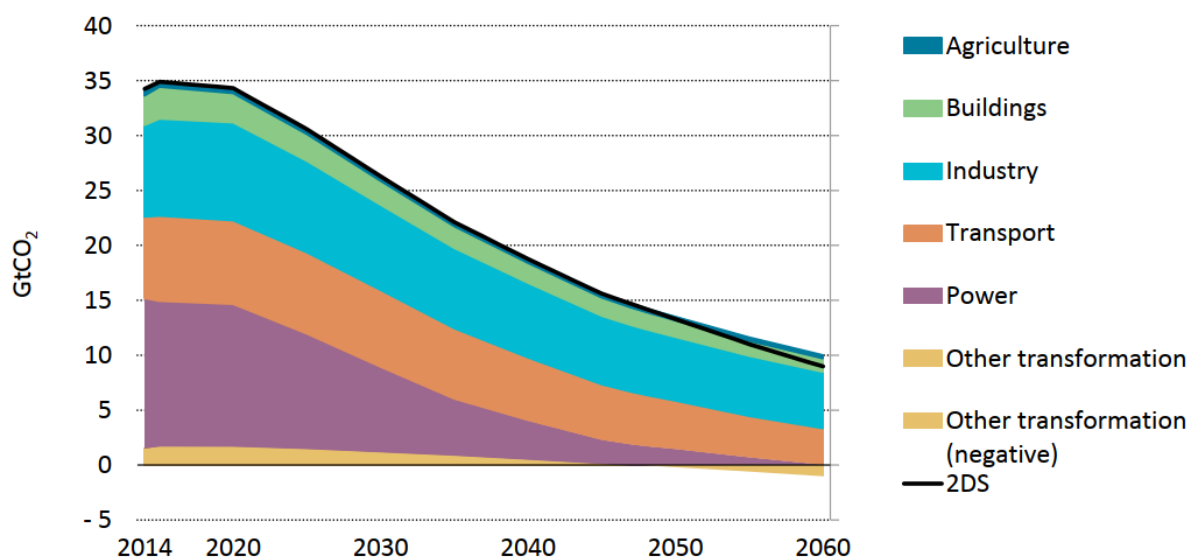


Figure 1.1: Remaining $CO_2$ emissions in the 2DS (2-Degree Scenario) by International Energy Agency (IEA). Note: solid-black line represents net $CO_2$ emissions [2]

### 1.1.1   The Challenge for Decarbonization of the Industrial Sector

The largest source of clean energy is expected to become available in the form of electricity from renewable energy. The availability of renewable electricity, however, varies greatly since it's largely dependent on weather conditions. This variation is a big challenge for the industry. The industrial sector does not have much room for flexibility to the variation in energy supply. Industries often have constant energy demand across the day and year. This is due to strict process requirements, which make it impossible to frequently shutdown and restart production. Furthermore, to be able to respond to the energy supply variation, over-design of equipment capacity is required, which is highly capital intensive. Besides that, the industrial sector is hard to decarbonize because of four technical reasons [3]:

- 45% of $CO_2$ emissions that result from feedstocks cannot be abated by the change in fuel, but only by changing the process.
- 35% of emissions come from the combustion of fossil fuels to generate high-temperature heat. Abating these emissions by switching to alternative greener fuels would be highly challenging, because this may require significant change to the furnace design.
- Industrial processes are highly integrated. Therefore, any change to one part of a process would affect other parts. Any change must be accompanied by changes to other parts of that process.
- Production facilities have long lifetimes, typically more than 50 years. Changing processes at existing sites requires costly retrofits or rebuilds.

In this study, the challenge of switching to one of the greener fuels for high-temperature heat (point 2) will be addressed. Three-quarters of energy used in the industry is in the form of heat. Around 30% of it is for low-temperature heating (below 150 °C), 22% for medium-temperature heating (150 – 400 °C), and 48% for high-temperature heating (above 400 °C). Therefore, the effort to tackle the challenge in high-temperature heat would have a significant impact on decarbonizing the industrial sector. Figure 1.2 visualizes the energy use of industry by the type.
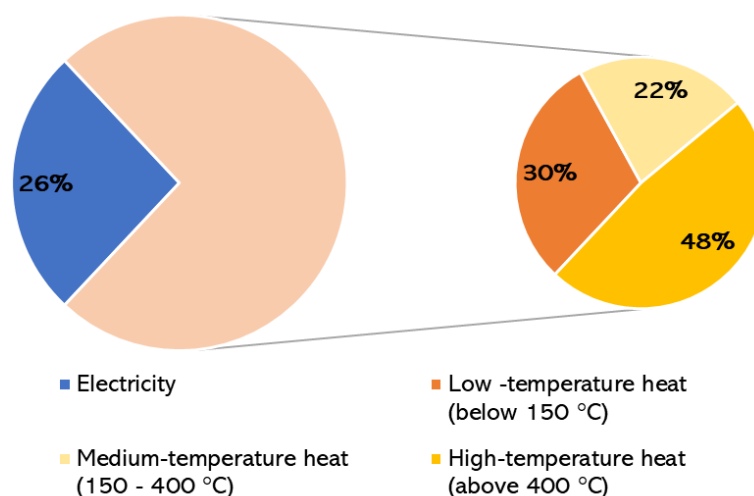


Figure 1.2: Heat represents three-quarters of industrial energy demand worldwide. High-temperature heat accounts for almost half of it. [2]

### 1.1.2 Hydrogen Role as the Fuel for High-Temperature Heat

Hydrogen is one of the solutions considered to substitute fossil fuel. This is due to the fact that generating energy from hydrogen fuel does not generate carbon dioxide. More importantly, hydrogen can be produced sustainably. There are three ways of production of hydrogen that are considered clean, namely:

1. **Green hydrogen production**. Hydrogen can be produced by electrolysis of water using green electricity. The hydrogen produced by this method is usually referred to as green hydrogen. The production by this method is expected to increase as more renewable energy power generations (e.g., solar panels, wind turbines) are installed. Conversion of the green power to hydrogen could accommodate the mismatch of energy supply and demand at a large scale. The production cost by this method is influenced by various technical and economic factors, with investment cost, conversion efficiency, electricity cost, and annual operating hours being the most important factors [4].

2. **Blue hydrogen production**. Blue hydrogen is the term used for the production of hydrogen from fossil fuels with the combination of CCS (carbon capture and storage). The carbon dioxide produced by this method is captured and prevented from being released to the atmosphere. The source of fossil fuels can be natural gas, oil, or coal. This production method can be a temporary solution to accommodate the transition to a more sustainable energy source.

3. **Production from Biomass**. Hydrogen can be produced from biomass in different ways, with anaerobic digestion and thermochemical gasification being the most popular. In the anaerobic digestion process, organic materials are processed by microorganisms to produce biogas or a combination of acid, alcohols, and gases (fermentation). In thermochemical gasification, biomass is converted at elevated temperature into a mix of carbon dioxide, carbon monoxide, hydrogen, and methane. In all cases, the produced gas would need to be further processed to extract the hydrogen. The complex processing of biomass makes it generally a more expensive method to produce low-carbon hydrogen than the other methods [4].

Amongst the fossil fuels, natural gas is the most logical fuel to be substituted with hydrogen since both are in the gas form at room conditions. The substitution may, however, require changes on the burner or furnace design, as the fuel properties are different. The properties of hydrogen and its comparison to natural gas are shown in Table 1.1. The properties of natural gas may vary as the composition of natural gas differs per production location. But, in all cases, methane is the largest component.

Table 1.1: Physical properties of hydrogen and its comparison to natural gas [4]

| Property | Hydrogen | Comparison to natural gas |
|---|---|---|
| Density (gaseous) | 0.089 kg/m3 (0°C, 1 bar) | 1/10 of natural gas |
| Density (liquid) | 70.79 kg/m3 (-253 °C, 1 bar) | 1/6 of natural gas |
| Boiling point | -252.76 °C (1 bar) | 90 °C below LNG |
| Energy per unit of mass (LHV) | 120.1 MJ/kg | 2.5 of natural gas |
| Energy density (ambient cond., LHV) | 0.01 MJ/L | 1/3 of natural gas |
| Specific energy (liquefied, LHV) | 8.5 MJ/L | 1/3 of LNG |
| Flame velocity | 346 cm/s | 8x methane |
| Ignition rate | 4 – 77 % in air by volume | 6x wider than methane |
| Autoignition temperature | 585 °C | 580 °C |
| Ignition energy | 0.02 MJ | 1/10 of methane |

## 1.2 Case Study: Hydrogen for High-Temperature Heating in a Foundry

To understand the challenge of switching from fossil fuel to hydrogen for high-temperature heating in an industrial application, a case study has been selected. The study focusses on the hydrogen application for high-temperature heating in the iron and steel industry. This study specifically investigates the case to switch natural gas into hydrogen for heat-treatment furnaces at Nefit Industrial, a foundry in Deventer. In this study, hydrogen will be evaluated as the replacement for natural gas for a heat treatment furnace. There are three heat treatment furnaces in the facility, and they contribute to more than 50% of the $CO_2$ emission in the factory. It is expected that the regulatory demands for reducing these emissions will increase in the coming years.

### 1.2.1 General Process at Nefit Industrial

The iron and steel industry is highly energy-intensive. Figure 1.3 shows the key process steps of steelmaking. The foundry industry is distinctive from the steel industry, in which it does not start with iron ore, but instead from the pig iron and scraps.
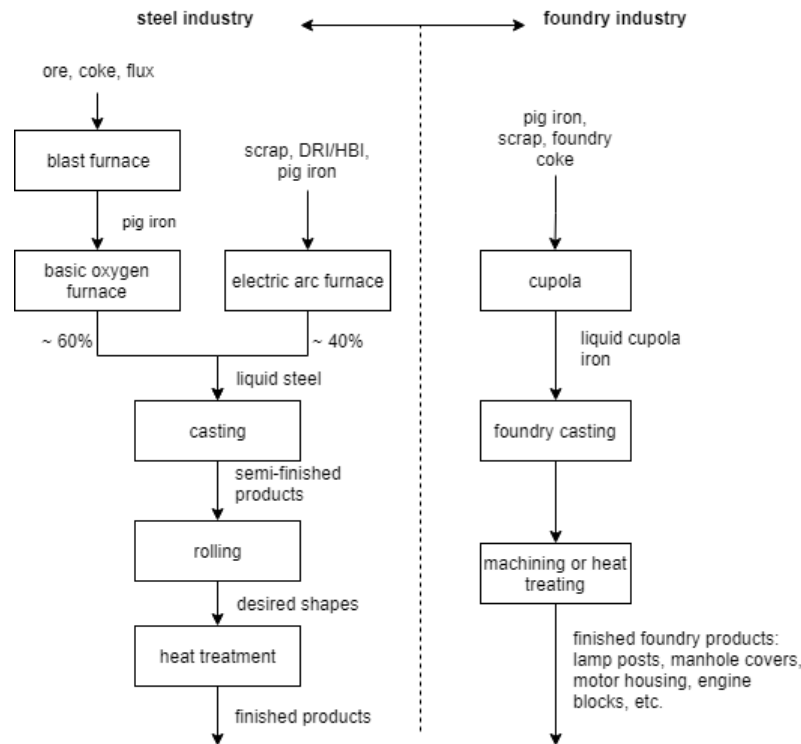
Figure 1.3: Key process steps of steelmaking [5]

Nefit Industrial is the industrial supplier of serial castings in white-heart malleable cast iron (also known as GJMW according to DIN EN 1562 standard). The range of casting products serves the automotive, building, heating, agricultural, installation, and utility industries. The white-heart malleable cast iron production has a specific process and material addition that distinguishes it from other types of cast irons. It has different properties compared to other types of cast irons. Malleable iron is used in applications where ductility and toughness are important [6]. Figure A.2 presents the basic differentiation of processing to obtain different types of cast irons, including white-heart malleable iron.

In Nefit Industrial, the process starts by melting the pig iron and recycled steel in a cupola furnace. The cupola furnace uses cokes as the energy source. The melted steel is then poured into molds made from sand. The molded steel is then cooled by air as it moves to the next process. In the next process, any excess steel is removed by grinding. Then, the steel product goes into a heat-treatment process. The heat-treatment process is necessary to improve the weldability of the steel products. After the heat-treatment process, the products are further processed by sharpening, polishing, and stamping. The products are then stored in a temporary warehouse before being transferred to another processing facility. In this facility, the products are machined, assembled, and prepared for delivery to customers. Figure 1.4 presents the block flow diagram at Nefit Industrial.
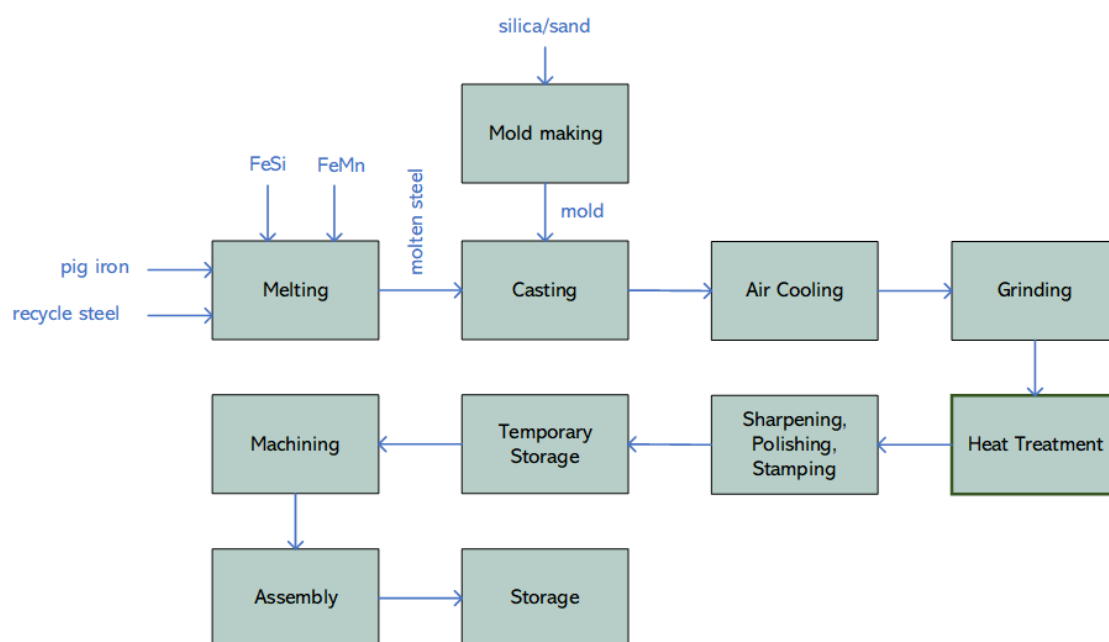
Figure 1.4: Block Flow Diagram (BFD) at Nefit Industrial

### 1.2.2  Potential Hydrogen Application on the Heat Treatment Furnaces

In Nefit Industrial, the heat treatment process is the biggest energy consumer. It accounts for 37% of the total energy consumption. In the heat treatment furnace, the iron products are processed at high temperatures inside the furnaces. The furnaces use natural gas as fuel. One of the furnaces uses natural gas and electricity for a lower temperature requirement. Further details on the heat treatment process are presented in Chapter 2. The replacement of natural gas into sustainable hydrogen would have a significant impact on reducing total emissions by the company. There are, of course, other less costly options that would also reduce the emissions. For example, applying energy-saving measures and producing green electricity with solar PV. However, with only these options the company would not achieve deep decarbonization at the scale corresponding to the high-temperature heat requirements.

### 1.2.3  Heat Treatment Process

The high-temperature heating in the heat treatment process is the focus of the study. This process is necessary to treat white cast iron into white-heart malleable iron with several different structures. An explanation of the metallurgical process occurring in the furnace is presented in Appendix A. The process is performed in furnaces with several burners. The burners used in the furnaces are a type of radiant tube burner. In this way, there's no direct contact between the flue gas and the product. Only heat is transferred from hot combustion products from the burner interior to the furnace. Figure 1.5 shows the inside view of the furnace.
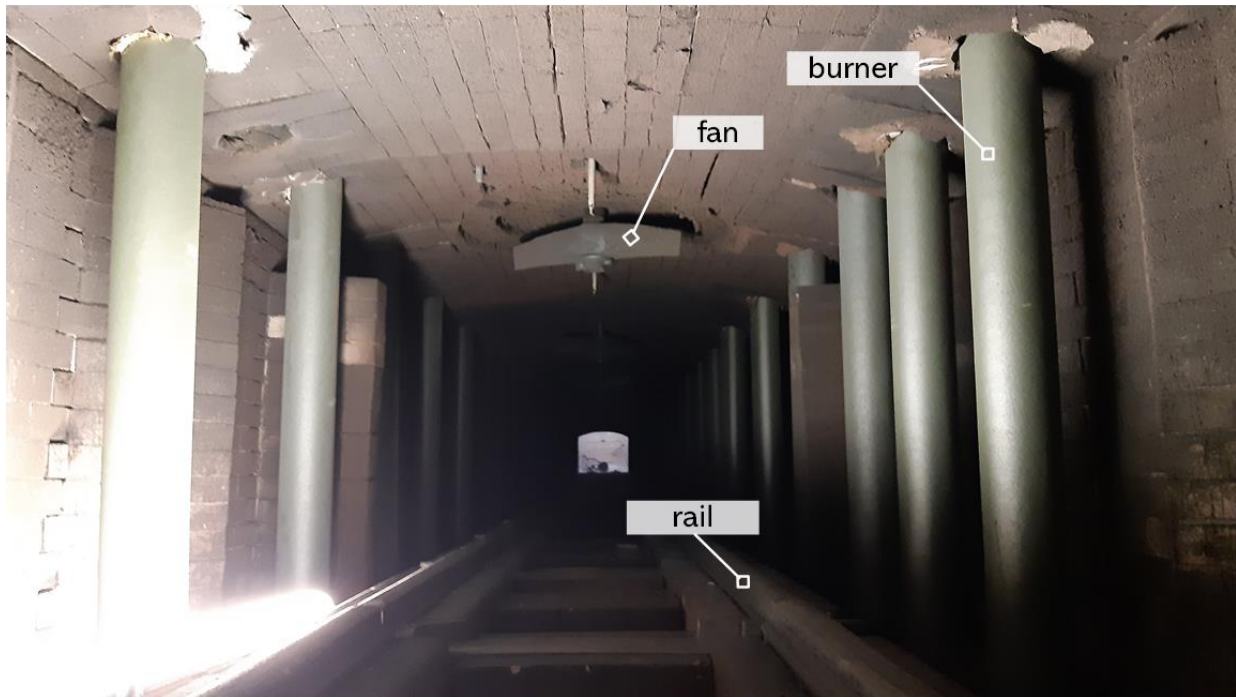
Figure 1.5: Inside view of the heat treatment furnace

As shown in Figure 1.5, there's a rail for which the product moves position. The iron products are contained in a basket or crate as shown in Figure 1.6. In the furnace, fans are available to circulate a controlled atmosphere environment. There are multiple burners installed vertically in the furnace. The burner has a non-circulating firing system and a single-ended design. Figure 1.7 shows the cross-section view of a burner. The non-circulating type is the most common radiant burner design. The distinguishing feature of this system is that the flue gas makes only a single pass through the tube. Compared to a circulating type system, the temperature profile in the non-circulating type generally is less evenly distributed. Therefore, with the same burner power, it has a higher local maximum temperature than the circulating type. Non-circulating pipe radiant tubes need a proper burner design to distribute heat more uniformly over the surface of the tube [7].



Figure 1.6 A basket of heat-treated GJMW just coming out the furnace. Source: Nefit Industrial

To increase energy efficiency, the burner includes a heat exchanger in which the heat from flue gas is recovered and transferred to the incoming air. Because the heat is recuperated in the same burner that produced the heat, it is called a self-recuperative burner. The burner has a 'single-ended design' with flue gas making a 180-degree bend. This makes it directly possible to use a counter-current heat exchanger between the flue gas and air. The heat exchangers transfer the heat from the flue gas into the secondary airflow.
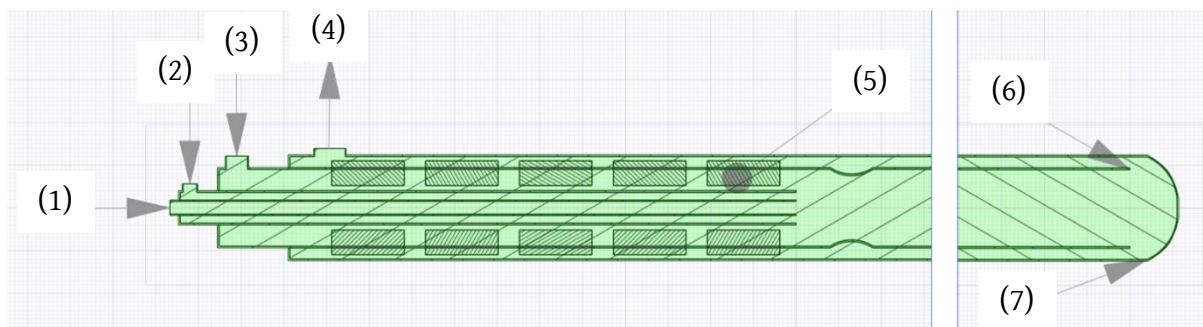


Figure 1.7: The burner geometry. (1) fuel inlet, (2) primary air inlet, (3) secondary air inlet, (4) flue gas outlet, (5) heat exchanger's fin, (6) inner tube, (7) outer radiant tube

## 1.3  Research Objectives

The main objective of this study is to investigate whether an industrial heat-treatment furnace can be operated with hydrogen fuel by simply replacing natural gas as the fuel, therefore minimizing the investment cost to switch into a clean energy option. To achieve the main objective, several sub-questions are formulated:

1. What are the effects of replacing hydrogen use on an existing burner designed for natural gas in terms of heat, flow, and radiation distribution?

2. How does the fuel efficiency and NOx emission on hydrogen combustion compare to the existing conditions?

3. How effective is a flue gas recycling technique to be applied for burner modification in reducing NOx emission?

4. How does the difference in heat flux supplied from burners affect the furnace performance and temperature profile of the product in the heat treatment furnace?

## 1.4  Report Outline

To answer the research questions, a CFD modeling was performed on the combustion of hydrogen in the radiant tube burner. The base case of natural combustion was also simulated for comparison. The theoretical background supporting the CFD modeling of the combustion is presented in Chapter 2. Next, In Chapter 3, the description of the CFD model development is presented. The result of the burner simulation is presented in Chapter 4. The result for a proposed burner modification on NOx emission is discussed as well. Next, an evaluation of the effects on burner heat flux to the product temperature and furnace performance is discussed in Chapter 5. Finally, the conclusion and recommendations are presented in Chapter 6.

# Theoretical Background

The aim of this chapter is to introduce the theory related to modeling of combustion in a Computational Fluid Dynamics (CFD) model. Combustion phenomena on a length and time scale can be described by transport equations of reactive flows. In Section 2.1, the theory for simulation of reactive flows is presented. Then, in Section 2.2, the Reynolds-averaged Navier–Stokes (RANS) model is introduced as a lower computational load alternative to the instantaneous transport equations. The RANS model leads to 'unclosed' term and require a turbulent viscosity model or Reynolds stress model (RSM) and closure of mean source term due to chemical reactions. In Section 2.3 the turbulence model is discussed. The closure of the reaction term, a turbulence-chemistry interaction, is explained in Section 2.4. As Nitric Oxide (NO) formation is considered in this study, the related theory is presented in Section 2.5. Next, radiative heat transfer and an approximate model to obtain a solution of the radiative transfer equation are presented in Section 2.6. The theory provided here is compiled based on [8], [9], [10], and [11].

## 2.1  Simulation of Reactive Flows

Combustion, as a chemically reactive flow phenomenon, can be described by a set of coupled partial differential equations that describe the conservation of mass, momentum, and energy. For a compressible flow, the mass and momentum conservation equations can be written as

Mass conservation equation:

$$\frac{\partial \rho}{\partial t} + \frac{\partial \rho u_j}{\partial x_j} = 0 \qquad \text{Eq. 1}$$

Momentum equation:

$$\frac{\partial}{\partial t}(\rho u_i) + \frac{\partial}{\partial x_j}(\rho u_i u_j) = -\frac{\partial p}{\partial x_i} + \frac{\partial \tau_{ij}}{\partial x_j} \qquad \text{Eq. 2}$$

The first term of Eq. 2 describes the local rate of change of momentum, and the second term is the momentum advection.

Reactive flow involves more than one component, therefore mass conservation for each species is applied. The equation for each species I, $Y_I$ , can be written as,

$$\frac{\partial}{\partial t}(\rho Y_I) + \frac{\partial}{\partial x_j}(\rho u_j Y_I) = -\frac{\partial J_{I,j}}{\partial x_j} + \dot{\omega}_I \qquad \text{Eq. 3}$$

$J_{I,j}$ is the diffusion flux of species I, and is defined as $-\rho \mathcal{D}_{Y_I} \frac{\partial Y_I}{\partial x_j}$, where $\mathcal{D}_{Y_I}$ is the diffusion coefficient of species I into the rest of the gas mixture. The last term on the equation, $\dot{\omega}_I$, is the volumetric reaction rate of species I.

There are several ways to describe the energy conservation. For convenience, here, it is described as a transport equation for enthalpy. The equation is:

$$\frac{\partial}{\partial t}(\rho h) + \frac{\partial}{\partial x_j}(\rho u_j h) = \frac{Dp}{Dt} + \tau_{ij} \frac{\partial u_i}{\partial x_j} - \frac{\partial J_{q,j}}{\partial x_j} + \dot{Q}_r \qquad \text{Eq. 4}$$

where $\dot{Q}_r$ is the radiative heat source term and $J_{q,j}$ is the energy flux. The energy flux is heat flux by conduction and heat flux by species interdiffusion:

$$J_{q,j} = -\lambda \frac{\partial T}{\partial x_i} + \sum_{I=1}^{n_s} h_I J_{I,j} \qquad \text{Eq. 5}$$

To completely describe the multicomponent system, the multicomponent ideal gas thermodynamics equation of state is required to obtain density as a function of other thermodynamics variables,

$$\rho = \frac{p}{R_u T} \left( \sum_{I=1}^{n_s} \frac{Y_I}{W_I} \right)^{-1} \qquad \text{Eq. 6}$$

The above instantaneous balance equations (Eq. 1, Eq. 2, Eq. 3, Eq. 5) are valid for all flow regimes, from laminar to turbulent. Unfortunately, the direct solution of the above equations, referred to DNS, requires high computational resources, and in engineering applications to reduced computational cost has to be replaced by a statistical approach based on averaging of the equations.

## 2.2   Reynolds Averaged Navier-Stokes (RANS) method

Averaging of the equations leads to equations for mean values. Reynolds-averaged Navier-Stokes (RANS) method use ensemble averaging which for statistically steady flows can be considered to be time-averaging. However this averaging also leads to several new or 'unclosed' terms[8] in the mean equations. Conceptually all the vector, scalar, and tensor quantities are considered to be the sum of the mean and a fluctuating component. In combustion applications, it is convenient to use density-weighted averages also called Favre averages. Any instantaneous quantity ($\phi$) is decomposed into its Favre average ($\tilde{\phi}$) and fluctuations about Favre average ($\phi''$) as

$$\phi = \tilde{\phi} + \phi'' \qquad \text{Eq. 7}$$

The main advantage of using Favre averages is that correlations with the density are zero and will not lead to unclosed terms in the equations: $\overline{\rho \phi''} = 0$.

Averaging of the instantaneous transport equations (Eq. 1, Eq. 2, Eq. 3, Eq. 5), using the Favre-averaging method, leads to the Favre average conservation equations as shown in Eq. 4 to Eq. 11.

Mean mass conservation equation:

$$\frac{\partial \bar{\rho}}{\partial t} + \frac{\partial \bar{\rho}\widetilde{u}_i}{\partial x_i} = 0$$

Eq. 8

Mean momentum conservation equation:

$$\frac{\partial}{\partial t}(\bar{\rho}\widetilde{u}_i) + \frac{\partial}{\partial x_i}(\bar{\rho}\widetilde{u}_i\bar{u}_j) = -\frac{\partial \bar{p}}{\partial x_i} + \frac{\partial \bar{\tau}_{ij}}{\partial x_i} - \frac{\partial}{\partial x_j}\left(\widetilde{\bar{\rho}u_i''u_j''}\right)$$

Eq. 9

Mean species transport equation:

$$\frac{\partial}{\partial t}(\bar{\rho}\widetilde{Y}_I) + \frac{\partial}{\partial x_j}(\bar{\rho}\widetilde{u}_j\widetilde{Y}_I) = \frac{\partial}{\partial x_j}\left(\overline{\rho\mathcal{D}\frac{\partial Y_I}{\partial x_J}}\right) - \frac{\partial\left(\widetilde{\bar{\rho}u_j''Y_I''}\right)}{\partial x_j} + \overline{\dot{\omega}_I}$$

Eq. 10

Mean enthalpy transport equation:

$$\frac{\partial}{\partial t}(\bar{\rho}\widetilde{h}) + \frac{\partial}{\partial x_j}(\bar{\rho}\widetilde{u}_j\widetilde{h}) = \frac{D\bar{p}}{Dt} + \frac{\partial}{\partial x_j}\left(\overline{\rho\mathcal{D}\frac{\partial h}{\partial x_J}}\right) - \frac{\partial(\widetilde{\bar{\rho}u_j''h''})}{\partial x_j} + \overline{u_J\frac{\partial\tau_{IJ}}{\partial x_J}} + \bar{\dot{Q}}$$

Eq. 11

$\bar{\tau}_{ij}$ in Eq. 9 is the mean viscous tensor and is given by

$$\bar{\tau}_{ij} = \mu\left(\frac{\partial\widetilde{u}_i}{\partial x_j} + \frac{\partial\widetilde{u}_j}{\partial x_i} - \frac{2}{3}\frac{\partial\widetilde{u}_k}{\partial x_k}\delta_{ij}\right)$$

Eq. 12

The Favre-averaging yields several unclosed terms in the above equations. The first one is $\left(\widetilde{\bar{\rho}u_i''u_j''}\right)$ in the momentum equation, also known as Reynolds stress term (RSM). In species and energy equations, the unclosed terms are $\left(\widetilde{\bar{\rho}u_i''Y_j''}\right)$ and $\left(\widetilde{\bar{\rho}u_i''h_j''}\right)$, respectively. The closure of these terms is discussed in Section 3.3. The last term in the species transport equation is the mean source term due to chemical reactions. The closure of this term is discussed in Section 3.4.

## 2.3 Turbulence Modeling

The Reynolds stress term (RSM) in the Favre averaged momentum equation needs to be closed by using turbulence models. Using the turbulence viscosity assumption proposed by Boussinesq [12], Reynolds stress$\left(\widetilde{\bar{\rho}u_i''u_j''}\right)$ can be described using viscous stress tensor $\tau_{ij}$ as

$$-\bar{\rho}\widetilde{u_i''u_j''} = \mu_t\left(\frac{\partial\widetilde{u}_i}{\partial x_j} + \frac{\partial\widetilde{u}_j}{\partial x_i} - \frac{2}{3}\delta_{ij}\frac{\partial\widetilde{u}_k}{\partial x_k}\right) + \frac{2}{3}\bar{\rho}\widetilde{k}\delta_{ij}$$

Eq. 13

Here, $\widetilde{k}$ is Favre-averaged turbulent kinetic energy and is equal to $\frac{1}{2}\widetilde{u_i''u_j''}$. The turbulent viscosity $\mu_t$ can be obtained by three different types of approaches, depending on how many differential equations are added to solve for turbulence quantities: zero-equation model (or algebraic model), one equation model, or two-equation model.

The other two unclosed terms, the turbulent fluxes of scalars ($-\bar{\rho}\widetilde{u_j''Y_I''}$ and $-\bar{\rho}\widetilde{u_j''h}$), are usually solved using classical gradient assumption. They are given in Eq. 14 and Eq. 15.

$$-\bar{\rho}\widetilde{u_i''Y_r''} = -\frac{\mu_t}{Sc_t}\frac{\partial \widetilde{Y_k}}{\partial x_j}$$

<div align="right">Eq. 14</div>

$$-\bar{\rho}\widetilde{u_i''h} = -\frac{\mu_t}{Pr_t}\frac{\partial \widetilde{Y_k}}{\partial x_j}$$

<div align="right">Eq. 15</div>

where $Sc_t$ and $Pr_t$ are the turbulent Schmidt number and turbulent Prandtl number, respectively, which are model constants.

## k −ε Turbulence Model

k –ε turbulence model is a two-equation turbulence model. This model is the most widely-used turbulence model in Computational Fluid Dynamics (CFD) for industrial flow simulations [11]. This two-equation model describes the turbulence based on two quantities, which are turbulent kinetic energy (k) and turbulent dissipation rate (ε). In this model, the turbulent viscosity is based on these two quantities and is given by equation Eq. 16.

$$\mu_t = \rho C_\mu \frac{k^2}{\varepsilon}$$

<div align="right">Eq. 16</div>

Additional transport equation for $\tilde{k}$ and $\tilde{\varepsilon}$ needs to be solved. The turbulent kinetic energy equation is:

$$\frac{\partial \bar{\rho}\tilde{k}}{\partial t} + \frac{\partial(\bar{\rho}\widetilde{u_j}\tilde{k})}{\partial x_j} = \frac{\partial}{\partial x_j}\left[\left(\mu + \frac{\mu_t}{\sigma_k}\right)\frac{\partial \tilde{k}}{\partial x_j}\right] + P - \bar{\rho}\tilde{\varepsilon}$$

<div align="right">Eq. 17</div>

Dissipation rate of the turbulent kinetic energy equation:

$$\frac{\partial \bar{\rho}\tilde{\varepsilon}}{\partial t} + \frac{\partial(\bar{\rho}\widetilde{u_j}\tilde{\varepsilon})}{\partial x_j} = \frac{\partial}{\partial x_j}\left[\left(\mu + \frac{\mu_t}{\sigma_\varepsilon}\right)\frac{\partial \tilde{\varepsilon}}{\partial x_j}\right] + C_{\varepsilon 1}\frac{\tilde{\varepsilon}}{\tilde{k}}P - C_{\varepsilon 2}\bar{\rho}\frac{\tilde{\varepsilon}^2}{\tilde{k}}$$

<div align="right">Eq. 18</div>

where $P$ is the production of turbulent kinetic energy due to the mean velocity gradient and is defined as:

$$P = -\bar{\rho}\widetilde{u_i''u_j''}\frac{\partial \widetilde{u_i}}{\partial x_j}$$

<div align="right">Eq. 19</div>

The k-ε model involves several model constants. The constants are tabulated in Table 2.1.

Table 2.1: Model constant values used in the standard k-ε turbulence model [11]

| Constant | $C_\mu$ | $C_1$ | $C_2$ | $\sigma_k$ | $\sigma_\varepsilon$ | $\kappa$ |
|----------|---------|-------|-------|------------|----------------------|----------|
| Value    | 0.09    | 1.44  | 1.92  | 1.0        | 1.3                  | 0.4187   |

## 2.4    Modeling of Turbulence-Chemistry Interaction.

In turbulent combustion, the mixing of reactants has to occur before they can react. The mixing is done by turbulent advection. Shear and strain at the interface during the breakup of developed eddies promote the mixing. Concentration gradients are developed and that causes an increase in molecular mixing between the reactants at the interface of smaller eddies.

In the transport equation of species mass fractions (Eq. 10), there is a mean chemical rate term $\dot{\omega}_I$. The closure of the term is rather difficult due to its non-linear dependency on temperature and species concentration. Several turbulent combustion models have been developed in the past based on estimates of timescales of mixing and reaction and using statistical approaches. Here we shall use an approach based on a scalar describing the mixing between fuel and air (mixture fraction) and an assumed probability density function (PDF), but enabling the representation of detailed finite rate chemistry effects.

## Presumed PDF Approach with Finite Rate Chemistry.

The presumed PDF approach uses a mixture fraction concept which reduces a turbulent non-premixed flame to a mixing problem coupled to a universal local flame structure. A sub-model is needed to describe the local flame structure as a function of a variable describing the presence of mass from fuel and oxidizer streams (mixing). The mixture fraction $Z$ represents the mass fraction of fluid at a particular location that originated from the fuel stream. The pure fuel stream has a value of 1, and the pure oxidant stream has a value of 0. In turbulent flow also the mixture fraction is fluctuating. Knowing only the mean value of mixture fraction is not sufficient because species concentrations and temperature depend in a nonlinear way on mixture fraction. A common way to handle the fluctuations of mixture fraction is as follows. The probability that Z takes a value between two possible values z and $z + dz$ is $P(z)dz$ where P is the probability density function [11].

The Favre mean mass fraction and Favre mean temperature at any location in space where the PDF is known, are exactly given by integration over all mixture fraction values with the $\beta$-function as weight factor:

$$\tilde{Y} = \int Y(z)\, P(z) dz \qquad \text{Eq. 20}$$

$$\tilde{Y} = \int Y(z)\, P(z) dz \qquad \text{Eq. 21}$$

$$\tilde{T} = \int T(z)\, P(z)\, dz \qquad \text{Eq. 22}$$

The way to obtain the PDF is explained below. Different possible assumptions can be made for the local flame structure appearing in the integral. The simplest possibility is infinitely fast chemistry leading to thermochemical equilibrium. This does not allow the representation of kinetic effects. More realistic are models using a local flame structure where both diffusion and reaction play a role, which is described next.

## Flamelet Model

In the counterflow laminar diffusion flame model, the local state is assumed to be arising in a head-on counterflow of a fuel stream and an air (or more generally 'oxidant') stream.

The flamelet equations describing the local state are given by

$$\rho \frac{\partial Y_k}{\partial t} - \rho \frac{\chi}{2} \frac{\partial^2 Y_k}{\partial \xi^2} - \dot{\omega}_k = 0 \qquad \text{Eq. 23}$$

and

$$\rho \frac{\partial T}{\partial t} - \rho \frac{\chi}{2} \frac{\partial^2 T}{\partial Z^2} + \sum_{k=1}^{N} \frac{h_k}{c_p} \dot{\omega}_k = 0$$

Eq. 24

To reach these equations a transformation of variables was necessary from spatial coordinates to mixture fraction Z and some approximations were made. The scalar dissipation rate appears in front of the second derivative and describes the strength of diffusion in the direction normal to the flame. At the air and fuel side of the flame (Z=0 and Z=1), the inflow conditions have to be specified. In steady-state, the transient term vanishes. Then the balance between diffusion in mixture fraction space and chemical reaction determines the flame structure.

Solving the steady flamelet equations gives a solution of scalar variables (temperature, concentrations) as a function of mixture fraction and scalar dissipation rate. This collection is known as a steady flamelet library. The library contains in tabulated form the scalar quantities (temperature, concentrations) as functions of the mixture fraction and scalar dissipation rate.

An extension is needed for the case with heat loss, e.g. by thermal radiation. Then the enthalpy deficit relative to the adiabatic case has to be provided. This can be done in several ways. The simplest is to lower the temperature of the solution but keeping the solution for species unchanged.

This concept enables the transformation of the entire chemistry of reaction in terms of mixture fraction and dissipation rate. This method avoids the calculation of transport equations for every single species. Thus, it reduces computational load considerably even with detailed chemistry involving many species.

The scalar dissipation rate has the units of frequency and characterizes the flow field in which the flame is arising. When the flamelet solution is used in turbulent flames the scalar dissipation rate has the interpretation of a parameter characterizing the level of turbulence, by the interpretation of the inverse of mixing time.

The flamelet model requires information on the value of mixture fraction and scalar dissipation rate and enthalpy to provide values of species and temperature. In the statistical description of turbulent flow using RANS, instantaneous values of mixture fractions are not computed, but in order to obtain the PDF, an equation for the Favre mean value of mixture fraction and the corresponding variance is solved. It is assumed that the probability density function of the mixture fraction has a certain mathematical form depending on two parameters. The most common form is that of $\beta$-function. The mean and the variance of the mixture fraction are two independent parameters together characterizing the PDF.

The flamelet model for turbulent non-premixed flames then solves the Favre-averaged transport equations of mixture fraction and its variance. The variance is denoted as $g = \widetilde{Z''^2}$ .

The steady-state transport equation Favre mean mixture fraction is given by

$$\frac{\partial}{\partial x_j} \left( \bar{\rho} \tilde{u}_j \ \tilde{Z} \right) = \frac{\partial}{\partial x_j} \left( \frac{\mu_t}{Sc_\xi} \frac{\partial \tilde{Z}}{\partial x_j} \right)$$

Eq. 25

Here, the first term of the equation is the turbulent flux of mixture fraction and the second term is the source term used in liquid fuel combustions due to interphase transport, which is not applicable for the present work. The transport equation for the mixture fraction variance is expressed as,

$$\frac{\partial}{\partial x_j}\left(\bar{\rho}\tilde{u}_j g\right) = \frac{\partial}{\partial x_j}\left(\frac{\mu_t}{Sc_t}\frac{\partial g}{\partial x_j}\right) + C_{g1}\mu_t\left(\frac{\partial \tilde{Z}}{\partial x_j}\right)^2 - \bar{\rho}\tilde{\chi}$$

Eq. 26

where $C_{g1}$ is a model constant with a standard value of 2.0. The last two terms on the right-hand side of the equation are the generation rate of mean mixture fraction variance and the rate of destruction of mean mixture fraction variance, respectively. By model assumption, it is proportional to the product of turbulence frequency of the turbulence model and the variance via Eq. 27.

$$\tilde{\chi} = c_\chi \frac{\tilde{\varepsilon}}{\tilde{k}} g$$

Eq. 27

where $c_\chi$ is a constant having a standard value of 2.0.

## 2.5  Formation of Nitric Oxide (NOx)

There are several mechanisms for the formation of Nitric Oxide ($NO_x$), which are thermal $NO_x$, prompt $NO_x$, Nitrous Oxide ($N_2O$) mechanism, and fuel generated $NO_x$. and fuel generated NOx is not applicable for this study since there is no nitrogen bound in the fuel. The $N_2O$ mechanism is not considered. It is significant in lean premixed combustion[9] but not here.

### Thermal NOx

Formation of NOx by a thermal mechanism can be described by these elementary reactions below [9][10]:

$$O + N_2 \underset{k_{r,1}}{\overset{k_{f,1}}{\rightleftarrows}} NO + N$$

Eq. 28

$$N + O_2 \underset{k_{r,2}}{\overset{k_{f,2}}{\rightleftarrows}} NO + O$$

Eq. 29

$$N + OH \underset{k_{r,3}}{\overset{k_{f,3}}{\rightleftarrows}} NO + H$$

Eq. 30

The values of the above rate constants which are used in ANSYS Fluent program for the above reactions are as follows:

$$k_{f,1} = 1.8 \times 10^8 e^{-38370/T} \qquad k_{r,1} = 3.8 \times 10^7 e^{-425/T}$$

$$k_{f,2} = 1.8 \times 10^4 e^{-4680/T} \qquad k_{r,2} = 3.81 \times 10^3 T\, e^{-20820/T}$$

15

$$k_{f,3} = 7.1 \times 10^7 e^{-450/T} \qquad\qquad k_{r,3} = 1.7 \times 10^8 e^{-24560/T}$$

Where $k_f$ is the reaction rate constant for a forward reaction and $k_r$ is the reaction rate constant for the backward reaction. The unit for these rate constants is m³/mol-s. These values are the result of numerous studies and have been selected in ANSYS Fluent based on an evaluation by Hanson and Salimian [13]. The first reaction (Eq. 28) has very high activation energy and therefore reacts efficiently fast only at high temperatures. The second reaction (Eq. 29) is has a significantly low rate constant and therefore is the rate-limiting step.

The rate of formation for the above reactions is:

$$\frac{d[NO]}{dt} = k_{f,1}[O][N_2] + k_{f,2}[N][O_2] + k_{f,3}[N][OH] - k_{r,1}[NO][N]$$
$$- k_{r,2}[NO][O] - k_{r,3}[NO][H]$$

Eq. 31

The above rate equation depends on the concentration of oxygen atom [O], hydrogen atom [H], nitrogen atom [N], and [OH]. For most of the combustion cases, [N] is in steady-state (rate of formation equal to the rate of destruction) due to fast reactions with other species and can be obtained from an algebraic relation[10]. The concentration of other species (O, H, and OH) is available from the solution of the flamelet equations for the main combustion process with detailed chemistry.

## Prompt NOx

This mechanism suggests that NOx is also generated promptly at the flame front resulting from radical CH. The radical CH is formed at the flame front only. It reacts with nitrogen from the air (oxidant), forming hydrocyanic acid (HCN), which reacts further to produce NO. [9]

$$CH + N_2 \rightarrow HCN + N \begin{array}{c} \nearrow \cdots \rightarrow NO \\ \searrow \cdots \searrow N_2 \end{array}$$
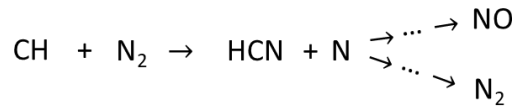
The activation energy of the reaction above is smaller (75 kJ/mol at $T_a \approx 9\,000$ K) compared to the formation of the thermal NO (318 kJ/mole at $T_a \approx 38\,200$ K); therefore, in contrast to thermal NO, prompt NO is also produced at relatively low temperatures (about 1000 K). [9]

The rate-limiting step, $CH + N_2 \rightarrow$ HCN + N, is not fully known. The accuracy of this prediction of prompt NO formation is at a factor of 2 [9]. The prompt NOx formation rate model in ANSYS Fluent is a modification from the model derived by De Soete [14], which includes correction factor f to incorporate the effect of fuel type (number of carbon atoms) and air to fuel ratio.

$$\frac{d[NO]}{dt} = f k_{pr}'[O_2]^a[N_2][FUEL]e^{-E_a'/RT}$$

Eq. 32

where:

$$f = 4.75 + 0.0819n - 23.2\phi + 32\,\phi^2 - 12.2\phi^3$$

Eq. 33

and

$$k'_{pr} = 6.4 \times 10^6 (RT/p)^{a+1}$$

Eq. 34

$E'_a$ is 303,474 J/mol. $a$ is the oxygen reaction order, R is the universal gas constant, and p is pressure (all in SI units). $k_{pr}$ depends on the fuel. n is the number of carbon atom in the fuel, and $\phi$ is the equivalence ratio. The correction factor is valid for alkanes and equivalence ratio between 0.6 – 1.6.


## Temperature and Composition Variance

In the present work, the RANS method is used to solve the turbulent combustion calculation. The resulted time-averaged composition and temperature are not valid to be employed to calculate the mean NOx formation rate. This is because the turbulent mixing process has temporal fluctuations in temperature and species concentration. Therefore, the fluctuation must be considered on the variables for NOx formation rate calculation. In this work, the probability density function (PDF) technique is used to evaluate the statistical averages of chemical quantities. The mean values of the independent variables needed for the PDF construction are obtained from the solution of the transport equations.

The PDF is used for weighting against the instantaneous rates of production of (Eq. 31 and Eq. 32) and subsequent integration over suitable ranges to obtain the mean turbulent reaction rate. Hence, we have:

$$\bar{S}_{NO} = \int \rho w_{NO}(V_1, V_2) \; P(V_1, V_2) \; dV_1 dV_2$$

Eq. 35

Where $V_1$ and $V_2$ are temperature and species concentrations. $P$ is the probability density function (PDF).

ANSYS Fluent can assume $P$ to be a two-moment beta function that is suitable for combustion calculations. The equation for the beta function is

$$P(V) = \frac{\Gamma(\alpha + \beta)}{\Gamma(\alpha)\Gamma(\beta)} V^{\alpha-1}(1 - V)^{\beta-1}$$

Eq. 36

$$P(V) = \frac{V^{\alpha-1}(1 - V)^{\beta-1}}{\int_0^1 V^{\alpha-1}(1 - V)^{\beta-1} dV}$$

Eq. 37

Where $\Gamma(\ )$ is the Gamma function, and $\alpha$ and $\beta$ depend on the mean value of the quantity in question, $\bar{m}$, and its variance, $\sigma^2$.

$$\alpha = \bar{m}\left(\frac{\bar{m}(1 - \bar{m})}{\sigma^2} - 1\right)$$

Eq. 38

$$\beta = (1 - \bar{m})\left(\frac{\bar{m}(1 - \bar{m})}{\sigma^2} - 1\right)$$

Eq. 39

The beta function requires the independent variable $V$ to have values between 0 and 1. Thus, field variables such as temperature must be normalized.

The variance $\sigma^2$ is based on an approximate form of the variance transport equation (also referred to as the algebraic form). For a PDF in terms of mixture fraction, the mixture fraction

variance has already been solved as part of the basic combustion calculation. Thus, no additional computation is required for $\sigma^2$.

## 2.6 Radiation Model

In order to calculate the radiative heat transfer, a model is needed for the radiative properties (absorption coefficient) and a method for solving the radiative transfer equations (RTE). In this work assume that the absorption coefficient is wavelength-independent (gray) and the P-1 model is used to solve the RTE. The P-1 model is the lowest order of a series of models called P-N. Here N is the order at which the solution of the equation in a series expansion in spherical harmonic functions is truncated. P-1 is a very popular method since it reduces the RTE equation to a relatively simple partial differential equation. The P-1 method is suitable for optically thick media. Optical thickness results in an angular distribution of intensity of radiation which is quite uniform. The P-1 method has three independent parameters to describe the angular dependence. In order to reach higher accuracy other more computationally intensive RTE solution methods are available such as the discrete ordinates method (DO) but these have not been used. Using a non-gray radiation model or using the DO for solving the RTE would lead to a different local distribution of radiation inside the radiant tube burner, but is expected not to make a significant difference for NOx formation or for the radiative heat transfer from burner to surroundings.

In the case of gray radiation, the equations of the P-1 model are as follows [15].

A general expression for the radiative source appearing in the energy equation is

$$-\nabla \cdot q_r = aG - 4an^2\sigma T^4 \qquad \text{Eq. 40}$$

Here $q_r$ is the radiative heat flux, G is the total incident radiation, $a$ is the absorption coefficient of the gas phase, n is the refractive index, σ is the Stefan-Boltzmann constant and T is the temperature. The expression for $-\nabla \cdot q_r$ substituted into the enthalpy equation providing for heat sources (or sinks) due to radiation that influences the local temperature.

In the P-1 model, the heat flux is related to the total incident radiation via

$$q_r = -\Gamma\nabla G \qquad \text{Eq. 41}$$

Where the coefficient Γ depends on the radiative properties of the medium

$$\Gamma = \frac{1}{(3(a + \sigma_s) - C\sigma_s)} \qquad \text{Eq. 42}$$

$\sigma_s$ is the scattering coefficient which can be taken zero in the natural gas and hydrogen flames considered here.

The following transport equation for G is obtained and added to the transport equations to be solved to describe the flow in the burner:

$$\nabla \cdot (\Gamma\nabla G) - aG + 4an^2\sigma T^4 = 0 \qquad \text{Eq. 43}$$

However, in the frame of a RANS approach, the averaged form of the P-1 model equation is used. A closure problem arises because the mean value of the fourth power of temperature is not equal to the mean temperature to the fourth power. In the approach used here this difference is

neglected. The inaccuracy of proceeding in this way is expected to be similar to the inaccuracy in using the P-1 model and a gray gas model and acceptable for the current application. An improvement could come by including a model for the so-called turbulence-radiation interaction.

## Weighted Sum of Gray Gases (WSSGs) Method

The above radiative equation requires a value for the fluid absorption coefficient. Its value depends on the concentration of the absorbing and emitting species $CO_2$ and $H_2O$ and the temperature. But it also depends on the size of the gas cloud. The radiation contribution from soot formation is not considered, since it is absent in hydrogen flames and very low in lean methane flames [11].

To handle this a standard approach described the gas as a mixture of a set of gray gases with different absorption coefficient. In this weighted sum of gray gases (WSSGs) method the total emissivity of the gas is obtained from the following correlation:

$$\varepsilon_g = \sum_j a_j (1 - e^{-\kappa_j p L})$$

Eq. 44

$p$ is the sum of the partial pressure of $CO_2$ and $H_2O$, L is the path length taken as the size of the domain and $\kappa_j$ are the gray gas radiative absorption coefficients. The coefficients $a_j$ are obtained in the form of polynomial functions of gas temperature. $\kappa_j$ and $a_j$ depends on the ratio of partial pressures $p_{H_2O}/p_{CO_2}$, see Smith et al. [25].

The total emissivity of a gas cloud by definition is the fraction of intensity that has been absorbed compared to the incoming intensity or also it is the fraction of intensity that is emitted compared to the maximum possible. The mean absorption coefficient to reach this emissivity is calculated by inverting Beer-Lambert law (describing exponential attenuation or growth),

$$\kappa_g = -\frac{1}{L} ln(1 - \varepsilon_g)$$

Eq. 45

The link between P-1 model and WSGG model then is that $a = \kappa_g$.

# Burner Model

In this chapter, a CFD model for the simulation of combustion in a radiant tube burner (RTB) is described. In general, the process flow for working on a CFD analysis is presented in Figure 3.1. The process starts with defining geometry in preprocessing step up to defining the model and analyzing the solution.

The combustion takes place inside the burner and is isolated from the furnace by the outer burner wall. Heat transfer occurs from a part of the burner outer wall to the iron product and the rest of the furnace. The burner's components, physical domain, and computational domain are introduced in Section 3.1. The boundary conditions are explained in the subsequent section. The mathematical model used for the CFD simulation is explained in Section 3.3. To solve transport equations, CFD simulation requires finite elements (mesh) generation in the computational domain to solve the associated equations. The mesh used for the simulation is presented in Section 3.4. In Section 3.5 the model is validated using measured data. Section 3.6 gives an overview of the simulated cases.
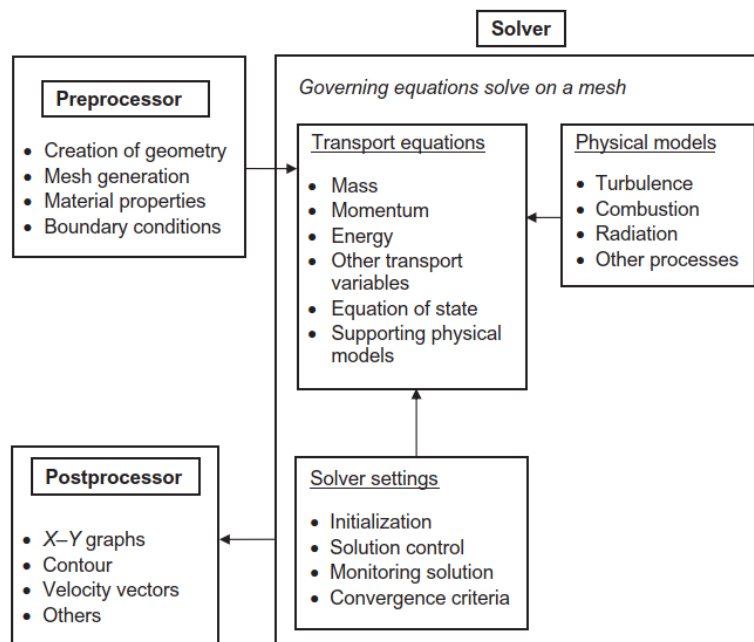


Figure 3.1: Three main elements within a CFD analysis framework.[16]

## 3.1 Burner Geometry

This work evaluates a single-ended and non-circulating type radiant tube burner (RTB). Single-ended radiant (SER) in combination with radiant tube burner are the most burner used in the European market [17]. On RTB, the combustion reactions occur inside the radiant tube. The burner has a heat recuperation section which enables the pre-heat of air (i.e. a self-recuperative type). The fuel and air are injected separately and meet at the combustion zone. This is known as a non-premixed combustion type. Figure 3.2 presents a schematic of the burner. The burner has two main zones: the heat recuperation zone and the combustion zone.

The recuperator is a counter-flow heat exchanger with fins to increase the heat transfer area. The combustion zone is composed of two concentric tubes. The outer tube has an outside diameter of 140 mm and a thickness of 10 mm. The inner tube has an inside diameter of 120 mm and a thickness of 6 mm. The burner is constructed from austenitic heat-resistance casting steel with GX40CrNiSi25-20 grade. The thermal properties of the material are tabulated in Table E.1 in Appendix E.
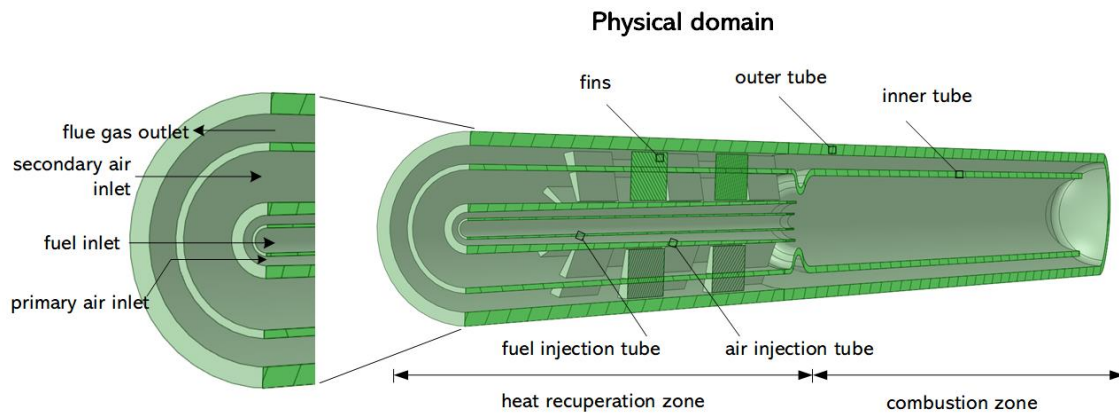


Figure 3.2: Schematic of the self-recuperative radiant tube burner (RTB) at Nefit Industrial.

The simulation applied a 2-dimensional (2D) computational domain with an axisymmetric model to reduce the computational cost. Figure 3.3 shows the computational domain. The fins in the heat recuperation zone are not represented well because of the 2D domain. However, the fins' heat exchange area is kept constant.
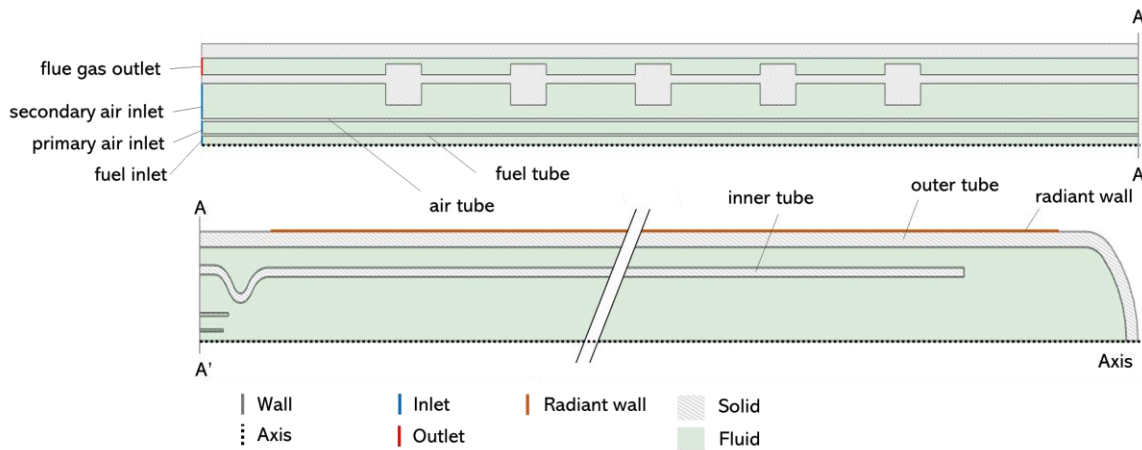
Figure 3.3: Computational domain for CFD model of the RTB

## 3.2 Boundary Conditions

The air and fuel inlets were defined as a velocity-inlet boundary condition, with a value vary depending on the case. The values of boundary conditions are discussed in Section 3.6. The thermal boundary condition for different wall surfaces was specified as follows. The wall interfaces between fluid and solid zones considered conjugate heat transfer. The radiant wall has an emissivity of 0.97 (Stainless steel GX40CrNiSi25-20 material [18]). It radiates heat to the products and walls inside the furnace. Most of the temperature in the furnace is maintained at 1323.15 K. The surface of the burner wall is significantly smaller than the surfaces it radiates to. Thus, the heat received by the burner from the surrounding is significantly smaller than the heat it radiates. Therefore, it can be neglected. The net heat transfer from the burner to the surrounding can be expressed as:

$$\dot{Q}_r = \sigma \, \varepsilon_B \, A_B \, (T_B{}^4 - T_s{}^4) \qquad \text{Eq. 46}$$

Where $T_B$ is the temperature of the burner's radiant wall and $T_s$ is the surrounding temperature (1323.15 K). $A_B$ and $\varepsilon_B$ are the surface area of the radiant wall and its emissivity, respectively.

In the heat treatment furnace, heat transfer to the load is mainly through radiation, therefore convection from the burner to the surrounding atmosphere is not considered in the wall boundary condition of the burner. Table 3.1 summarizes the boundary conditions. The rest of the wall boundaries are considered adiabatic.

Table 3.1: Boundary conditions of the RTB model

| Boundary | Type | Value |
|---|---|---|
| Fuel inlet | Velocity inlet | Case dependent |
| | | Composition of natural gas: 85% mole $CH_4$, 15% mole $N_2$ |
| | | Composition of hydrogen fuel: 100% H2. |
| Primary air inlet | Velocity inlet | Case dependent |
| Secondary air inlet | Velocity inlet | Case dependent |
| Flue gas outlet | Pressure outlet | Pressure: 0 barg |
| Radiant wall | Wall | Emissivity: 0.97, external temperature: 1232.15 K |

## 3.3  Mathematical model

The fluid dynamics are described by Reynolds Averaged Navier-Stokes (RANS) approach given in Chapter 2. The simulation used the double-precision solver based on the pressure of the commercial software ANSYS Fluent® 2019 R3 version.

### Momentum and energy

The Reynolds stress tensor in the RANS equations was calculated using the standard k-ε model. The Coupled and Standard algorithms were used for pressure-velocity coupling and pressure interpolation, respectively. The flow in the viscous region of the boundary layer near the walls was calculated using the Enhanced Wall Treatment (EWT) method. The mean enthalpy equation is solved with the radiative source term included. The radiative transfer equation providing this source term was solved using the P1 model in combination with a WSGGM for spectral properties.

### Combustion

Combustion was described by the steady flamelet model for non-premixed combustion. The flamelet table was generated using the Fluent code, including enthalpy loss as an independent variable. The final lookup table then has four independent variables, mean and variance of mixture fraction, strain rate, and scaled enthalpy loss.

### Kinetic mechanism

The combustion model requires a kinetic mechanism that describes the oxidation of the fuel. The kinetic mechanism used in this study was Li et al., [19] for hydrogen combustion and Shi et al., [20] for methane combustion. Both are detailed mechanisms.

A detailed reaction mechanism was chosen since NOx formation is considered in this work. There are several sets of the detailed kinetic mechanism of hydrogen combustion. O'Conaire et al [21], Li et al [19], Mueller et al [22], Shimizu [23] for high pressure application. Hong et al [24]. There are several mechanisms that involve hydrocarbon. The kinetic mechanism by Li et al has been validated against a wide range of experimental conditions and was found to be in good agreement with experimental data from shock tubes, laminar premixed flames, and flow reactors [19]. The parameters of

the Li et al mechanism for hydrogen-air combustion are listed in Table 3.2. Following standard convention the units of A are expressed in cm, mol and s and the unit of E is kJ/mol (the temperature exponent n is dimensionless).

Table 3.2 Detailed H2/O2 Reaction Mechanism [19]

| No. | Reaction | | A | n | E |
|---|---|---|---|---|---|
| | H2/O2 chain reactions | | | | |
| 1 | $H + O2 = O + OH$ | | $3.55 \times 10^{15}$ | -0.41 | 16.6 |
| 2 | $O + H2 = H + OH$ | | $5.08 \times 10^{4}$ | 2.67 | 6.29 |
| 3 | $H2 + OH = H2O + H$ | | $2.16 \times 10^{8}$ | 1.51 | 3.43 |
| 4 | $O + H2O = OH + OH$ | | $2.97 \times 10^{6}$ | 2.02 | 13.4 |
| | H2/O2 dissociation/recombination reactions | | | | |
| 5 | $H2 + M = H + H + M^{a}$ | | $4.58 \times 10^{19}$ | -1.40 | 104.38 |
| | $H2 + Ar = H + H + Ar$ | | $5.84 \times 10^{18}$ | -1.10 | 104.38 |
| | $H2 + He = H + H + He$ | | $5.84 \times 10^{18}$ | -1.10 | 104.38 |
| 6 | $O + O + M = O2 + M^{a}$ | | $6.16 \times 10^{15}$ | -0.50 | 0.00 |
| | $O + O + Ar = O2 + Ar$ | | $1.89 \times 10^{13}$ | 0.00 | -1.79 |
| | $O + O + He = O2 + He$ | | $1.89 \times 10^{13}$ | 0.00 | -1.79 |
| 7 | $O + H + M = OH + M^{a}$ | | $4.71 \times 10^{18}$ | -1.0 | 0.00 |
| 8 | $H + OH + M = H2O + M^{b}$ | | $3.8 \times 10^{22}$ | -2.00 | 0.00 |
| | Formation and consumption of HO2 | | | | |
| 9 | $H + O2 + M = HO2 + M^{c}$ | $k_0$ | $6.37 \times 10^{20}$ | -1.72 | 0.52 |
| | $H + O2 + M = HO2 + M^{d}$ | $k_0$ | $9.04 \times 10^{19}$ | -1.51 | 0.49 |
| | | $k_\infty$ | $1.48 \times 10^{12}$ | 0.60 | 0.00 |
| 10 | $HO2 + H = H2 + O2$ | | $1.66 \times 10^{13}$ | 0.00 | 0.82 |
| 11 | $HO2 + H = OH + OH$ | | $7.08 \times 10^{13}$ | 0.00 | 0.30 |
| 12 | $HO2 + O = OH + O2$ | | $3.25 \times 10^{13}$ | 0.00 | 0.00 |
| 13 | $HO2 + OH = H2O + O$ | | $2.89 \times 10^{13}$ | 0.00 | -0.50 |
| | Formation and consumption of H2O2 | | | | |
| 14 | $HO2 + HO2 = H2O2 + O2^{e}$ | | $4.20 \times 10^{14}$ | 0.00 | 11.98 |
| | $HO2 + HO2 = H2O2 + O2$ | | $1.30 \times 10^{11}$ | 0.00 | -1.63 |
| 15 | $H2O2 + M = OH + OH + M^{f}$ | $k_0$ | $1.20 \times 10^{17}$ | 0.00 | 45.5 |
| | | $k_\infty$ | $2.95 \times 10^{14}$ | 0.00 | 48.4 |
| 16 | $H2O2 + H = H2O + OH$ | | $2.41 \times 10^{13}$ | 0.00 | 3.97 |
| 17 | $H2O2 + H = H2 + HO2$ | | $4.82 \times 10^{13}$ | 2.00 | 7.95 |
| 18 | $H2O2 + O = OH + HO2$ | | $9.55 \times 10^{6}$ | 0.00 | 3.97 |
| 19 | $H2O2 + OH = H2O + HO2^{f}$ | | $1.00 \times 10^{12}$ | 0.00 | 0.00 |
| | $H2O2 + OH = H2O + HO2$ | | $5.8 \times 10^{14}$ | | 9.56 |

The thermal transport properties and reaction rate data are provided using the CHEMKIN software contained in ANSYS Fluent. For natural gas combustion, a short version of GRI 3.0 mechanism developed by Shi et al [20] is used. It describes reactions between 16 species.


## NOx formation model

Compared to the combustion rate, the NOx generation rate is very slow, therefore NOx formation can be obtained by post-processing. First, the combustion process is calculated without NOx formation and next the calculation of NOx formation is performed taking into account the fields of combustion species and temperature. In simulations of hydrogen combustion, only the thermal NOx mechanism was considered. In natural gas

combustion, both thermal and prompt mechanisms were taken into account. The formula involved in the simulation has been given in Section 2.5.

## 3.4   Computational Mesh

CFD simulation requires division of the domain into smaller subdomains. The division results in the generation of a mesh (or grid) of cells (elements or control volumes). The transport equations of flow properties are solved in each of these cells. The mesh of cells was generated from the computational domain described previously using the ANSYS-ICEM software, applying the block partition method. The created mesh consists of 375,465 structured hexahedral cells. The mesh has the following characteristics, all in an acceptable range. The cells have a maximum aspect ratio of 214, occurring in the inflation layer near the wall, a minimum orthogonal quality of 0.43, and a maximum skewness of 0.54. Figure 3.4 presents the mesh used for the simulation. Local mesh refinement was performed on the layer of fluid near the walls. The grid cells are concentrated around the boundary between solid and fluid, and near the flame (combustion zone) in order to resolve the gradients of the computed quantities.
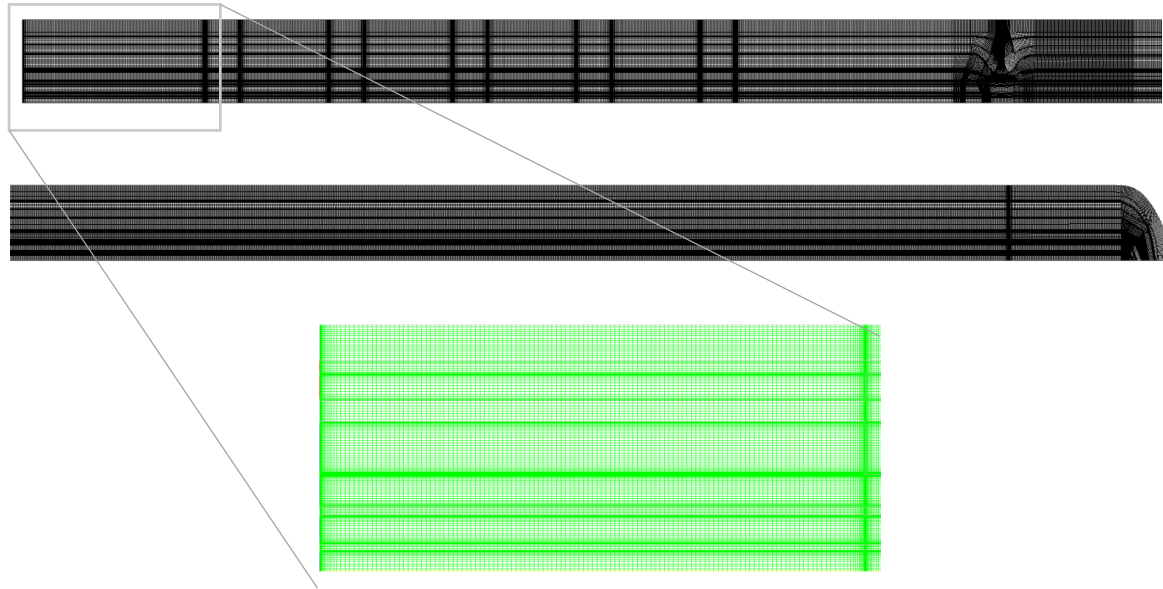


Figure 3.4: Computational mesh

## 3.5   Model validation

Measured data on the burner operation with natural gas is used for model validation. The measured data are obtained from burner operation with natural gas [25]. The measured variables are the concentration of oxygen, carbon monoxide, and NOx in flue gas at specific fuel and air rate to the burner. Table 3.3 presents the comparison between the result from the CFD model with the measured data. The result shows that the simulation results in lower prediction in oxygen content and NOx emission.

Table 3.3: Validation result of CFD model against measured data for the reference case

| Validation parameters | Measured data | CFD result |
|---|---|---|
| Flue gas composition at the final exit | | |
| $O_2$ (dry) [vol%] | 7.5 | 6.4 |
| CO (dry) [ppmv] | 0 | 0 |
| $H_2O$ | N/A | 13.77 |
| NOx (dry) [ppmv] | 213 average. | 246 |
| Flue gas exit temperature [K] | N/A | 1227 |

## 3.6  Case Studies Set Up

Simulations have been performed for six cases. The first two cases are for natural gas combustion at operational conditions for which measurement data are available. These cases were the operation at the minimum thermal power and maximum input thermal power of 5.0 kW and 11.7 kW. The power is based on flow rate data and the LHV. The data was obtained from a burner maintenance report at Nefit Industrial[25]. The third case is the operating conditions based on averaged operation data, with input thermal power of 8.2 kW. The next three cases are for hydrogen combustion at the same power as the first three cases. The input data for simulation with hydrogen fuel were calculated at the same input thermal power (LHV basis) and air ratio as the reference cases. The input data for these four cases are tabulated in Table 3.4.

LHV is used as the basis for thermal input power since it represents the actual available heat for the burner. The latent heat of water contained in the HHV is not useful in the range of burner temperature operation. A similar study has used constant power based on LHV as well [26].

Table 3.4: Input data for burner cases

| Case | Fuel | Fuel rate | Primary air inlet rate | Secondary air inlet rate | Input Power $\dot{Q}_{fuel}$ | Equivalence ratio $\Phi$ |
|---|---|---|---|---|---|---|
| | | [kg/s] | [kg/s] | [kg/s] | [kW] | [-] |
| #1 | Natural gas | 1.32e-4 | 2.124e-3 | 8.23e-4 | 5.0 | 0.59 |
| #2 | Natural gas | 3.053e-4 | 4.779e-3 | 8.23e-4 | 11.7 | 0.72 |
| #3 | Natural gas | 2.145e-4 | 3.156e-3 | 7.89e-4 | 8.2 | 0.72 |
| #4 | Hydrogen | 4.200e-5 | 1.762e-3 | 6.826e-4 | 5.0 | 0.59 |
| #5 | Hydrogen | 9.717e-5 | 3.982e-3 | 6.858e-4 | 11.7 | 0.72 |
| #6 | Hydrogen | 6.883e-5 | 2.519e-3 | 7.753e-4 | 8.2 | 0.72 |

# Burner Operation with Hydrogen

In this chapter, the simulation results of the CFD model for the burner are presented. As introduced in Section 3.6, there are six simulation cases that were performed. They are varied at different input thermal power for both the operation with natural gas and hydrogen. The analysis, which focused on the main parameters influencing the thermal efficiency and pollutant emissions at the exhaust (NOx) has been carried out for the different operating conditions of the burner. In Section 4.1 the flow and heat transfer comparison between hydrogen and natural gas combustion is evaluated at the same input thermal power (LHV based) and air ratio. In Section 4.2, the resulting fuel efficiency is compared for the six cases. The predicted NOx emission is discussed in Section 4.3. In Section 4.4, one of the options to reduce NOx emission is studied, which is the concept of internal flue gas recirculation.

## 4.1  Flow and Temperature Distribution Comparison

This section presents the observation made in the simulation results. Figure 4.1 presents the contour of static temperature for the operation with natural gas at 11.7 kW input thermal power. Figure 4.2 shows the visual comparison of the static temperature between hydrogen and natural gas at the same thermal input power $\dot{Q}_{fuel}$ and equivalence ratio $\Phi$. The peak temperature for natural gas combustion is 2324 K. Meanwhile, the peak temperature of hydrogen combustion is higher: 2671 K.
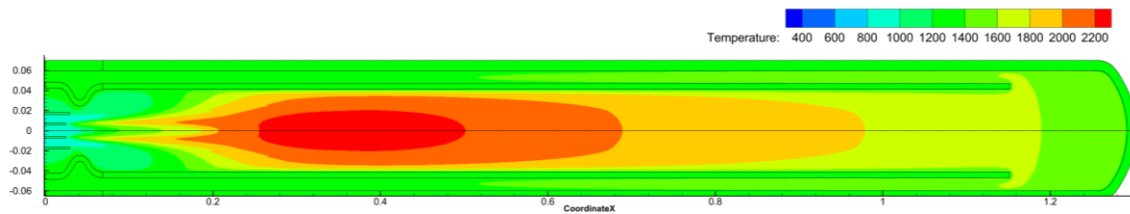


Figure 4.1: Contour of static temperature [K] for the operation with natural gas at $\dot{Q}_{fuel}$ = 11.7 kW and $\Phi$ = 0.72 (Case #1).
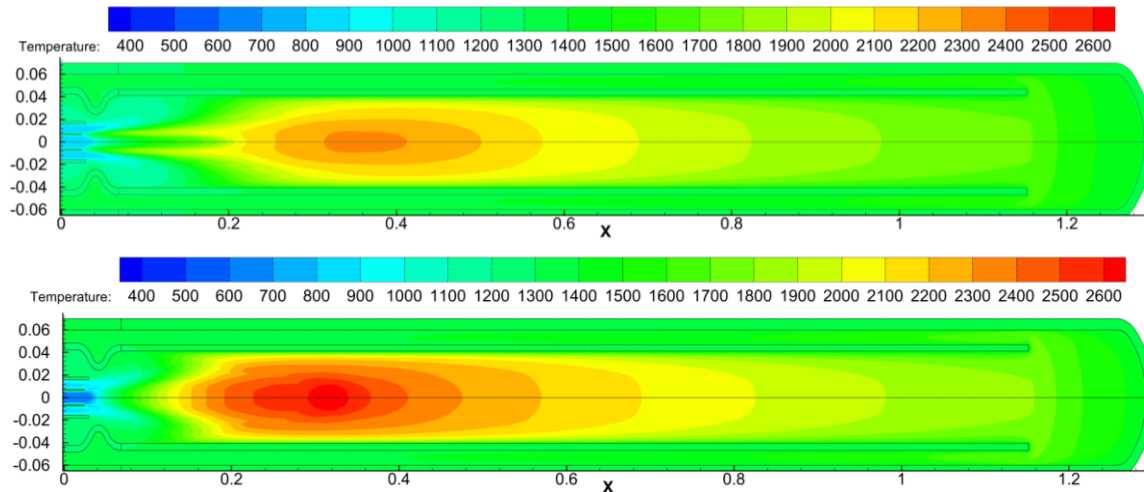
Figure 4.2: Contour of static temperature [K] for natural gas (top) and hydrogen (bottom) combustions at $\dot{Q}_{fuel} = 11.7$ kW and $\Phi = 0.72$.

Based on Figure 4.2, it seems that the hydrogen fuel flame is lifted from the fuel nozzle higher than the natural gas flame. Some literature on a non-radiant tube burner has shown the opposite result [26]. This means that the higher reactivity of hydrogen has not counterbalanced the high velocity for this case. Figure 4.3 shows the comparison of velocity magnitude contours and streamlines between the two cases. Due to the lower volumetric energy density, hydrogen fuel inlet velocity magnitude is almost three times higher than for natural gas'. The values are 10.0 m/s and 3.5 m/s for hydrogen and natural gas, respectively. As the fuel travels in the fuel injection tube, the velocity is fully developed. The flow has a lower velocity near the wall, and a higher velocity in the middle of the tube. The fuel temperature also increases as it travels toward the combustion zone, possibly because the tube's temperature becomes higher near the combustion zone by receiving radiation from the flame. The increase of temperature lowers the density and therefore increases the velocity. The maximum velocity magnitude of the fuels leaving the fuel nozzle is 15 m/s and 36 m/s, respectively for natural gas and hydrogen cases.
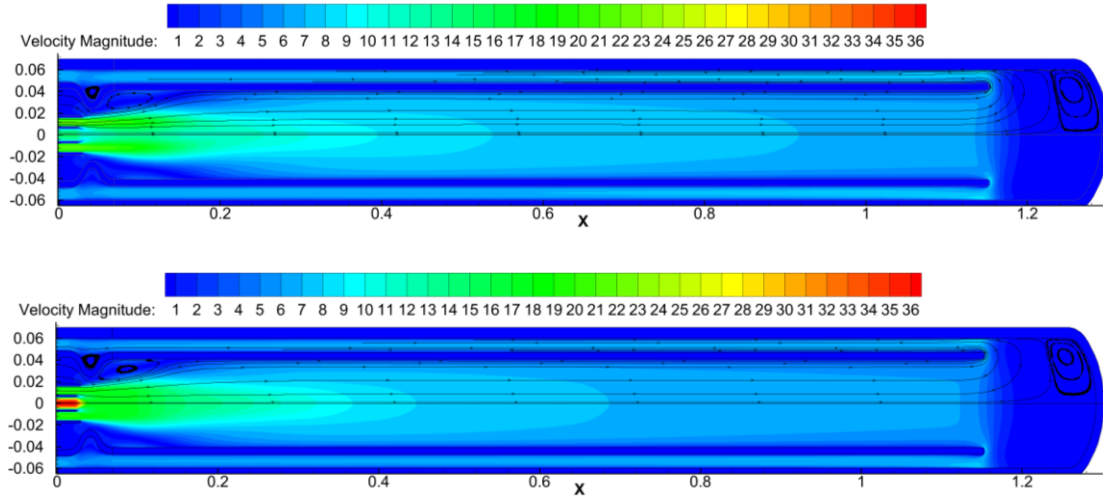
Figure 4.3: Contour of velocity [m/s] for natural gas (top) and hydrogen (bottom) at $\dot{Q}_{fuel} = 11.7$ kW and $\Phi = 0.72$.

## 4.2 Thermal Efficiency Comparison

The differences in flow and thermal properties between hydrogen and natural gas result in different effective heat transfer from the RTB to the furnace/load. Thermal efficiency $\eta_{th}$ for this burner is given in Eq. 47 [17].

$$\eta_{th} = 1 - \frac{\dot{Q}_{flue} + Q_{surface}}{\dot{Q}_{fuel} + \dot{Q}_{air}}$$

Eq. 47

where $\dot{Q}_{flue}$ is the energy loss with flue gas. $\dot{Q}_{surface}$ is the surface losses. $\dot{Q}_{fuel}$ is the chemical energy contained in the fuel and $\dot{Q}_{air}$ is the energy of the air. The rest of the burner surfaces is assumed to be adiabatic. Thus, $\dot{Q}_{surface}$ is eliminated. The air inlet is at the reference temperature, so $\dot{Q}_{air}$ is zero. Therefore Eq. 47 can be simplified to:

$$\eta_{th} = \frac{\dot{Q}_r}{\dot{Q}_{fuel}}$$

Eq. 48

$\dot{Q}_r$ is the net heat transfer to from the burner to the process side of the furnace. The thermal input power $\dot{Q}_{fuel}$ is based on LHV values. The $\dot{Q}_r$ is obtained from the integration of heat flux across the surface area of the burner radiant wall.

$$\eta_{th} = \frac{\int \dot{q}_r \, dA}{\dot{m}_{fuel} \times LHV_{fuel}}$$

Eq. 49

The calculated fuel efficiency for natural gas and hydrogen combustion for three different input power (case #1 - #6) are shown in Figure 4.4. The lowest thermal efficiency (5.7%) occurs at the lowest thermal input power (5.0 kW). The burner operation at this low power could happen when the products' temperature inside the furnace has reached the designated temperature. The highest thermal efficiency occurs at the operation with higher input power (11.7 kW). The simulation results have shown that the fuel efficiency

of using hydrogen is slightly higher (add 3 – 4% efficiency) than using natural gas on the RTB.
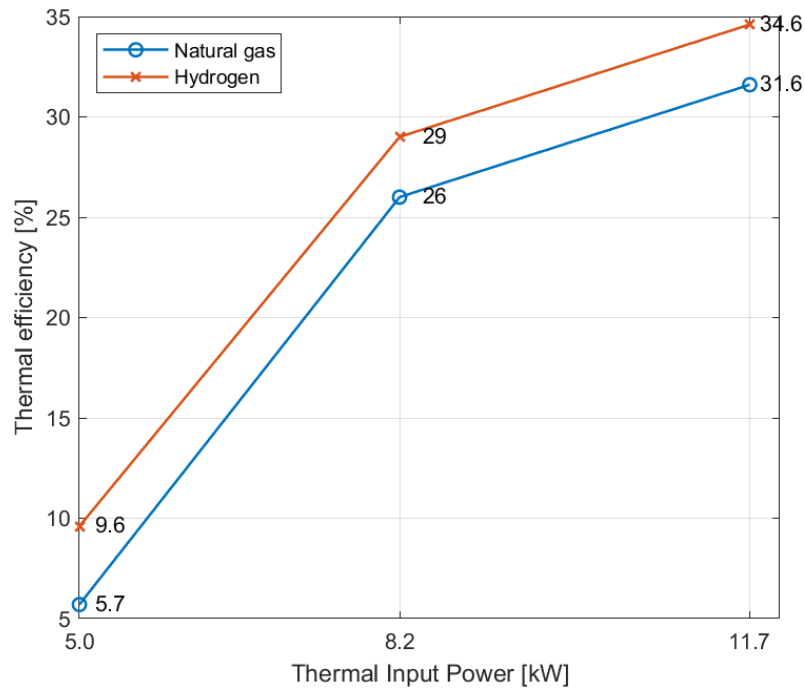


Figure 4.4: Fuel efficiency comparison between hydrogen and natural gas at several thermal input power

Literature shows that the thermal efficiency of RTB with self-heat recuperation is in the range of 58% to 85%. This is however for furnace operation at a lower temperature, 250 – 750 °C[17] [27]. In the present work, the furnace temperature is at 1050 °C. Thus, lower efficiency is expected.

The efficiency reduces as the thermal input power reduces. This is because the rate of heat transfer from combustion to the inside wall of the burner could not balance the heat transfer from the outside wall to the heat load. Therefore, some part of the radiant wall receives heat instead of releasing it. Figure 4.5 shows the temperature profile of the radiant wall for the six cases. The burner surface having a temperature above 1323.15 K releases heat to the load, while the surface having a temperature below 1323.15 K receives heat from the load/surrounding. The heat flux profile from the wall is shown in Figure 4.6. It can be seen that, for any thermal input power, a larger part of the wall on natural gas cases receives heat compared to the corresponding hydrogen cases.
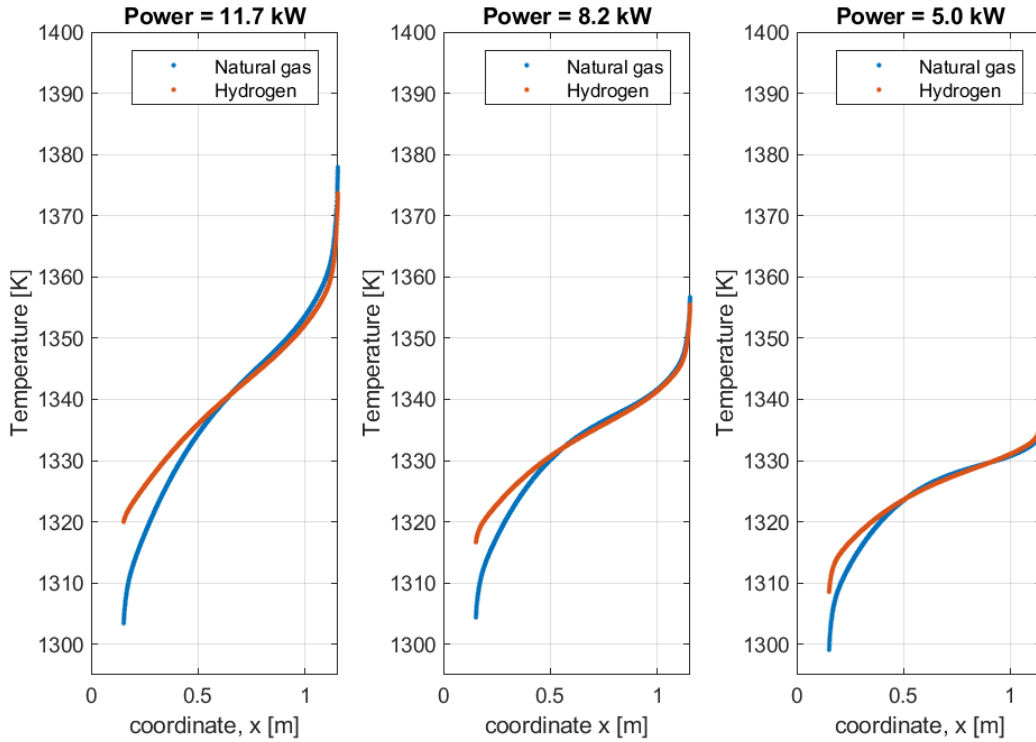
Figure 4.5: Temperature profile of the radiant surface at different thermal input power (11.7 kW, 8.2 kW, and 5.0 kW)
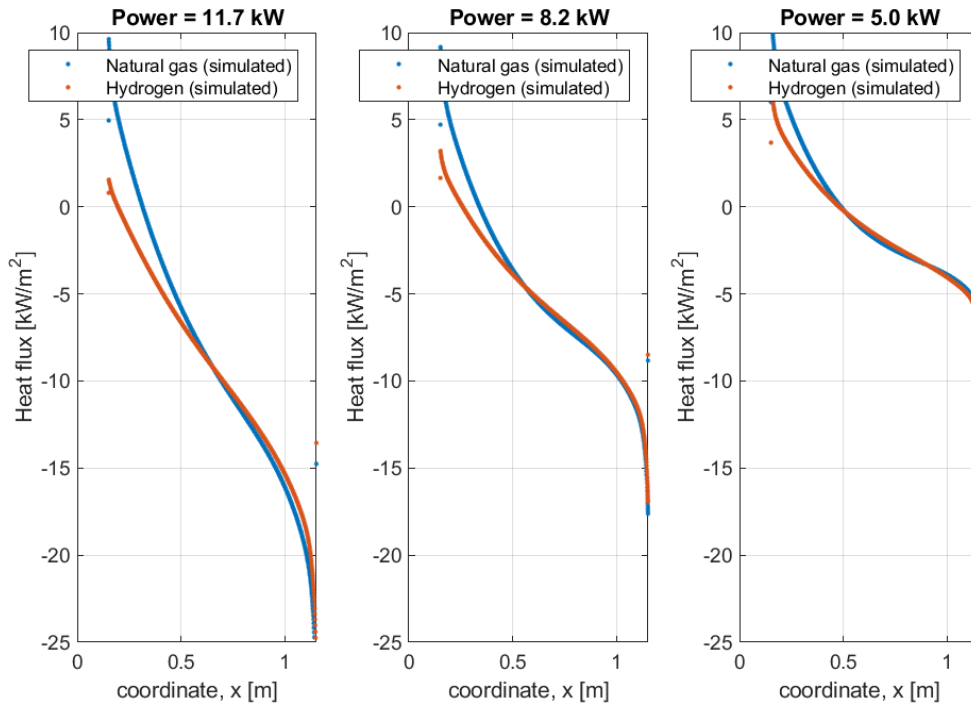


Figure 4.6: Heat flux profile on the radiant wall for different thermal input power (11.7 kW, 8.2 kW, and 5.0 kW)

To understand the reasoning, first, we look into the temperature profile in the burner. Figure 4.7 shows a temperature profile comparison between natural gas and hydrogen for several location samples on the x-direction for cases with $\dot{Q}_{fuel}$ = 11.7 kW and $\Phi$ = 0.72. Before the fuel and air leaving their nozzles (x = 0 m), the temperature of the

primary air and secondary air streams are slightly higher for the hydrogen case compared to the natural gas case. But the fuel temperature of hydrogen is significantly lower. Then, in the first part of the combustion zone (x = 0.1 m), there is a temperature peaking for the natural gas case. As we move in the x-direction, the temperature of fluid and solids in the hydrogen case becomes higher compared to the natural gas case. So, in general, the flame and fluid temperature are higher in the case of hydrogen than the natural gas.
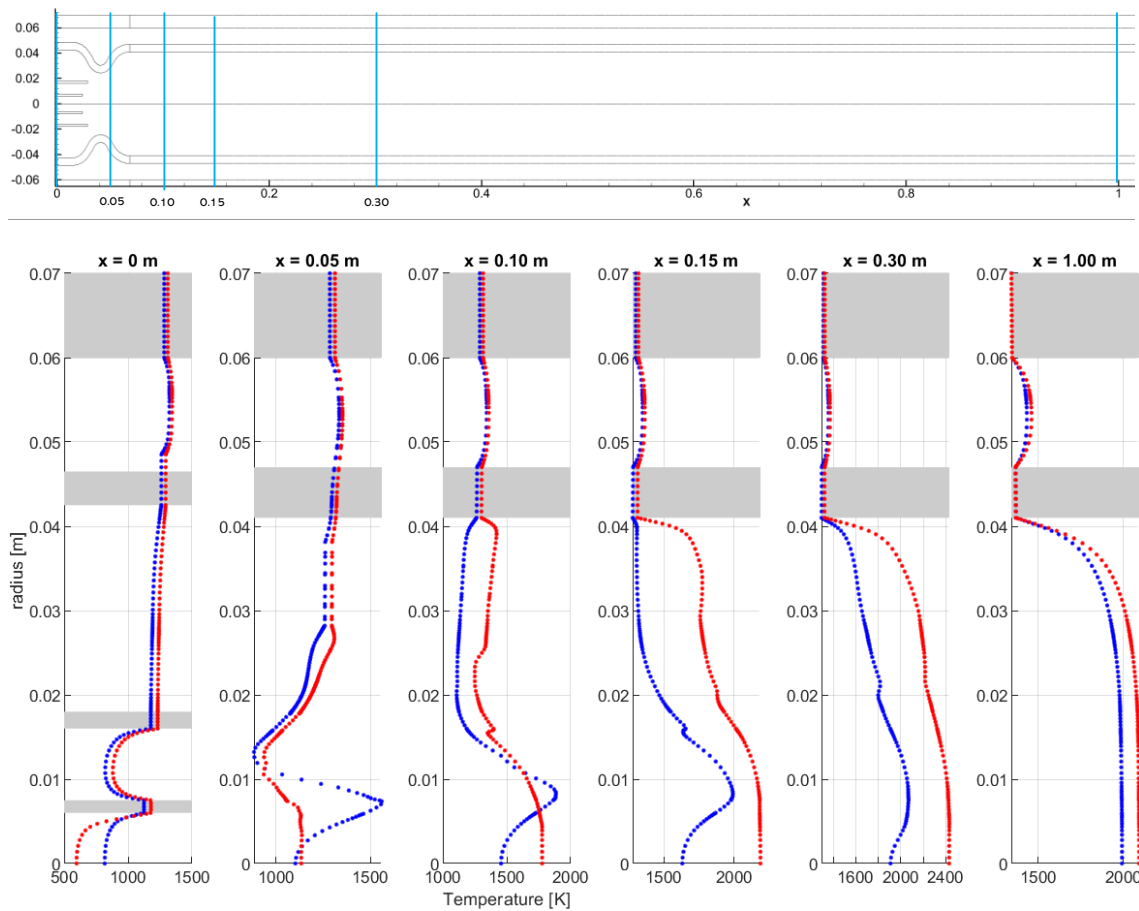


Figure 4.7: Temperature profile in the burner for the cases of (●) natural gas and (●) hydrogen at $\dot{Q}_{fuel} = 11.7$ kW and $\Phi = 0.72$.

The higher fluid temperature on the hydrogen cases was achieved since the total mass of the hydrogen case is around 20% lower than the natural gas case. As the total input power is the same, the case with a lower mass rate would have a higher temperature.

### Absorption coefficient

Hydrogen combustion produces only water. While natural gas combustion produces carbon dioxide as well. The difference in combustion product composition affects the radiation absorption coefficient. The absorption coefficient is calculated by WSSG methods (see Section 2.6). Water and carbon dioxides are the two gases with the highest absorption coefficient. In hydrogen combustion, the combustion product has a higher concentration of water compared to the natural gas combustion. But it has no carbon dioxide. The resulted absorption coefficient comparison for several sample locations is

shown in Figure 4.8. From the figure, it can be seen that the absorption coefficient of hydrogen combustion products is lower than the natural gas' at any location. The average mole fraction of water and carbon dioxide on the natural gas case is 6.9% and 13.8% respectively. While the average water mol fraction on the hydrogen case is 26.1%.
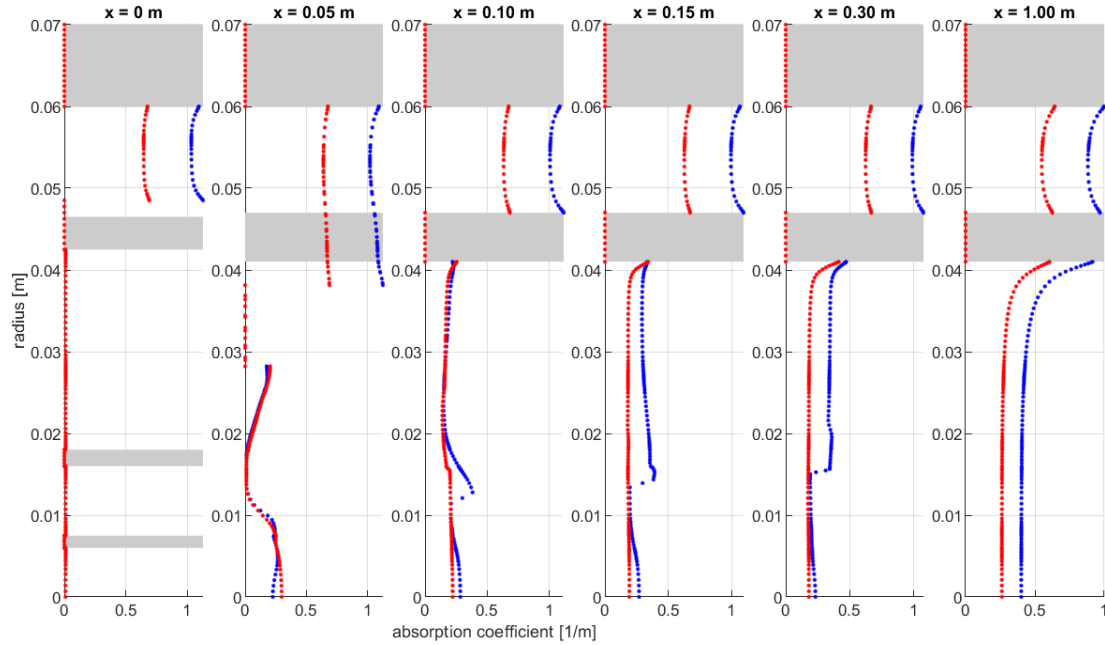


Figure 4.8: Absorption coefficient in the cases of (●) natural gas and (●) hydrogen at $\dot{Q}_{fuel} = 11.7$ kW and $\Phi = 0.72$.

## Temperature distribution

In a radiant tube burner, the temperature distribution is an important parameter that determines the heat flux at the radiant wall. Figure 4.9 shows the temperature profile of the radiant wall, wall on the inner tube, inside wall of the outer tube, and the flue gas. Compared to the hydrogen case, the temperature of the inner wall at x coordinate < 0.3 m is significantly lower for the natural gas case. This is due to lower secondary air temperature and the fact that the flame is far from the nozzle compared to hydrogen. Figure 4.10 shows a more clear contour of temperature comparison, especially for x < 0.3 m.
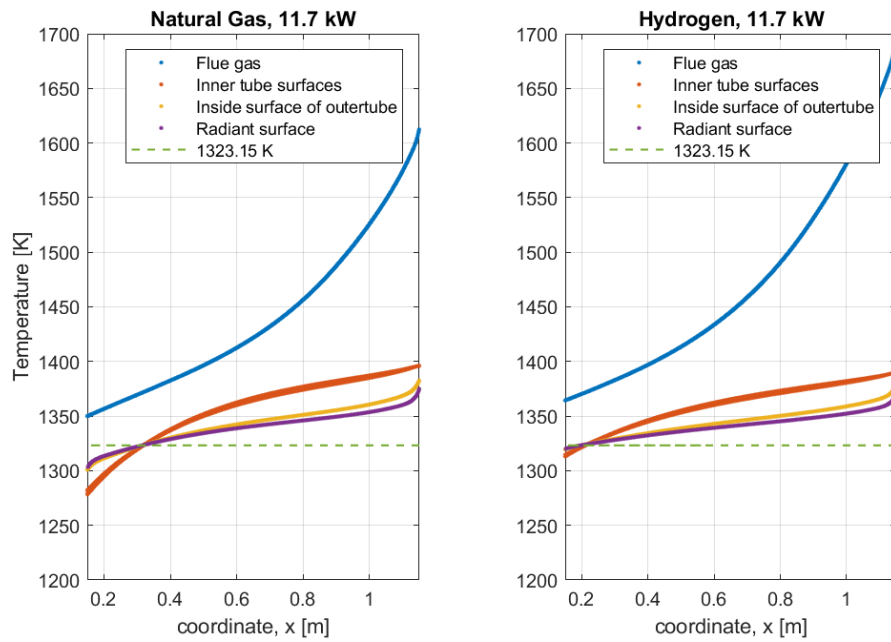
Figure 4.9 Temperature profile of gases and several walls for cases at $\dot{Q}_{fuel} = 11.7$ kW and $\Phi = 0.72$.

The significantly lower innertube temperature at x < 0.3 m has contributed to lowering the radiant wall temperature at x < 0.3. The temperature goes below 1323 K and therefore starts receiving heat from the outside and thus reducing the net heat transfer.
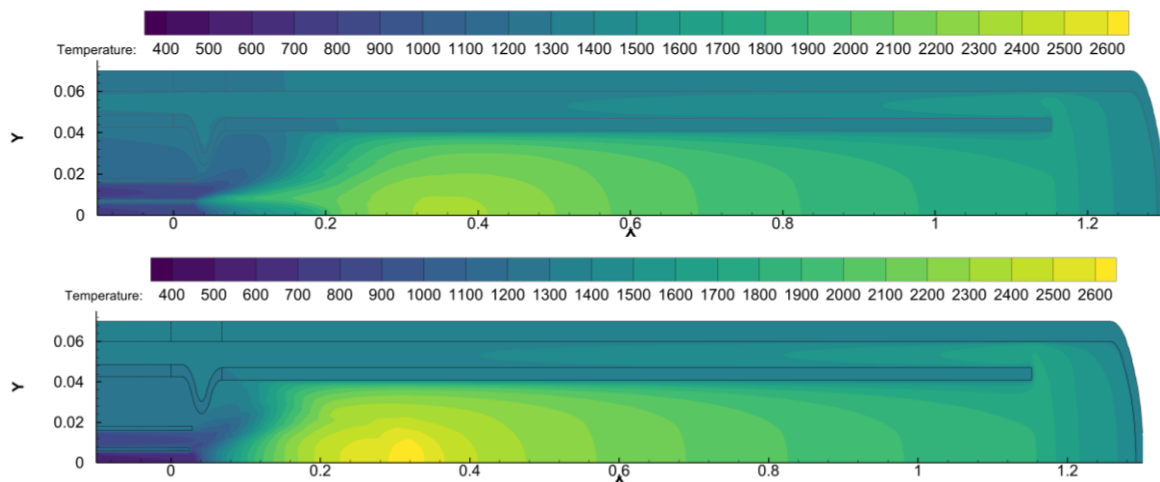


Figure 4.10 Temperature [K] contour comparison between natural gas (top) and hydrogen (bottom) combustion at $\dot{Q}_{fuel} = 11.7$ kW and $\Phi = 0.72$.

Higher radiant duty is observed as well by Lowe et al [28] on switching from refinery fuel to hydrogen on a radiant tube burner.

### 4.2.1  Heat Recuperation

In a self-recuperative burner, a heat exchanger is built into the burner so that the hot combustion products preheat the air while it travels to exit from the burner. Having a built-in heat recuperation in the burner has some advantages over an external heat exchanger for recovering energy. The built-in heat exchanger does not require a

significant amount of large, insulated ductwork as the external exchanger does. However, the heat exchanger built into the burner may be less efficient than an external exchanger and therefore tends to have lower preheat temperatures. [17]

The heat recuperated from the flue gas into the inlet streams is shown in Figure 4.11 in terms of percentage. It is defined as the net heat transferred from flue gas to the inlet streams divided by the input thermal power. In any case, the heat recuperation percentage is lower on the hydrogen case compared to the natural gas.
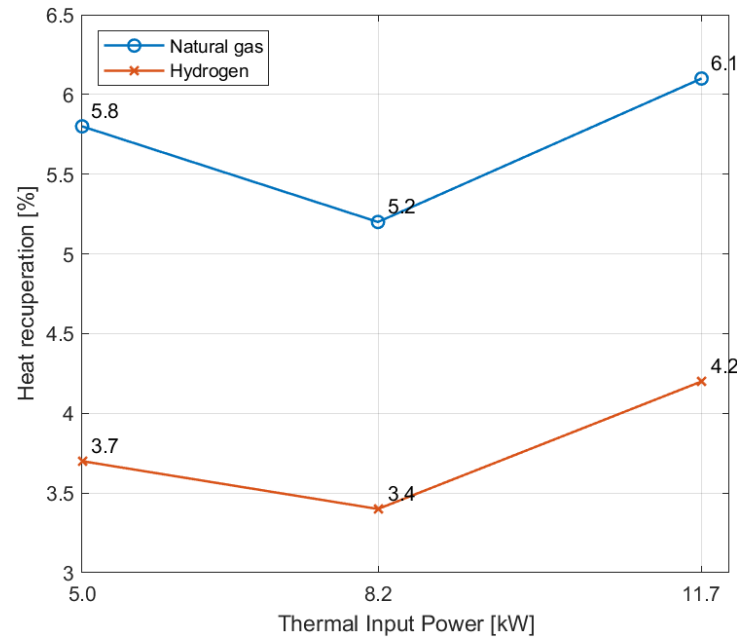


Figure 4.11 Heat recuperation percentage

Figure 4.12 shows the heat flow on the burner system. The heat input is the heat from the fuel $\dot{Q}_{fuel}$. In the heat exchange zone, an amount of heat is recuperated $\dot{Q}_{recup}$ from flue gas $\dot{Q}_{flue}$. The heat exchange zone also receives heat $\dot{Q}_{return}$ from the combustion zone through conduction from the solids and radiation from the flame. $\dot{Q}_{rad}$ is the heat rate supplied from the burner to the furnace. The heat flow for each case is tabulated in Table 4.1.
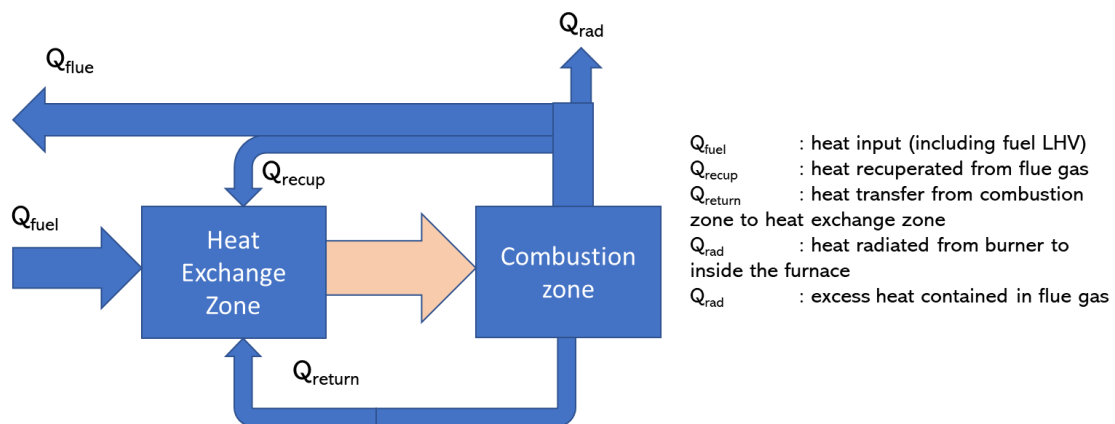


Figure 4.12: Illustration of heat flow on the burner system

Table 4.1: Comparison of heat flow between hydrogen and natural gas cases

| | Natural gas | | | Hydrogen | | |
|---|---|---|---|---|---|---|
| | $\dot{Q}_{fuel}$ = 5.0 kW | $\dot{Q}_{fuel}$ = 8.2 kW | $\dot{Q}_{fuel}$ = 11.7 kW | $\dot{Q}_{fuel}$ = 5.0 kW | $\dot{Q}_{fuel}$ = 8.2 kW | $\dot{Q}_{fuel}$ = 11.7 kW |
| $Q_{flue}$ [kW] | 4759 | 6068 | 7967 | 4560 | 5826 | 7613 |
| $Q_{recup}$ [kW] | 293 | 427 | 707 | 187 | 279 | 485 |
| $Q_{return}$ [kW] | 2846 | 3699 | 4678 | 1707 | 1989 | 2360 |
| $Q_{rad}$ [kW] | 285 | 2128 | 3697 | 480 | 2374 | 4047 |
| $Q_{fuel}$ [kW] | 5044 | 8196 | 11664 | 5040 | 8200 | 11660 |

The heat recuperation for any hydrogen cases is lower than its corresponding natural gas cases, as shown in Table 4.1. This indicates that the convective heat transfer is better in the case of natural gas. A similar result was obtained from a study that compares hydrogen and refinery fuel on RTB with a recuperation section. A decreased in convection section duty is observed [28].

The heat exchanger is modeled in a two-dimensional (2D) domain (referred to as 2D built-in) and is connected to the combustion zone. To evaluate the impact of having a 2D domain, the result of the heat recuperation section is compared to a separate simulation with a 3D domain (referred to as 3D external). The 3D domain is only for the heat recuperation zone, not including the combustion zone. The 3D domain is shown in Figure F.1. Another 2D heat exchanger model (referred to as 2D external), which is also not attached to the combustion zone, is therefore also required for comparison. Table 4.2 shows the heat transfer comparison in the heat exchanger zone for the three models.

The first observation from the result in Table 4.2 is that between the 3D external and 2D-external, the calculation result of heat recuperated from flue gas is almost the same (8% difference). Therefore, it can be concluded that the selection of the 2D domain does not have a significant impact on the result. The second observation is that the heat recuperated on the 2D built-in heat exchanger is significantly lower compared to the other two models. Notice that the total enthalpy change in the heat recuperation zone is not zero. This is the amount of heat received from the combustion zone via flame radiation and conduction on the solids. The heat receives by the heat exchanger zone from the combustion zone actually reduces the heat recuperation performance. The heat received increases the temperature of air and fuel, thus reduces the temperature gradient between the flue gas and the incoming air and. This becomes the disadvantage of the self-recuperative burner.

Table 4.2 Heat exchange comparison between 3 models of the heat exchanger

| | | 2D built-in | | | 3D external | | | 2D external | | |
|---|---|---|---|---|---|---|---|---|---|---|
| Stream | Mass flow | Inlet T | Outlet T | ΔH | Inlet T | Outlet T | ΔH | Inlet T | Outlet T | ΔH |
| | [kg/s] | [K] | [K] | [W] | [K] | [K] | [W] | [K] | [K] | [W] |
| Flue gas | 5.91E-03 | 1317 | 1227 | 707 | 1323 | 1052 | 2673 | 1323 | 1065 | 2462 |
| Fuel | 3.05E-04 | 293 | 867 | -457 | 293 | 433 | -92 | 293 | 419 | -81 |
| Primary air | 4.78E-03 | 293 | 864 | -2885 | 293 | 570 | -1392 | 293 | 547 | -1269 |
| Secondary air | 8.23E-04 | 293 | 1200 | -811 | 293 | 1028 | -1188 | 293 | 968 | -1112 |
| Total | | | | -3446 | | | 0 | | | 0 |

## 4.3  NOx Emission Comparison

Hydrogen combustion in general has a high flame speed, short ignition delay time, and wide flammability limit compared to natural gas [26]. It burns with a higher adiabatic flame temperature than natural gas, therefore increases the potential for NOx emission. This section presents the comparison of NOx emission between the operation with the two fuels.

Table 4.3 presents the result of NOx emission (dry basis) for the natural gas base case (simulated and measured), and for the hydrogen case (simulated). First, it can be seen that the model has accurately simulated the NOx emission for the base case for two different values of thermal input power. Secondly, the replacement with hydrogen is expected to increase the NOx emission by 10 – 15 times.

A study by Ilbas et al shows that the use of ANSYS Fluent NOx post-processor to predict NOx emission on hydrogen fuel combustion shows good agreement with experimental data. In that study, the turbulent is modeled using the standard k-ε model as well. The chemical reaction is described by seven species and three steps.[29]

Table 4.3 NOx emission comparison in ppmv (dry)

| Thermal input power $\dot{Q}_{fuel}$ | Equivalence ratio $\Phi$ | Natural gas (measured) | Natural gas (simulated) | Hydrogen (simulated) |
|---|---|---|---|---|
| 5.0 kW | 0.59 | 124.9 | 127 | 1607 |
| 8.2 kW | 0.72 | N/A | 371 | 4493 |
| 11.7 kW | 0.72 | 213 | 246 | 3952 |

There are two reasons for higher NOx emission on the hydrogen case. The first reason is the higher local temperature in the hydrogen case. NOx formation rate is highly influenced by temperature, as explained in Sec 2.5, because of the reaction Eq. 28 has high activation energy.

The second reason is due to higher oxygen radical concentration [O] as suggested by Eq. 31. Figure 4.13 shows the comparison for [O] concentration between the base case and hydrogen case. The concentration of [O] on the hydrogen case is significantly higher and covers a larger area than the case of natural gas.
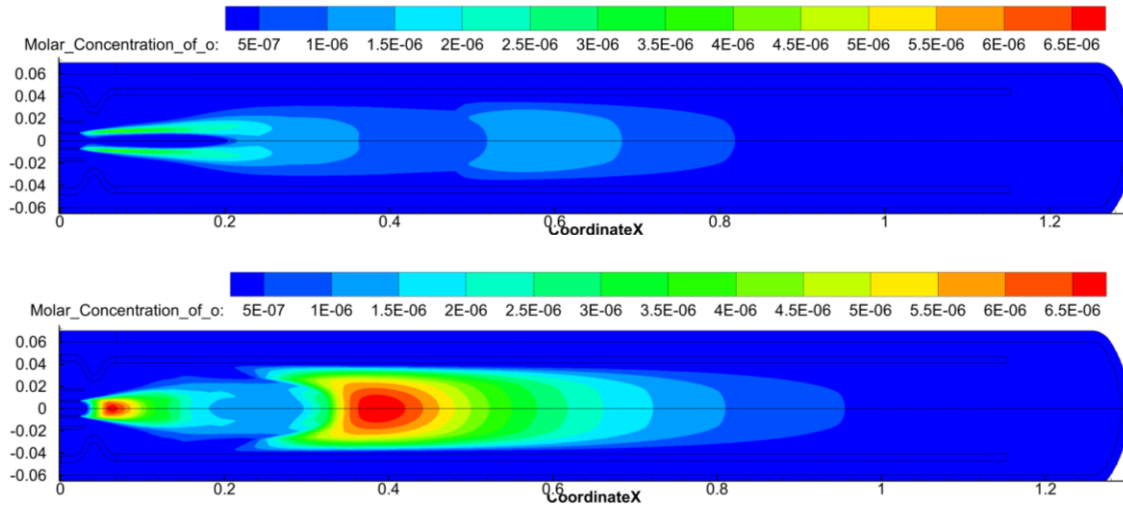


Figure 4.13: Contour of O molar concentration [mol/m$^3$], [O], for natural gas combustion (top) and hydrogen combustion (bottom).

Both the higher temperature and oxygen radical concentration [O] lead to a significantly higher NOx formation rate. The comparison is shown in Figure 4.14. The prompt formation is not shown here since it contributes only <5% to NOx formation in the natural gas case and does not contribute at all to the hydrogen case.
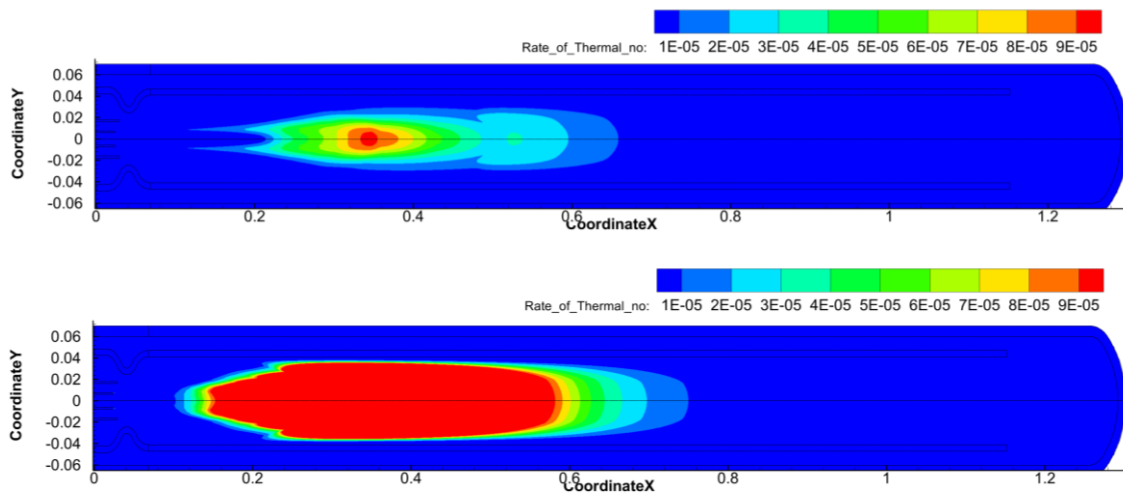


Figure 4.14: Contour of NO$_x$ formation rate [mol/m$^3$s] for hydrogen combustion (top) and natural gas combustion (bottom).

Another important parameter that determines the amount of NOx generated is residence time. The formation rate shown in Figure 4.13 expresses the amount of NOx generated per unit time. The final quantity of generated NOx depends on residence time in the space. Residence time depends on the velocity of the fluid at the space. Residence time for the cases hydrogen and natural gas are different since the velocities of the inlet gases are different. Especially, the velocity of inlet hydrogen fuel is roughly double the velocity

of natural gas. For all cases, the fluid velocity on the hydrogen combustion cases is not high enough to have lower NOx emission than the natural gas combustion. But, the influence of residence time explains the higher NOx emission on the cases at $\dot{Q}_{fuel}$ = 8.2 kW compared to $\dot{Q}_{fuel}$ = 11.7 kW.

Figure 4.15 shows the comparison of NOx formation rate for hydrogen combustion at $\dot{Q}_{fuel}$ = 8.2 kW (top) and $\dot{Q}_{fuel}$ = 11.7 kW (bottom). Both cases are at equivalence ratio $\Phi$ = 0.72. The contour shows that there is more area with a high formation rate in the case with $\dot{Q}_{fuel}$ = 11.7 kW. But its velocity is significantly higher than the case with $\dot{Q}_{fuel}$ = 8.2 kW. The total NOx emission is, therefore, lower than the case at $\dot{Q}_{fuel}$ = 8.2 kW as shown in Table 4.3.
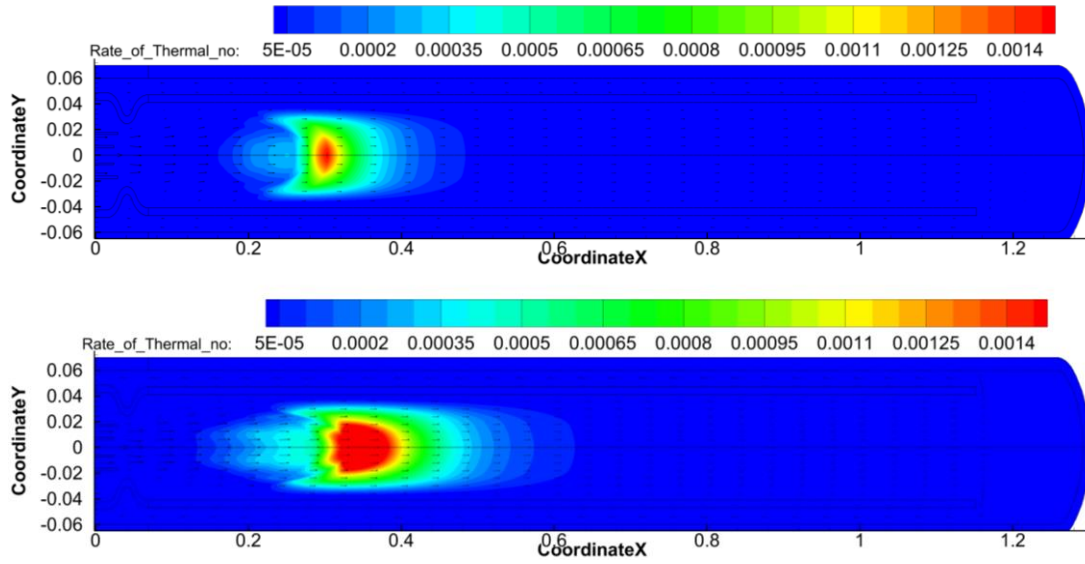


Figure 4.15: Contour of NOx formation rate [mol/m³s] for hydrogen combustion $\dot{Q}_{fuel}$ = 8.2 kW (top) and $\dot{Q}_{fuel}$ = 11.7 kW (bottom). $\Phi$ = 0.72.

## 4.4   Options to mitigate high NOx emission

In this Section. the effect of increasing air ratio to reduce NOx emission is discussed. A simulation of a proposed design applying an internal flue gas recycling technique is provided to prove the working principle and simulate the level of reduction of the proposed design.

NOx emission is regulated and is expected to become stricter as environmental concern is rising. The level is normally regulated in the unit of mg/Nm³. In the European Union (EU), the limit for an existing plant is 300 mg/Nm³ for gaseous fuel [30]. The limit is stricter for a new plant. In the Netherlands, the limit is 150 mg/Nm³ for a new plant [31]. The unit of NOx emission on the previous sections is in ppmv (dry basis). NOx measurements are mostly in ppmv and dry basis [32]. To convert to mg/Nm³ unit, Eq. 50 is used.

$$NO \left[\frac{mg}{m3}\right] = [NO\ ppm] \times \frac{W_{NO}}{Wflue} \times \frac{\dot{m}}{\dot{V}} \qquad \text{Eq. 50}$$

The ppm value must be first corrected by a standard reference oxygen content by Eq. 51. [33]. The reference oxygen content is 3% for gaseous fuel [30][31].

$$ppm_{CORR} = ppm_{MEAS} \left[\frac{20.95 - O_{2_{basis}}}{20.95 - O_{2_{MEAS}}}\right] \qquad \text{Eq. 51}$$

Subscript MEAS means for the measured value. The resulted unit conversion for the NOx emission for the six simulated cases is shown in Table 4.4. As expected, the NOx emission on the hydrogen cases is higher than the regulation.

Table 4.4 NOx emission in several units of measure for the six simulated cases.

| | Natural gas | | | Hydrogen | | |
|---|---|---|---|---|---|---|
| $\dot{Q}_{fuel}$ [kW] | 5.0 | 8.2 | 11.7 | 5.0 | 8.2 | 11.7 |
| NOx [ppmv] (wet) | 112.0 | 320.0 | 212.0 | 1255.0 | 3344.0 | 2928.0 |
| % vol $O_2$ | 8.1 | 5.6 | 5.5 | 7.7 | 5.4 | 5.3 |
| % vol $H_2O$ | 11.5 | 13.7 | 13.8 | 21.9 | 25.6 | 25.9 |
| NOx [ppmv] (dry) | 126.5 | 371.0 | 245.9 | 1606.7 | 4492.8 | 3952.0 |
| NOx [ppmv] (dry) ($O_2$ corrected) | 176.7 | 432.7 | 286.2 | 2176.6 | 5169.6 | 4538.5 |
| mg NOx/kW | 179.4 | 361.9 | 238.2 | 1784.5 | 3495.4 | 3047.7 |
| mg NOx/Nm3 | 82.3 | 199.1 | 131.5 | 921.7 | 2126.3 | 1857.2 |

To reduce the NOx emissions. There are several modification techniques that could be applied, for example: air preheat reduction, air staging, gas recirculation, water injection, and reburning, and low NOx burner techniques [11]. An EPA study suggests that ultra-low NOx burners are the most cost-effective means to reduce NOx. Table 4.5 shows the typical NOx reduction for different low-NOx burner types. The internal flue gas recirculation (FGR) has the most significant impact in reducing NOx. Therefore, a modification of the existing burner applying the internal FGR is proposed and discussed in Section 4.4.2. The effect of adjusting air to fuel ratio is studied as well (in Section 4.4.1), since it is the most simple and low operating cost technique.

Table 4.5 NOx Reductions for different low-NOx burner types [11]

| Burner Type | Typical $NO_x$ Reductions |
|---|---|
| Staged-air burner | 25%–35% |
| Staged-fuel burner | 40%–50% |
| Low-excess-air burner | 20%–25% |
| Burner with external flue gas recirculation (FGR) | 50%–60% |
| Burner with internal flue gas recirculation | 40%–50% |
| Air or fuel-gas staging with internal FGR | 55%–75% |
| Air or fuel-gas staging with external FGR | 60%–80% |

### 4.4.1  Air Ratio Adjustment

To reduce NOx emission, a higher air ratio (or lower equivalence ratio) could be applied to the combustion of hydrogen. Table 4.6 shows the result for reducing the equivalence ratio to the NOx emission and fuel efficiency for hydrogen case with $\dot{Q}_{fuel}$ = 8.2 kW. As shown in the figure, NOx emission has reduced as the equivalence ratio is decreased, but so is the fuel efficiency. At equivalence ratio = 0.5, the NOx emission is almost comparable to the corresponding natural gas case (199 mg/Nm$^3$). However, the efficiency is greatly reduced by almost 50%. Thus, it is not feasible to reduce NOx emission for hydrogen combustion in this case with adjusting the air ratio.

Table 4.6 NOx emission and thermal efficiency as a function of equivalence ratio for hydrogen combustion at $\dot{Q}_{fuel}$ = 8.2 kW

| Equivalence ratio $\Phi$ | NOx [ppmv] (dry) | O$_2$ % vol | $\dot{Q}_r$ [kW] | $\eta_{th}$ | NOx [mg/Nm3] |
|---|---|---|---|---|---|
| 0.3 | 43 | 13.9 | -1524 | N/A | 50.5 |
| 0.4 | 130 | 11.7 | 182 | 2% | 112.4 |
| 0.5 | 515 | 9.58 | 1211 | 15% | 351.7 |
| 0.6 | 2033 | 7.56 | 1873 | 23% | 1151.2 |
| 0.72 | 4493 | 5.35 | 2374 | 29% | 2126.3 |

### 4.4.2  Design with Internal Flue Gas Recirculation

Internal flue gas recirculation leads to better temperature uniformity. Flue gas entrainment dilutes the combustion zone. The dilution reduces the rate of NOx formation in two ways. First, it reduces the temperature in the combustion zone. Flue gas has a higher heat capacity compared to fuel and air. Higher heat capacity allows for a lower temperature increase with the same amount of heat. Even though the flue gas temperature is high, but compared to temperature in the combustion zone, it's relatively lower. Secondly, flue gas entrainment reduces the concentration of oxygen radicals [O] in the combustion zone. Oxygen content in the flue gas is significantly lower than the oxygen content in the oxidant stream (air). Consequently, the formation rate of NOx emission reduces significantly.

The internal recirculation of the flue gas can be achieved through making cuts on the inner tube near the fuel and air nozzles' tips. The high velocity of the air and fuel leaving the nozzle has enabled entrainment of flue gas into the combustion zone. Figure 4.16 shows the modified burner geometry and velocity profile near the circulation region and its comparison with the base case.
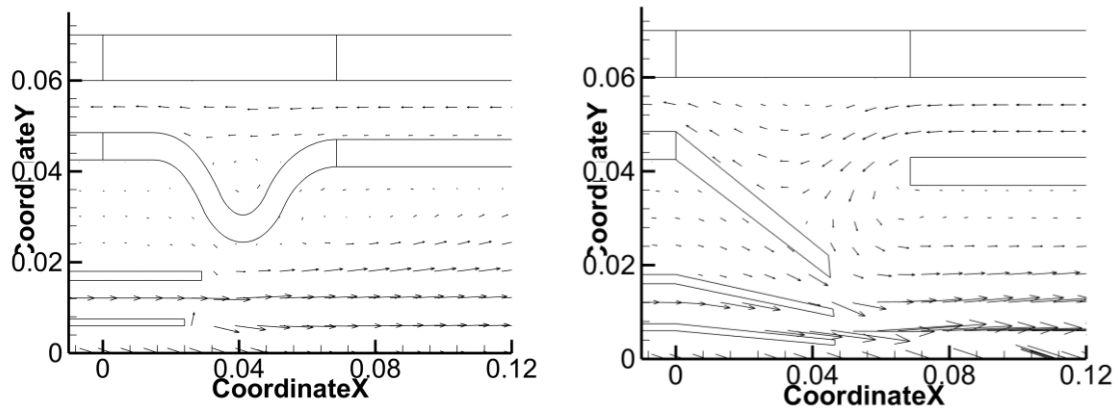
Figure 4.16: Velocity vector comparison between the base geometry (left) with proposed geometry modification (right). $\dot{Q}_{fuel} = 8.2$ kW (bottom). $\Phi = 0.72$.

Figure 4.17 presents the comparison between the temperature contour between the case with internal flue gas recirculation (FGR) and the base case. The maximum temperature on the FGR case is only slightly lower (2492 K) than the base case (2571 K). However, the area with a high temperature is significantly reduced.
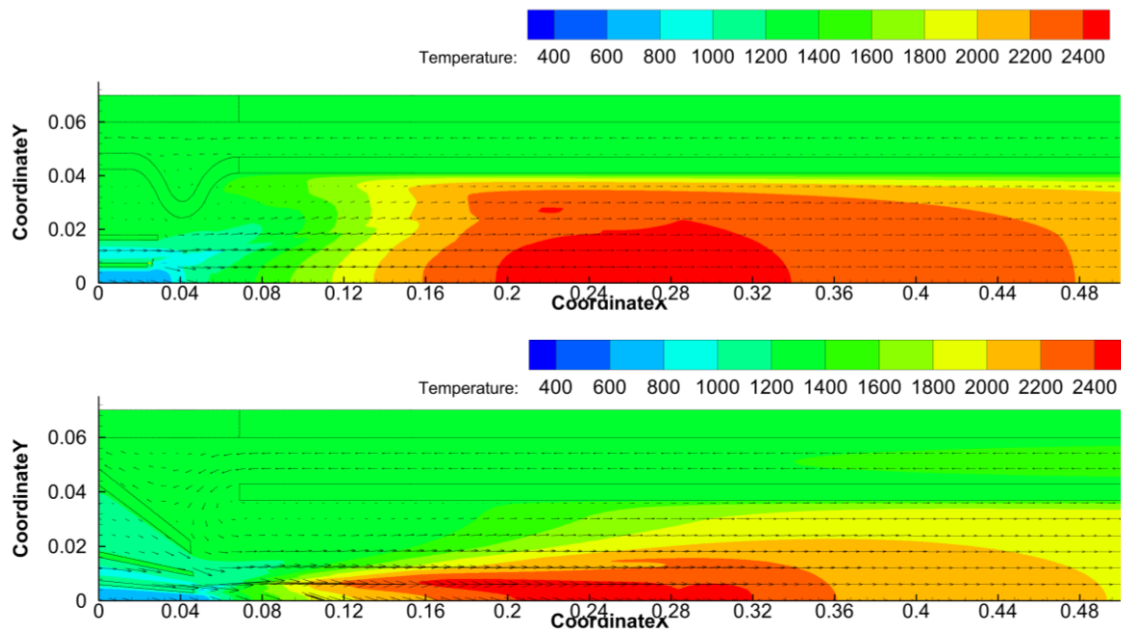


Figure 4.17: Temperature contour comparison between the base case (top) and the case with proposed modification (bottom). $\dot{Q}_{fuel} = 8.2$ kW (bottom). $\Phi = 0.72$.

The dilution of the combustion zone by the flue gas has also reduced the concentration of the [O] atom. The reduction of Oxygen atom concentration is shown in Figure 4.18. Overall, the area of high [O] concentration is reduced compared to the base case. There's a higher Oxygen concentration near the burner tip, but the temperature in the area is relatively low, thus it has not significantly contributed to NOx formation. The comparison of the NOx formation rate is shown in Figure 4.19.
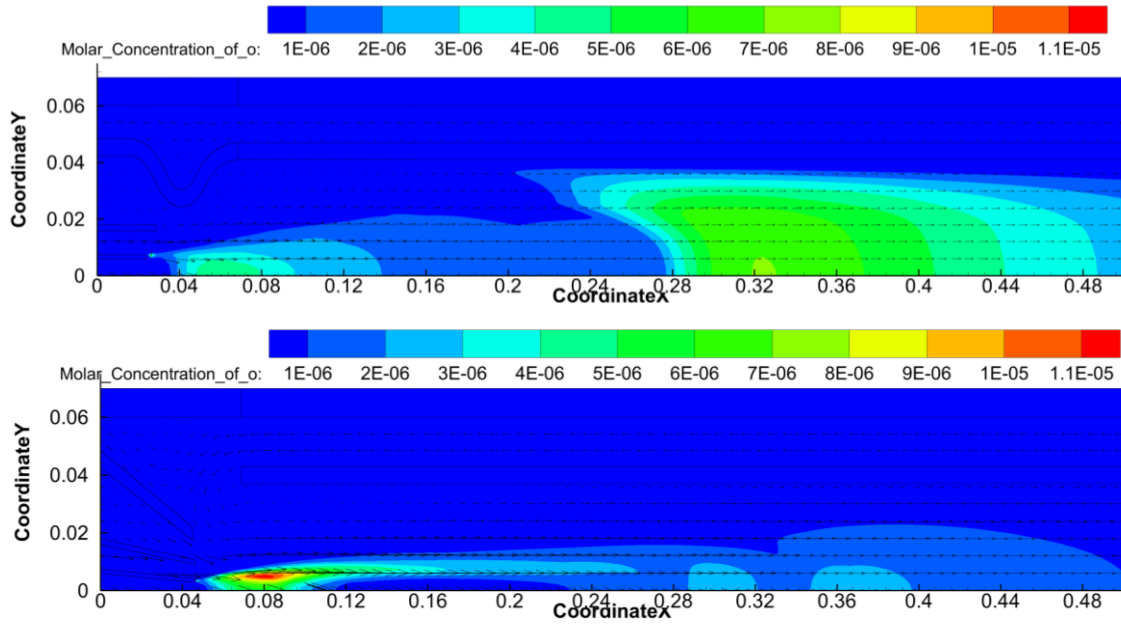
Figure 4.18: Comparison of O concentration [mol/m³] between base case (top) and FGR (bottom). $\dot{Q}_{fuel} = 8.2$ kW (bottom). $\Phi = 0.72$.
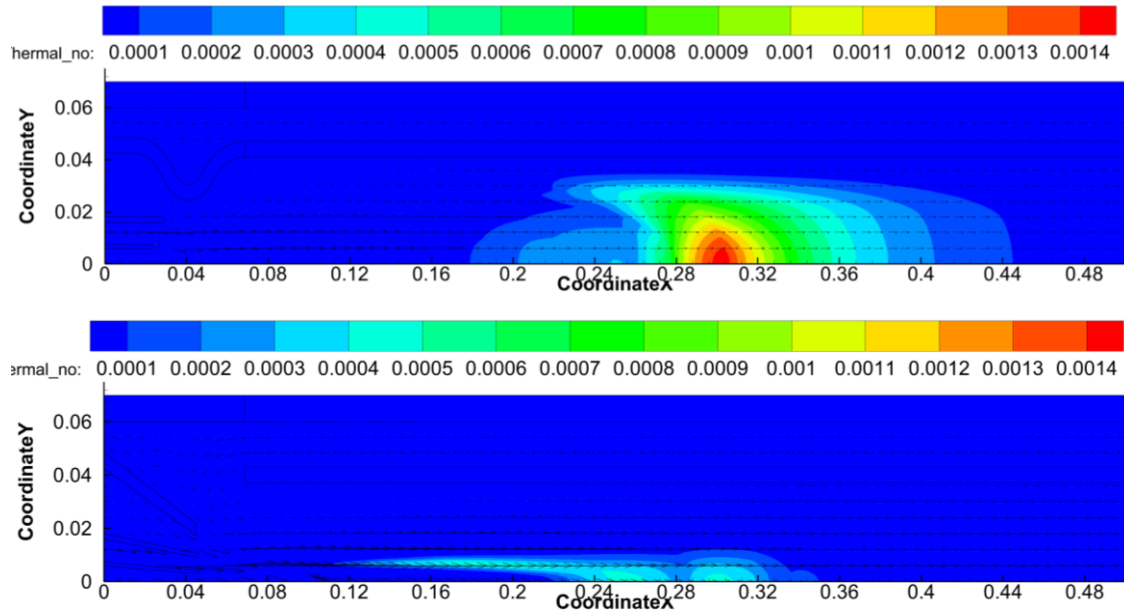


Figure 4.19 Contour of NOx formation rate[mol/m³s] between base case (top) and FGR (bottom). $\dot{Q}_{fuel} = 8.2$ kW (bottom). $\Phi = 0.72$.

It was found that the internal recirculation of the flue gas has reduced the NOx emission from 4493 ppmv (existing geometry) to 558 ppmv (proposed geometry). This emission level is comparable to the base case with natural gas in the unit of mg/Nm³. Furthermore, the thermal efficiency has increased from 29% to 39%. Table 4.7 tabulates this comparison. The increase in thermal efficiency has suggested that it has a better heat distribution in the burner and therefore to the radiant wall.

Table 4.7 Efficiency and NOx emission comparison for the cases at $\dot{Q}_{fuel} = 8.2$ kW and $\Phi = 0.72$.

| Case | NOx [ppmv] (dry) | O₂ [ppmv] | $\dot{Q}_{rad}$ [W] | Mass rate [kg/s] | Thermal efficiency $\eta_{th}$ | NOx [mg/Nm³] |
|---|---|---|---|---|---|---|
| Natural gas | 371 | 5.56 | 2128 | 0.004159 | 26% | 272.2 |
| Hydrogen | 4493 | 5.35 | 2374 | 0.003363 | 29% | 2126.3 |
| Hydrogen with FGR | 558 | 4.43 | 2594 | 0.003363 | 32% | 271.3 |

# Heat Transfer Analysis of the Furnace

In Chapter 4 it has been shown that the operation of the existing burner with hydrogen fuel can supply the same power as the current operation with natural gas. As the power supplied from the burner is indifferent, the heat treatment process in the furnace will not be affected when the fuel is switched to hydrogen.

However, different power could be applied for several reasons. The first reason is to comply with NOx regulation. To supply the same power using the existing burner, the NOx level will be higher with hydrogen fuel. Therefore, to obtain the same NOx level, the power supply must be lower. The second reason is to increase the processing speed. Higher thermal efficiency is expected with hydrogen combustion as discussed in Chapter 4. When the high NOx emission problem has been addressed, the operation could benefit from higher thermal efficiency, and possibly increase the processing speed.

A different burner supply power could affect the heat treatment process. A practical relation has been known that different temperature set point on the furnace's atmosphere changes the time requirement for the heat treatment process. Therefore, heat transfer analysis in the furnace was performed to understand the effects of having different burner power to the temperature of the furnace components. The simulation would also result in the relation of heat requirement per ton of product to the processing speed. This could be helpful for exploring the economic benefit of increasing processing speed in order to balance the higher cost of hydrogen fuel.

The structure of this chapter is as follows. First, the control parameters of the furnace are discussed in Section 5.1. Then, the geometry of the furnace and the components involved are introduced in Section 5.2. Next, In Section 5.3, the heat balance of the furnace is described. Next in Section 5.4, the model of the furnace is developed by determining the governing equations and boundary conditions. The result of the simulation is discussed in Section 5.5.

## 5.1 Control Parameters of the Furnace

The heat treatment process has three important control parameters. They are temperature, time, and atmosphere composition. The atmosphere composition is not affected by the type of fuel used. On the other hand, heat flux changes would impact temperature and processing time. They are related to each other. A practical relation has been known for the furnace being studied and is shown in Figure 5.1. In principle, the cycle time decreases with the increase in furnace temperature. Here, the furnace temperature is represented by atmosphere temperature. The cycle time is a time interval between batches of product incoming to the furnace.
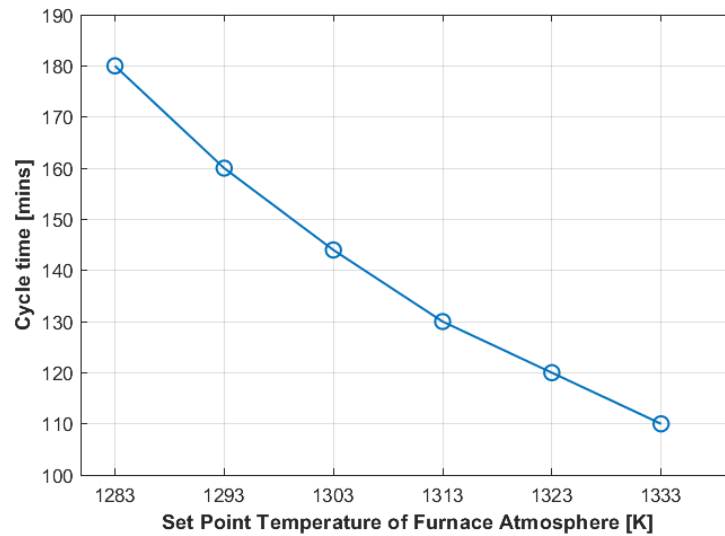
Figure 5.1: Relation of cycle time with the furnace's atmosphere temperature. [34]

## 5.2 Furnace components and geometry

The heat treatment furnace treats cast iron products at high temperatures. Every 2 hours (cycle time), 1 basket of cast iron product weighing ~750 kg comes into the furnace at 20 °C, while another one leaves the furnace at 680 °C. The product is the object which is heated. It is also called heat load. The use of product and load are used interchangeably in this report.

The furnace investigated in this work is a pusher type. It works by pushing in one product and pushing out one product every period of time. The period of time is also called cycle time. In the furnace, during every cycle, there are 39 baskets of product heated by 42 burners. A simplified representation of the furnace is shown in Figure 5.2. A detailed dimension of the furnace is presented in Figure B.5 in Appendix B.
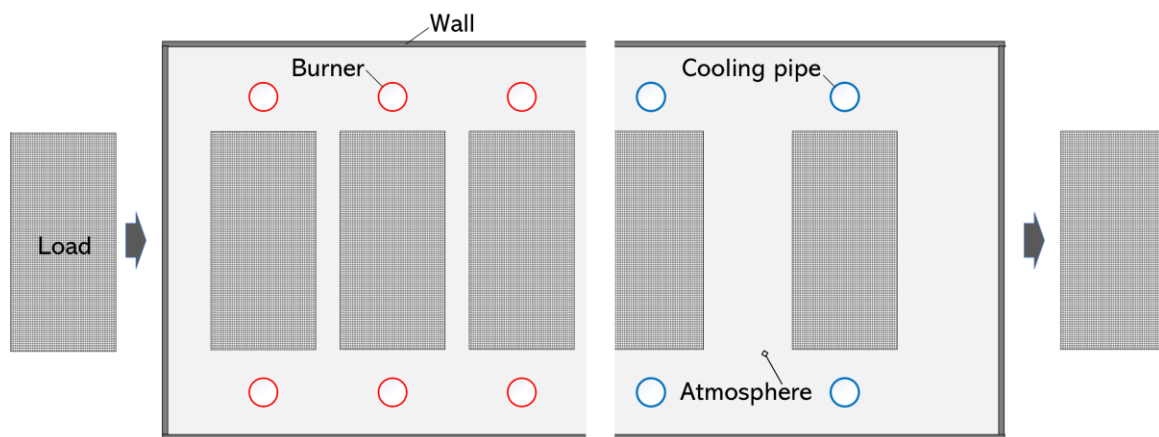


Figure 5.2: Top view representative of the furnace

## 5.3 Heat Balance

The heat treatment process requires the product to be maintained at a certain high temperature (~1323 K) for a long period of time. In this furnace, a product stays inside

46

the furnace for ~78 hours. The heat received from the burner is mainly used to maintain the high temperature inside the furnace. Reactions occur in the iron product and furnace atmosphere (see Table A.1 for the detailed reactions), and naturally that involves heat of reactions. Heat of reaction has been calculated for the series of reactions using the heat of reaction as tabulated in Table A.1. The rate for each of reaction is determined so that the resulted composition matches the equilibrium atmosphere composition (see Appendix A). The result shows that the heat of reaction contributes only 2% to the heat balance of the furnace. Therefore, it is not considered for the heat transfer analysis in this work.

The heat balance of the furnace is presented in Figure 5.3. The total fuel energy consumed is based on averaged consumption at Nefit Industrial [35]. A large portion of the heat is lost through the walls and a small portion loss through the atmosphere to the environment at the time a new basket enters the furnace. Only 19% of heat supplied from the burner is contained in the product upon leaving the furnace. Before leaving the furnace, the product is cooled to an acceptable temperature before coming in contact with uncontrolled ambient air. The cooling is performed using cooling pipes at the end of the furnace.
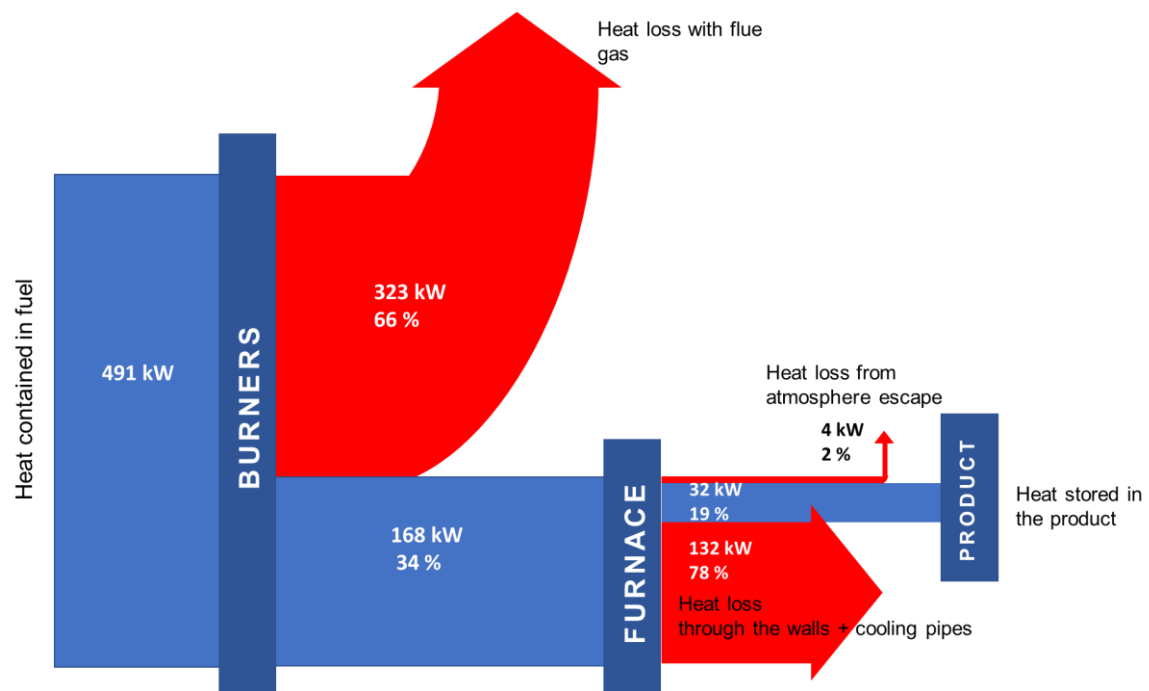


Figure 5.3: Heat balance of the studied heat treatment furnace.

## 5.4  Modeling of Heat Transfer

A visual representation of the furnace model is presented in Figure 5.4. The furnace is modeled as a 2-dimensional geometry. Another dimension is the furnace height, which is taken as 0.6 m. Half of the furnace is taken as the computational domain with a symmetry line as shown in the figure. There are 21 burners and 4 cooling pipes on the modeled half part of the furnace. There are 39 loads inside the furnace at any time. To simplify the model, it is assumed that each burner supplies the same amount of heat ($\dot{Q}_b$), and each cooling pipe rejects the same amount of heat ($\dot{Q}_c$). In reality, each burner can

supply different heat depending on the surrounding temperature it transfers the heat. A burner radiating to a lower load temperature would generally supply more power than to a higher temperature load. The temperature of the furnace atmosphere, however, for the most part, is equal, therefore it is expected that the assumption would not have a significant impact on the result.

The heat transfer interaction that occurs between the furnace components is as follows. Direct heat transfer between burner, load, and wall occurs by radiation. Conduction heat transfer is considered within the load and the wall. Heat transfer with atmosphere occurs only via convection. Heat loss through the walls is considered as well in this model.

The initial load temperature is 293.15 K. It is set as an initial condition. The heat loss from the wall to the environment is set as a boundary condition. The heat loss resistance is found to be 0.24 $K/W$. It is determined in Section 5.4.1.
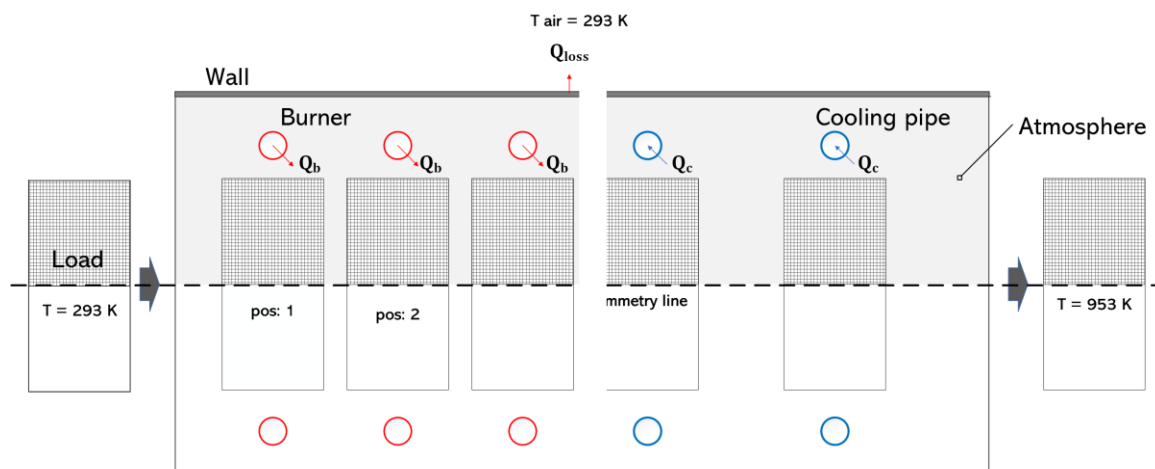


Figure 5.4: Visual representation of the furnace model

## 5.4.1 Mathematical model of the furnace

To obtain the temperature profile of each component of the furnace, the heat equation for each component must be formulated. These components are the loads (the iron products), burners, furnace's walls, and furnace's atmosphere. Since the product moves every two hours, the heat transfer analysis was done as a transient heat transfer. The heat equation is formulated as thermal circuit models, as presented in Kaviany [36] Chapters 3 and 4.

Several assumptions are applied to this model. Other than the assumption mentioned later during the model development, the following assumptions apply:

1. No heat of reaction both in the iron product and the atmosphere.
2. Radiation between walls and loads is not blocked off by the burner.
3. All burners have the same constant power $\dot{Q}_b$ despite the difference in the surrounding temperature it radiates.
4. The front, rear, top, and bottom walls are not considered since the evaluation was evaluated for 2D geometry.
5. To simplify the model, the height of the burner and furnace is equal to the height of the load (0.6 m). The actual height is 1.07 m.

6. The atmosphere in zone 5 to 28 is assumed to be well mixed due to the presence of fans and therefore has the same temperature.
7. No heat transfer occurs between burner to burner.

In this section, the heat transfer equations are formulated for the loads, burners, walls, and furnace atmosphere.

## Heat transfer equation of a load

The loads (iron products) are heated in the furnace. The load comes into the furnace at 293.15 K and leaves at 953.15 K. The load receives heat directly from the burners, and indirectly through wall reflection and furnace atmosphere. The heat transfer equation is first described for the conduction within the load itself, then radiation with burners and wall, and convection with the atmosphere.

### Conduction within the load

The load receives heat from burners mainly through radiation. Evaluation of conduction-radiation number, $Nr$, was done to determine whether the load can be assumed to have a uniform temperature. $Nr$ is a ratio of the temperature drop through the conductor to that between the radiating surfaces. Eq. 52 shows a formula to determine Nr value for radiation between solid's surfaces 1 and surface 3 and conduction within solid 1 [36]. In this case, object 1 is the load, and object 3 is the burner. This is a simplified formula assuming emissivity $\varepsilon_{r,1} = 1$, $\varepsilon_{r,3} = 1$ and view factor $F_{1-3} = 1$.

$$N_r = \frac{4\ \sigma_{SB}{T_m}^3 l_1}{k_1}$$

<div align="right">Eq. 52</div>

$k_1$ is the conductivity of the load. Conductivity values are listed in Table E.1. $l_1$ is the length of the conduction, which is the distance from the center of the load to its surface. $T_m$ is the radiant mean temperature between the load having a temperature $T_1$ of 1323 K and burner with temperature $T_3$ of 1360 K. It is calculated based on the following equation:

$$T_m = \left[\frac{\left({T_1}^2 + {T_3}^2\right)(T_1 + T_3)}{4}\right]^{1/3}$$

<div align="right">Eq. 53</div>

The $Nr$ value for the conduction within the load and its radiative interaction with the burner is 5.3. An $Nr$ value higher than 0.1 suggests that the conduction within the load is significant, and therefore it can't be treated as having a uniform temperature [36].

To capture temperature non-uniformity within the load, the load is divided into equally small volumes. Figure 20 shows a finite small volume analysis of two-dimensional, conductive heat transfer of the load. The two-dimensional model is chosen to simplify the calculation and because of less heat transfer interaction in the z-direction. The length in x-direction and y-direction are divided into 4 and 6 parts respectively. In total, 24 finite small volumes represent a load component. For the node (i, j), conductive heat transfer occurs with the neighboring nodes on the x-direction and y-direction.
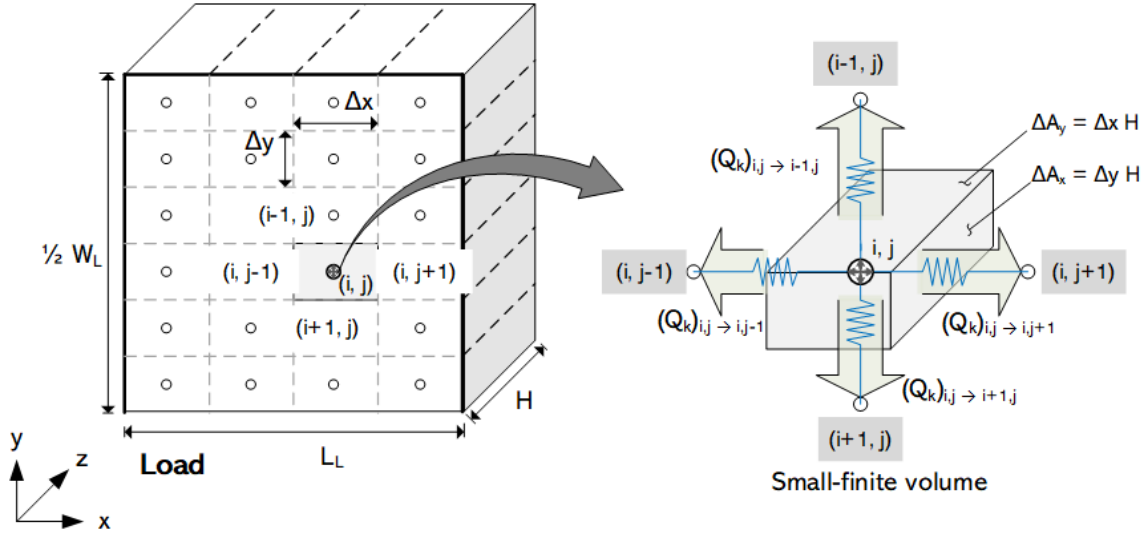
Figure 5.5: Finite-small volume analysis of conductive heat transfer on load

The conductive heat transfer equation for a small finite volume on node (i, j) $Q_k|_{\Delta V_{\{pos\}i,j}}$ to its neighboring nodes as shown in Figure 5.5 is:

$$Q_k|_{\Delta V_{L\{pos,i,j\}}} = (Q_r)_{L\{pos,i,j\} \to L\{pos,i-1,j\}} \qquad \text{Eq. 54}$$
$$+ (Q_r)_{L\{pos,i,j\} \to L\{pos,i+1,j\}}$$
$$+ (Q_r)_{L\{pos,i,j\} \to L\{pos,i,j-1\}}$$
$$+ (Q_r)_{L\{pos,i,j\} \to L\{pos,i,j+1\}}$$

Heat conduction between each node can be expressed in terms of thermal resistance $R_k$. Conduction from node i, j to the node i-1, j is equal to $(T_{L\{pos,i,j\}} - T_{L\{pos,i-1,j\}})/R_{k,\Delta x}$. Similarly, the conductive interaction with other nodes can be expressed as with their respective thermal resistance. The Eq. 52 now becomes:

$$Q_k|_{\Delta V_{L\{pos,i,j\}}} = \frac{T_{L\{pos,i,j\}} - T_{L\{pos,i-1,j\}}}{R_{k,\Delta x}} + \frac{T_{L\{pos,i,j\}} - T_{L\{pos,i+1,j\}}}{R_{k,\Delta x}} \qquad \text{Eq. 55}$$
$$+ \frac{T_{L\{pos,i,j\}} - T_{L\{pos,i,j-1\}}}{R_{k,\Delta y}} + \frac{T_{L\{pos,i,j\}} - T_{L\{pos,i,j+1\}}}{R_{k,\Delta y}}$$

where the thermal resistance for the conduction between finite volumes in the $x$-axis direction $R_{k,\Delta x}$ is:

$$R_{k,\Delta x} = \frac{\Delta x}{\Delta A_x\, k_L} \qquad \text{Eq. 56}$$

and the thermal resistance for the conductive heat transfer between finite volumes in the y-axis direction $R_{k,\Delta y}$ is:

$$R_{k,\Delta y} = \frac{\Delta y}{\Delta A_y\, k_L} \qquad \text{Eq. 57}$$

$\Delta A_x$ and $\Delta A_y$ are the heat transfer area for conduction in the x-axis and y-axis direction, respectively.

50

The loads receive heat from the burners through radiative heat transfer. Radiative heat transfer on the load occurs with burners, walls, and the neighboring loads. Figure 5.6 shows the thermal circuit diagram of these radiative heat transfer processes.
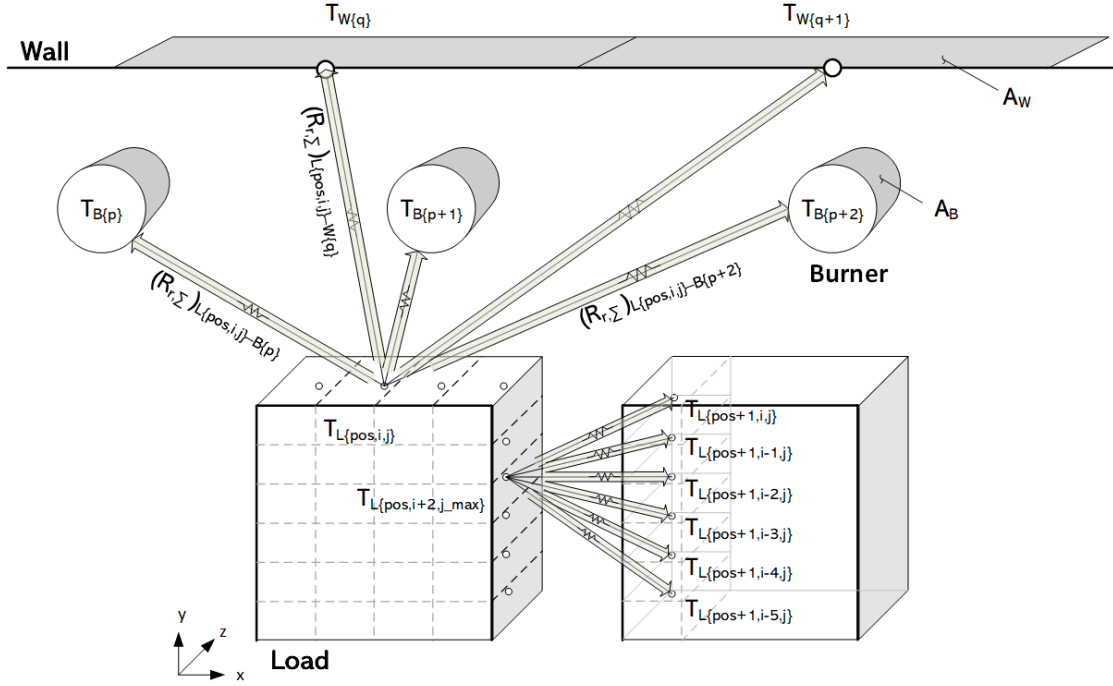


Figure 5.6: Radiative heat transfer between a load's finite volume to other furnaces components

### Radiative heat transfer between a load and its neighboring load

Radiative heat transfer from the node $L\{pos, i, j\}$ to the neighboring load $L\{pos + 1, i, j\}$ can be expressed as:

$$(Q_r)_{L\{pos,i,j\} \to L\{pos+1,i,j\}} = \frac{E_b(T_{L\{pos,i,j\}}) - E_b(T_{L\{pos+1,i,j\}})}{(R_{r,\Sigma})_{L\{pos,i,j\} \leftrightarrow L\{pos+1,i,j\}}} \qquad \text{Eq. 58}$$

where $E_b$ is the Stefan-Boltzman relation for total blackbody emissive power at temperature T, and is equal to $\sigma T^4$. The double arrow sign ($\leftrightarrow$) in total radiative thermal resistance $R_{r,\Sigma}$ indicates that the parameter gives the same value for either direction. The total radiative thermal resistance to the neighboring small finite volume is:

$$\left(R_{r,\Sigma}\right)_{L\{pos,i,j\} \leftrightarrow L\{pos+1,i,j\}} = \left(R_{r,\varepsilon}\right)_L + \left(R_{r,F}\right)_{L\{pos,i,j\} \leftrightarrow L\{pos+1,i,j\}} + \left(R_{r,\varepsilon}\right)_L \qquad \text{Eq. 59}$$

where the $R_{r,\varepsilon}$ is the surface-grayness resistance, which accounts for resistance from the emissivity of the load $\varepsilon_{r,L}$.

$$\left(R_{r,\varepsilon}\right)_L = \frac{1 - \varepsilon_{r,L}}{A_{r,L}\,\varepsilon_{r,L}} \qquad \text{Eq. 60}$$

$A_{r,L}$ is the radiative heat transfer area of the load. Its value is equal to $\Delta A_y$ for heat transfer with the burner.

The other thermal resistance is $R_{r,F}$. It is the resistance that accounts for the view factor $F$ from a load finite volume $L_{\{pos,i,j\}}$ to another load finite volume $L_{\{pos+1,i,j\}}$.

$$\left(R_{r,F}\right)_{L\{pos,i,j\} \leftrightarrow L\{pos+1,i,j\}} = \frac{1}{(A_r)_{L\{pos,i,j\}} \cdot F_{L\{pos,i,j\} \to L\{pos+1,i,j\}}}$$

$$= \frac{1}{(A_r)_{L\{pos+1,i,j\}} \cdot F_{L\{pos+1,i,j\} \to L\{pos,i,j\}}}$$

Eq. 61

View factor for radiation from load finite volume $L\{pos,i,j\}$ to $L\{pos+1,i,j\}$ $F_{L\{pos+1,i,j\} \to L\{pos,i,j\}}$ is calculated by Eq. 91 in Appendix C. $(A_r)_{L\{pos,i,j\}}$ is equal to $(A_r)_{L\{pos+1,i,j\}}$ and its value is $\Delta A_x$.

Radiative heat transfer between a load and a burner

Radiative heat transfer from the load at node $\{pos\}i,j$ having a temperature of $T_{L\{pos+1,i,j\}}$ to the burner $B$ at position $p$ with a temperature of $T_{B\{p\}}$ can be expressed as:

$$(Q_r)_{L\{pos,i,j\} \to B\{p\}} = \frac{E_b\left(T_{L\{pos,i,j\}}\right) - E_b\left(T_{B\{p\}}\right)}{\left(R_{r,\Sigma}\right)_{L\{pos,i,j\} \leftrightarrow B\{p\}}}$$

Eq. 62

The total heat transfer resistance $R_{r,\Sigma}$ is equal to:

$$\left(R_{r,\Sigma}\right)_{L\{pos,i,j\} \leftrightarrow B\{p\}} = \left(R_{r,\varepsilon}\right)_L + \left(R_{r,F}\right)_{L\{pos,i,j\} \leftrightarrow B\{p\}} + \left(R_{r,\varepsilon}\right)_B$$

Eq. 63

where $\left(R_{r,\varepsilon}\right)_B$ is the resistance due to the emissivity of the burner $\varepsilon_B$, which is equal to:

$$\left(R_{r,\varepsilon}\right)_B = \frac{1 - \varepsilon_{r,B}}{A_B \varepsilon_{r,B}}$$

Eq. 64

and the resistance due to the view factor $F_{L\{pos,i,j\} \to B\{p\}}$ can be expressed as:

$$\left(R_{r,F}\right)_{L\{pos,i,j\} \leftrightarrow B\{p\}} = \frac{1}{(A_r)_{L\{pos,i,j\}} \cdot F_{L\{pos,i,j\} \to B\{p\}}}$$

$$= \frac{1}{A_B \cdot F_{B\{p\} \to L\{pos,i,j\}}}$$

Eq. 65

$(A_r)_{L\{pos,i,j\}}$ is the radiative heat transfer area on the load finite volume, and is equal to $\Delta A_y$. View factor $F_{B\{p\} \to L\{pos,i,j\}}$ is calculated by Eq. 90 in Appendix C.

Radiative heat transfer between a load and a wall

The same type of equations apply for the radiative heat transfer from the load node $L\{pos,i,j\}$ to the wall at position $q$ with temperature $T_{W\{q\}}$ and emissivity of $\varepsilon_W$.

$$(Q_r)_{L\{pos,i,j\} \to W\{q\}} = \frac{E_b\left(T_{L\{pos,i,j\}}\right) - E_b\left(T_{W\{q\}}\right)}{\left(R_{r,\Sigma}\right)_{L\{pos,i,j\} \leftrightarrow W\{q\}}}$$

Eq. 66

## Total heat transfer equation of a load

Considering the above-mentioned heat transfer equations, the heat equation for each finite volume $L\{pos,i,j\}$ of the load at position $pos$ is:

$$Q|_{\Delta V_{L\{pos,i,j\}}} = Q_k|_{\Delta V_{L\{pos,i,j\}}} + \sum_{l=1}^{i_{max}} (Q_r)_{L\{pos,i,j_{max}\} \to L\{pos+1,l,1\}}$$

$$+ \sum_{l=1}^{i_{max}} (Q_r)_{L\{pos,i,1\} \to L\{pos-1,l,j_{max}\}} + \sum_{p=1}^{N_B} (Q_r)_{L\{pos,i,j\} \to B\{p\}}$$

$$+ \sum_{q=1}^{N_W} (Q_r)_{L\{pos,i,j\} \to W\{q\}} + (Q_h)_{L\{pos,i,j\} \to A\{pos\}}$$

Eq. 67

$N_B$, $N_B$, and $N_w$ are respectively the number of burners and wall divisions. $(Q_h)_{L\{pos,i,j\} \to A\{pos\}}$ is the heat transfer between the load finite volume and the atmosphere. It will be described later in this Section.

In a transient heat equation, the temperature changes if there's any heat accumulation in the load volume. The relation is shown in Eq. 68. The density $\rho$ and heat capacity $Cp$ values are provided in Table E.1 in Appendix E. The finite volume size is available in Table B.1 in Appendix B. The last term $\dot{s}_L$ in the last term of the equation is the volumetric energy conversion. The value is equal to zero since the reaction inside the load is not considered.

$$Q|_{\Delta V_{L\{pos,i,j\}}} = -(\rho\, Cp\, \Delta V)_L \frac{dT_{L\{pos,i,j\}}}{dt} + \dot{s}_L \Delta V_{L\{pos,i,j\}}$$

Eq. 68

## Heat transfer equation of the atmosphere

In this model, heat transfer to and from the furnace atmosphere occurs only via convective heat transfer. The atmosphere can be considered to be a non-participating gas because of its composition (9.1% $CO_2$ and 6.9% $H_2O$) and mean beam length (0.19 m from burner to load) gives an optical depth < 0.1 [37]. The heat transfer coefficient is obtained from Eq. 70. The Nusselt number for each geometry is calculated from the correlation equation as listed in Table D.1. The atmosphere velocity used to obtain the Reynolds on the correlation is obtained from Eq. 71. For a convective heat transfer from load finite volume $L\{pos,i,j\}$ to atmosphere at position $pos$ can be expressed as:

$$(Q_h)_{L\{pos,i,j\} \to A\{pos\}}$$
$$= h_{L\{pos,i,j\} \to A\{pos\}} (A_h)_{L\{pos,i,j\}} \left(T_{L\{pos,i,j\}} - T_{A\{pos\}}\right)$$

Eq. 69

$(A_h)_{L\{pos,i,j\}}$ is the heat transfer surface area. Its value can be $\Delta A_x$ or $\Delta A_y$ depending on which surface contacts with the atmosphere. The heat transfer coefficient $h_{L\{pos,i,j\} \to A\{pos\}}$ is equal to the product of Nusselt number $\langle Nu \rangle$ and atmosphere conductivity $k_A$ divided by the characteristic length $L_c$

$$h_{L\{pos,i,j\} \to A\{pos\}} = \frac{\langle Nu \rangle\, k_A}{L_c}$$

Eq. 70

Nusselt number $\langle Nu \rangle$ is obtained by correlation equation Eq. 92 in Appendix D. The required constants, that are specific to geometry and Reynolds number, are listed in Table D.1. Reynolds number depends on the flow speed of atmospheric gas $U_\infty$. For a system with a fan, the velocity can be obtained by Eq. 71. [38] [39]

$$U_\infty = \frac{\pi \, D_{fan}^2 / 4 \, H_{fan} R_{fan}}{A_{ws}}$$

Eq. 71

where $D_{fan}$, $H_{fan}$, and $R_{fan}$ are the diameter, height, and rotation speed of the circulation in the furnace, respectively. Their values are tabulated in Table B.1. $A_{ws}$ is the area of the load facing the flow direction of the atmospheric gas. The resulted $U_\infty$ is 2.32 m/s.

Eq. 72 describes the heat transfer equation of the atmosphere $A$ at location $pos$ considering its interaction with load finite volume at position pos on $i, j$ combination that contact the atmosphere, and burner and wall at position $p$ and $q$ respectively inside the atmosphere $pos$ formulated as follow:

$$Q|_{\Delta V_{A\{pos\}}} = \sum_i \sum_j (Q_h)_{L\{pos,i,j\} \to A\{pos\}} + (Q_h)_{B\{p\} \to A\{pos\}} + (Q_h)_{W\{q\} \to A\{pos\}}$$

Eq. 72

$$Q|_{\Delta V_{A\{pos\}}} = (\rho \, Cp \, \Delta V)_{A\{pos\}} \frac{dT_{A\{pos\}}}{dt} + \dot{s}_{A\{pos\}} V_{A\{pos\}}$$

Eq. 73

The density $\rho$ and heat capacity $Cp$ of the fluid is tabulated in Table E.3. Since no heat source is assumed on the atmosphere, the term $\dot{s}_{A\{pos\}} V_{A\{pos\}}$ is neglected.

## Heat equations of the burners and cooling pipes
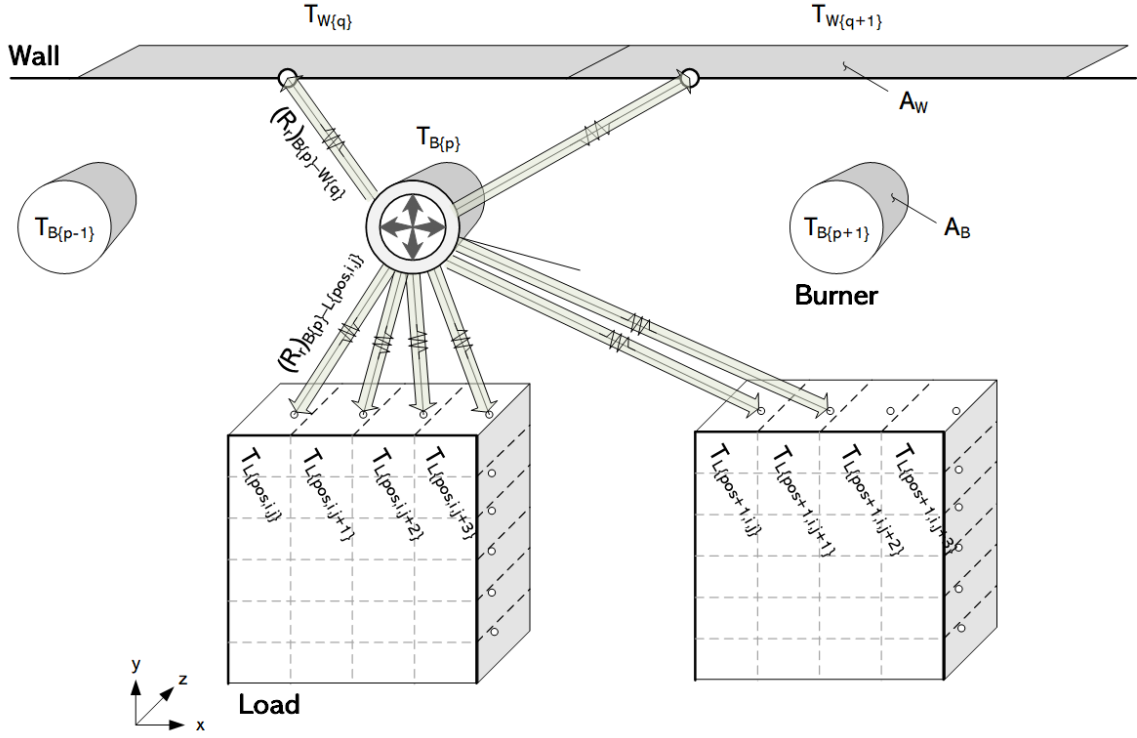


Figure 5.7: Radiative heat transfer between a burner and other furnace components

The heat equation for the burner $B$ at location $p$ is formulated as,

$$Q|_{V_{B\{p\}}} = \sum_{q=1}^{N_W}(Q_r)_{B\{p\} \to W\{q\}} + \sum_{pos=1}^{N_L}\sum_{j=1}^{j_{max}}(Q_r)_{B\{p\} \to L\{pos,1,j\}} + (Q_h)_{B\{p\} \to A\{pos\}}$$

Eq. 74

$$Q|_{V_{B\{p\}}} = -(\rho\,Cp\,V)_{B\{p\}}\frac{dT_{B\{p\}}}{dt} + \dot{s}_{b_k}V_{b_k}$$

Eq. 75

the source term $\dot{s}_{B\{p\}}V_{B\{p\}}$ is equal to burner power $Q_b$.

$$Q|_{V_{b_k}} = -(\rho\,Cp\,V)_{B\{p\}}\frac{dT_{B\{p\}}}{dt} + Q_b$$

Eq. 76

For cooling pipes $C$, a similar treatment applies, but the source term $\dot{s}_{c_k}V_{c_k}$ is equal to $Q_c$.

$$Q|_{V_{b_k}} = -(\rho\,Cp\,V)_{B\{p\}}\frac{dT_{C\{p\}}}{dt} + Q_c$$

Eq. 77

## Heat transfer equations of the walls
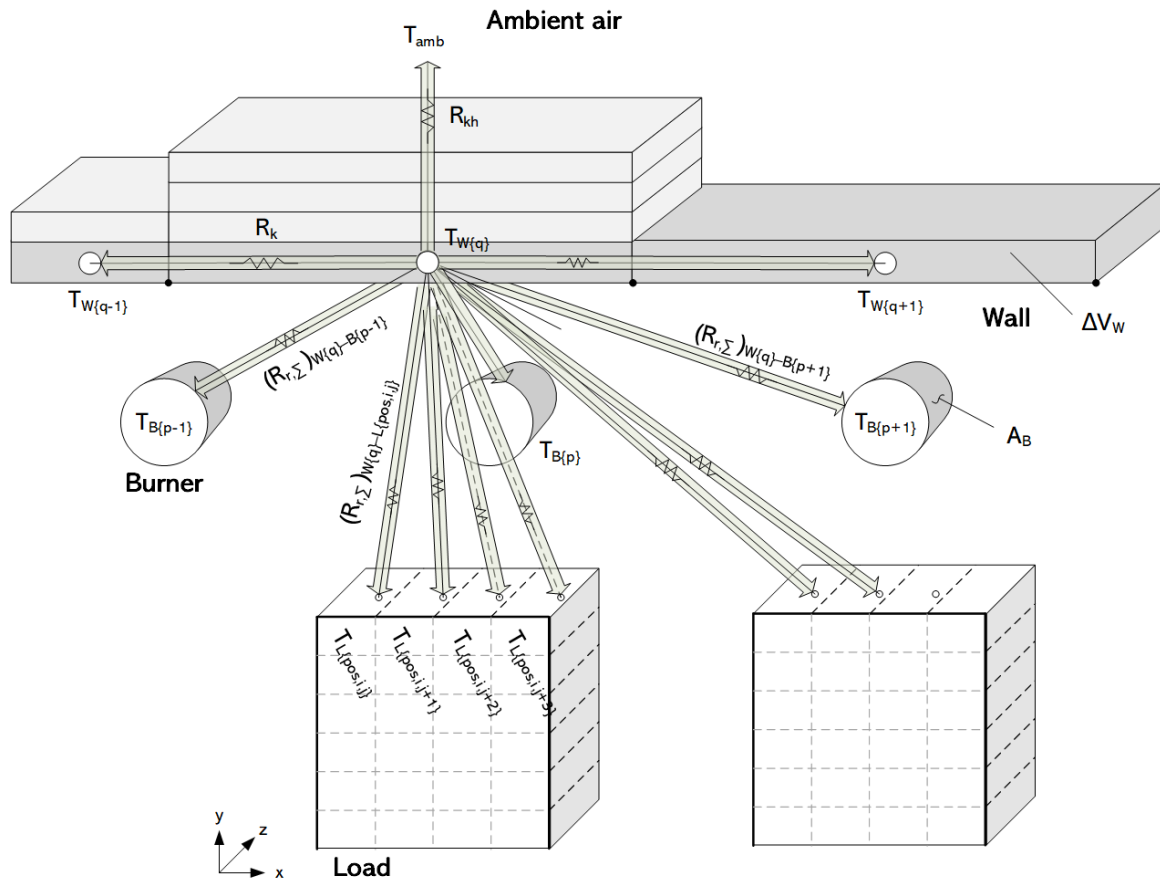


Figure 5.8: Radiative heat transfer between a wall part and other furnace components

The furnace wall is divided into 39 parts. Conductive heat transfer is considered between the wall part to its direct neighboring wall parts in the x-axis direction. The heat transfer is represented as:

$$Q_k|_{A_{W\{q\}}} = (Q_k)_{W\{q\} \to W\{q+1\}} + (Q_k)_{W\{q\} \to W\{q-1\}} \qquad \text{Eq. 78}$$

The walls are composed of several layers. Here, only the first inner layer (Layer 1 in Table 5.1) is physically considered. The other layers (Layer 2 – 5 in Table 5.1) are considered indirectly to estimate the heat resistance of heat loss to the environment. The heat equation of each wall part considers wall radiation interaction with burners and loads, convective heat transfer with the atmosphere, as well as conduction and heat loss. It is formulated as:

$$Q|_{\Delta V_{W\{q\}}} = \sum_{p}^{N_B} (Q_r)_{W\{q\} \to B\{p\}} + \sum_{pos=1}^{N_L} \sum_{j=1}^{j_{max}} (Q_r)_{W\{q\} \to L\{pos,1,j\}} \qquad \text{Eq. 79}$$
$$+ (Q_h)_{W\{q\} \to A\{q\}} + Q_k|_{A_{W\{q\}}} + Q_{loss}$$

$$Q|_{\Delta V_{W\{q\}}} = -(\rho \, Cp \, \Delta V)_{W\{q\}} \frac{dT_w}{dt} \qquad \text{Eq. 80}$$

The heat loss $Q_{loss}$ of the wall at position $q$ to the outside environment through the wall is expressed as:

$$Q_{loss} = \left(T_{W\{q\}} - T_{amb,\infty}\right)/R_{kh} \qquad \text{Eq. 81}$$

The heat loss resistance $R_{kh}$ is calculated based on the heat conductivity of the wall layers and convective heat transfer coefficient from the outer wall to the atmosphere. The conductivity and thickness of the wall layers are tabulated in Table 5.1. The ambient air temperature is assumed at 293.15 K. The convective heat transfer coefficient $h$ from the outer wall surface to the atmosphere is equal to $(k_f \langle Nu \rangle)/L$. The Nusselt number $\langle Nu \rangle$ correlation for the natural convective heat transfer is shown in Eq. 96 or Eq. 97. More explanation is provided in Appendix D.

Table 5.1: Furnace Wall Layers' Material Data

| Layer # | Material | Conductivity [36], $k$ | Thickness, $L$ |
|---------|----------|------------------------|----------------|
| | [-] | [W/m-K] | [m] |
| 1 | brick, fire clay | 1.6 | 0.259 |
| 2 | Insulating brick | 0.45 | 0.128 |
| 3 | Glass mat | 0.035 | 0.064 |
| 4 | Glass mat | 0.035 | 0.064 |
| 5 | Steel (AISI-304) | 15 | 0.140 |

### 5.4.2 Boundary conditions for the ODEs

To simulate the process, there are several constraints that shall be met by the solutions of the above-mentioned heat transfer equations (in ordinary differential equations (ODEs)). These are the boundary conditions. The first boundary condition is the initial temperature of the load. At position $pos = 1$ and initial time $t_{start}$, the load temperature is 293. 15 K

$$T_{L\{1,i,j\}}(t_{start}) = 293.15 \ K \qquad \text{Eq. 82}$$

for all small finite volume of the load i = 1, 2, ..., $i_{max}$ and j = 1, 2, ..., $j_{max}$.

As the load moves to the next location at a certain period, referred to as cycle time, the load temperature at location $pos + 1$ and initial time $t_{start}$ is equal to the load temperature at location $pos$ at the end of cycle time $t_{end}$. For every load at position $pos > 1$, the following relation applies,

$$T_{L\{pos+1,i,j\}}(t_{start}) = T_{L\{pos,i,j\}}(t_{end}) \qquad \text{Eq. 83}$$

The relation describes that the load temperature is continuous in time and position. The continuous temperature relation in time also applies to walls, burners, and atmosphere. For any wall at location $q$, the following mathematical expression applies

$$T_{W\{p\}}(t_{start}) = T_{W\{p\}}(t_{end}) \qquad \text{Eq. 84}$$

The heat is balanced between $t_{start}$ and $t_{end}$, therefore no heat is stored in the mass of walls, burner, nor atmosphere.

The burner temperature is continuous in time. Therefore, for any burner at location k, a similar boundary condition is applied.

$$T_{B\{p\}}(t_{start}) = T_{B\{p\}}(t_{end})$$
<div align="right">Eq. 85</div>

Here, $t_{start}$ is 0 hour, and $t_{end}$ is at 2 hours, unless otherwise stated.

### 5.4.3  Solver for ODEs with Boundary Conditions

The heat exchange processes influencing each component in the furnace have been formulated in Section 7.1, which results in several heat transfer equations in the forms of ordinary differential equations (ODEs). There are several boundary conditions that are required to be fulfilled as also presented in Section 5.4.2. In order to solve the equations, a solver for a boundary value problem called *bvp4c* in MATLAB is used. It is a finite difference code that implements three-stage Lobatta IIIa formula [40] [41] [42]. The formula provides a continuous solution that is fourth-order accurate uniformly in the interval of integration. Mesh selection and error control are based on the residual of the continuous solution. The solution is obtained when the residual has satisfied the set tolerance. In this work, the tolerance was 0.001.

Figure 5.9 presents a flowchart involved in simulating the furnace. The objective is to obtain the temperature for each component at any time and location.  The process starts by determining the input data, which are the thermal properties of the furnace components, values of heat supply power ($Q_b$) and heat rejection from each cooling pipes ($Q_c$), and heat resistance for the heat loss through the walls. Next, a set of formulated heat transfer equations relates to the temperature of each component to other components. The heat equations are solved in an iterative manner to obtain temperature that meets a set of boundary conditions. When the resulted temperatures are close to their respective previous values, the solution is found. Otherwise, iteration will be continued.
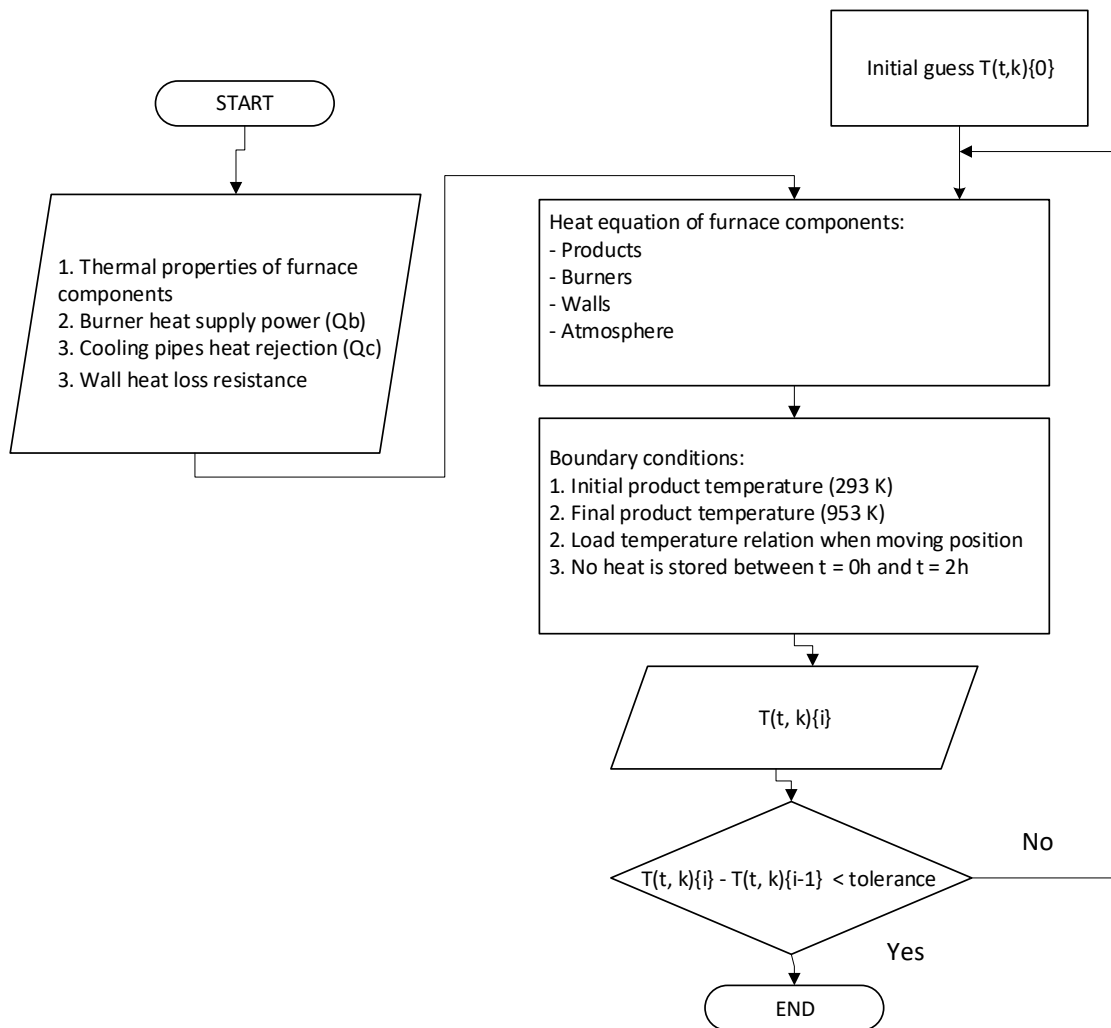
Figure 5.9: Flowchart of the furnace modeling

## 5.5  Result

The model estimates the temperature of furnace components at any time and location. The result is compared to measured operating data. The available measured data is the temperature of the furnace's atmosphere at several locations in the furnace. Figure 5.10 presents the simulated temperature of the furnace atmosphere and the measured values. The atmosphere temperature is rather constant across time, and therefore only averaged result is shown the figure. The simulation result is compared to this data. The figure shows that the simulation result agrees well with the measured data.
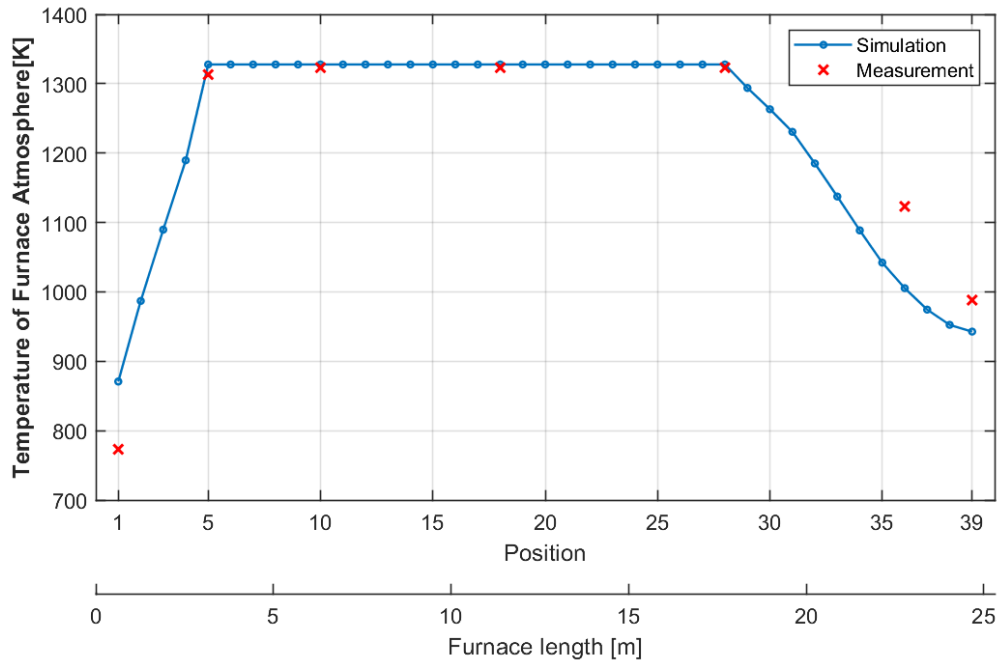
Figure 5.10: Comparison of furnace's atmosphere temperature profile from simulation result and measured data

On the burner simulation (Chapter 4), it is found that at the burner input power of $Q_{fuel}$ = 11.7 kW, the burner supply power to the furnace ($Q_b$) is equal to 4000 W. From the furnace simulation, it is obtained that the heat loss through the wall is: 65,248 W, and the heat rejection at cooling pipes is -735 W per pipe, to match the heat balance. The heat loss is obtained by Eq. 85. Heat rejection at cooling pipes is obtained by iteration to satisfy the product outlet temperature of 953 K. As the product leaves at a higher temperature than when it enters the furnace, the heat is stored in the load. The value is 15,812 W.

Figure 5.11 shows the temperature profile of the components in the furnace across the furnace length. The load starts with a temperature of 293 K and is heated up to ~ 1323 K inside the furnace. It is then cooled down to 953 K prior to exiting the furnace. The heat rejection at the end of the furnace is provided by a set of cooling pipes. As the burner provides the heat, the burner temperature is higher than other components. Conversely, the cooling pipe temperature is lower than other components as it receives heat. The atmosphere temperature, in general, is in between the temperature of the burner/cooling pipe, the load, and the walls. But at some locations due to the assumption of uniform atmosphere temperature, the atmosphere temperature can be higher than the burner temperature. This is physically possible since it receives heat from other zones.

The temperatures shown in Figure 5.1 for walls, atmosphere, and burners are the temperatures at t = 0 hrs and t = 2 hrs. As the temperature must meet continuity in time, the temperature at these two periods is the same. In between these periods, the temperature varies across time, as shown in Figure 5.12 for a sample of wall temperature.

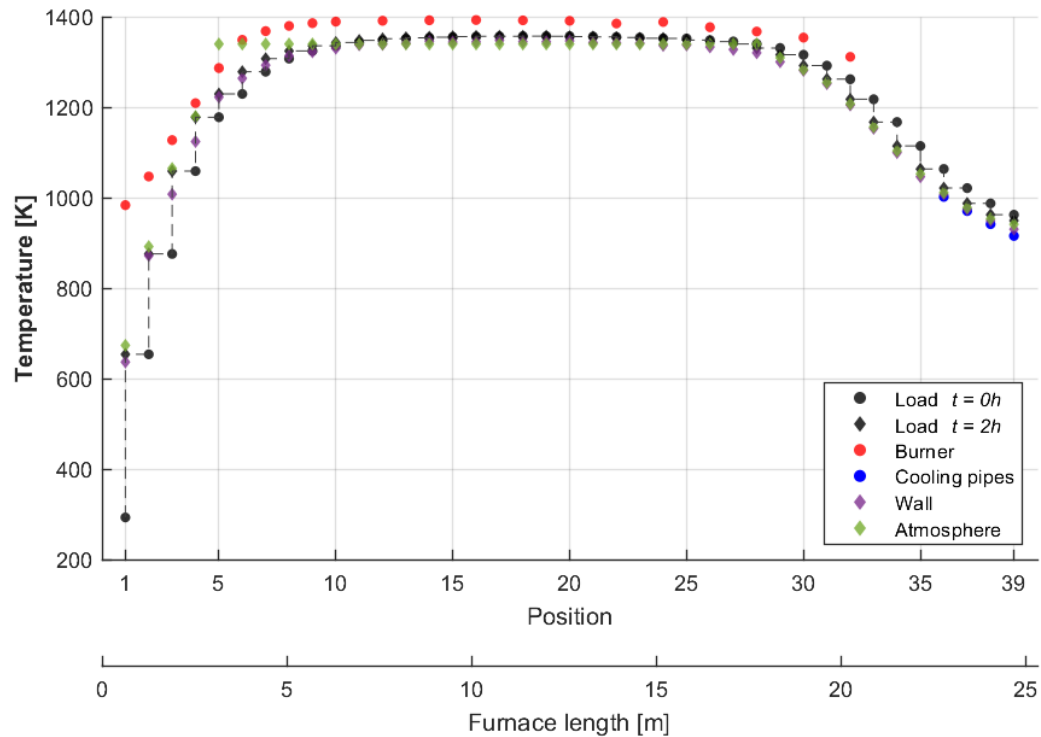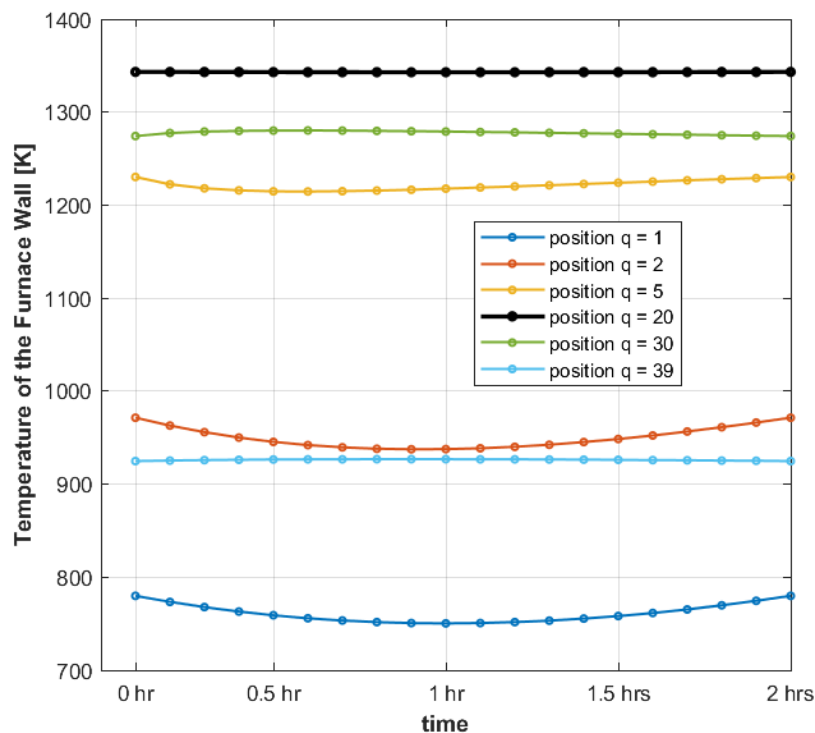Figure 5.11: Temperature profile of furnace components along the furnace length



Figure 5.12 Wall temperature at several different positions as a function of time

Evaluation of the conduction-radiation number, Nr, has shown that the load conduction has to be considered and that the load temperature is highly varying. Figure 5.13 shows the temperature contour of the product at several sample time and location. The product

starts with 293 K at time = 0 h and position = 1. As the time runs the load is heated until an average temperature of ~ 650 K, with higher temperature on the outside (750 K) and lower temperature in the inside (623 K). At time = 2 h, the product move to the next position. The product at location 1 is moved to location 2, therefore the temperature at pos =2 and t= 0 h is equal to the temperature at pos = 1 and t = 2h. In the middle part of the furnace, the temperature of the load is uniform as shown in position 15. The temperature is maintained at 1323 K for the heat treatment. The temperature contour in position 38 represents the load temperature during the cooling down. It shows that the temperature at the outside is lower than the inside.
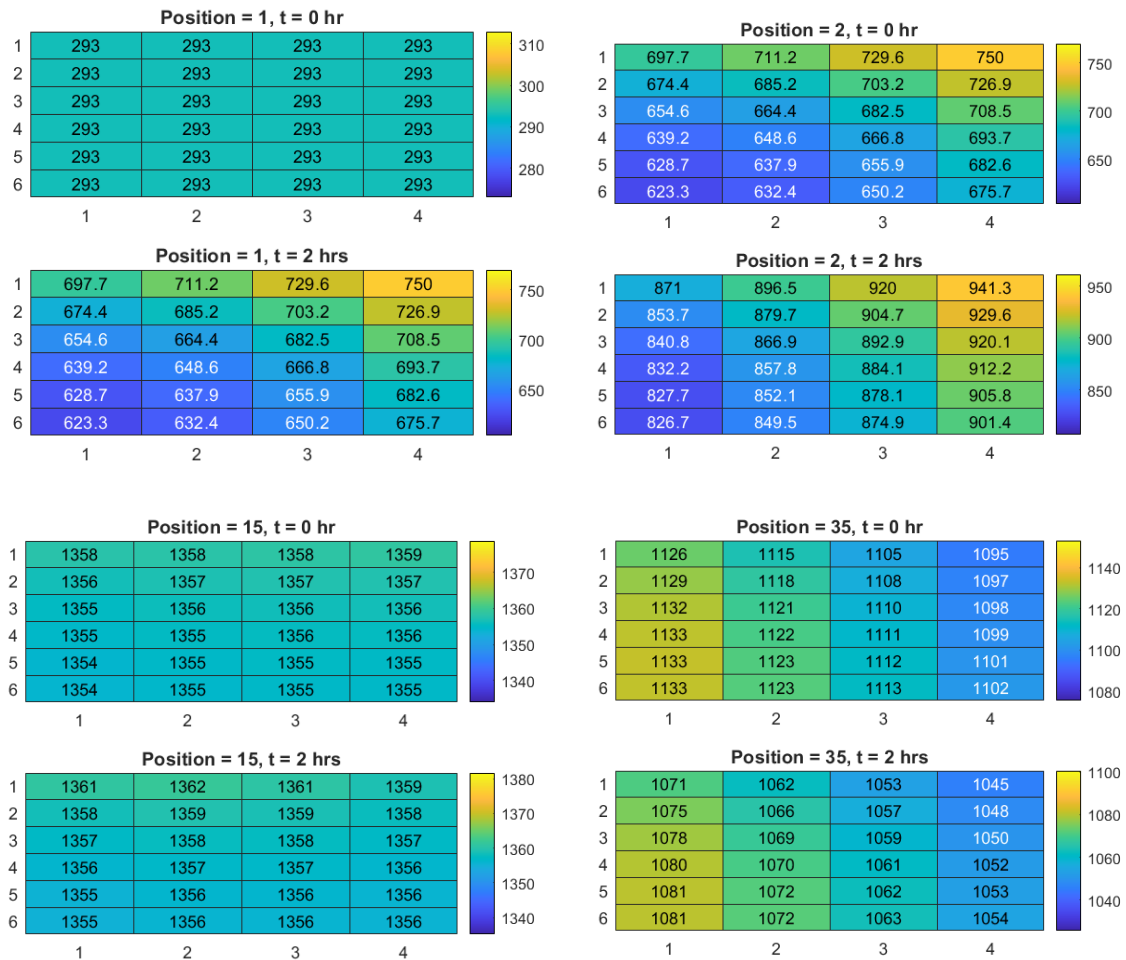


Figure 5.13: Temperature contour of a product at a different position (pos) inside the furnace and at time (t)

To understand the contribution of heat transfer rate from furnace components to the product, a sample heat transfer map is drawn for a product at position 3 and time = 2 hours. The heat map is shown in Figure 5.14. The load receives/delivers heat from/to the surrounding components. A negative value (written in red text) means that the load transfers the heat to the other component. On the opposite, a positive value (written in green text) means that the product receives heat from the other component. The biggest heat transfer occurs from the radiation between the load and the walls. The load finite volume shown in the figure receives 622 W net heat from the walls. The second biggest contributor is the burner with a net heat transfer of 406 W through radiation. The

product also receives heat from the product next to it. In total it receives 239 W from the neighbor loads. The heat transfer via convection is the lowest (147 W). The heat received by the product would raise its temperature. Through conduction, the heat is transferred to the core of the product. The number shows that the rate of heat transfer to the outer surface through radiation far exceeds the conduction rate to the core of the product.



Figure 5.14: Heat received by a sample of load finite volume from other furnace components (values in Watt)



Figure 5.15: Product temperature profile along the furnace length as a function of burner output power in Watt ($Q_b$).

Figure 5.15 shows the product temperature profile inside the furnace for different values of power $Q_b$. The output product temperature is set to 953 K in every case. In the middle part of the furnace, the temperature is held constant. The baseline case ($Q_b$ = 4000 W) has

a constant temperature at 1350 K. As the burner power increases, the temperature of the product at which being held constant also increases.

In Figure 5.16, the atmosphere temperature inside the furnace is plotted at different burner output power ($Q_b$). As expected, the temperature of the atmosphere reduces as the burner power is reduced. The atmosphere temperature could be used to determine the required processing time, as previously shown in Figure 5.1. Based on the specified atmospheric temperature (Ta) and cycle time, $Q_b$ and $Q_c$ can be calculated from the furnace model. The results are tabulated in Table 5.2. The values can be converted in terms of the required energy per ton of iron products. As shown in the Table, the higher the burner supply power, $Q_b$, the lower the heat requirement per kg of iron product.

Table 5.2: Required burner temperature and cooling pipes power based on specified Ta in cycle time

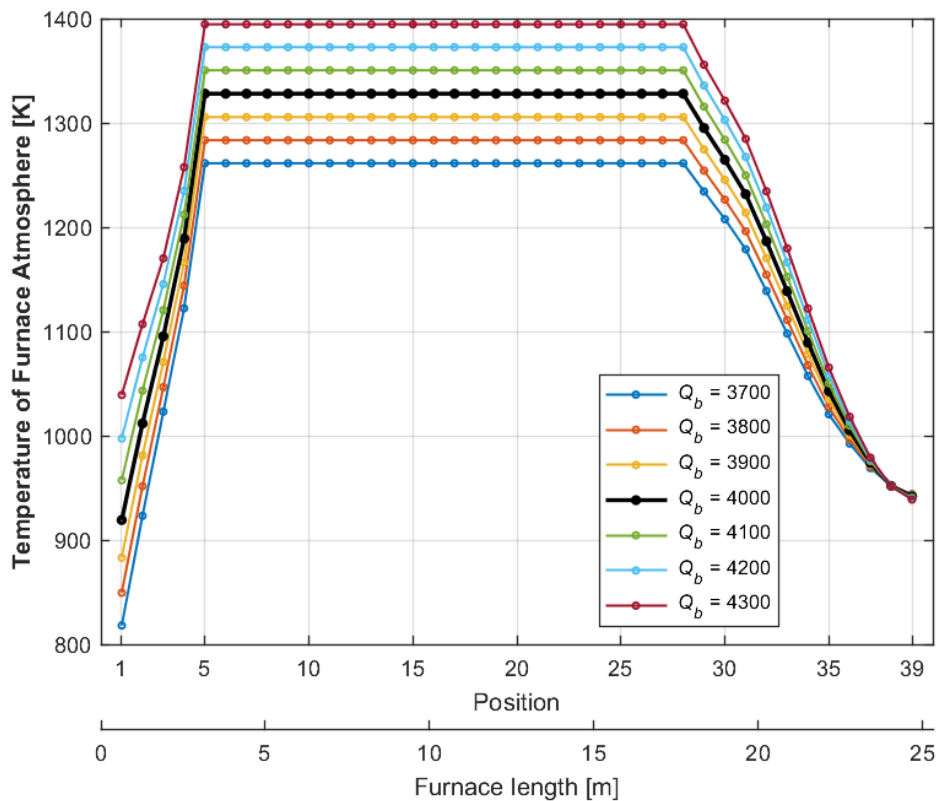| Atmosphere temperature, (Ta) | Cycle time | Qb | Qc | Energy/kg product |
|---|---|---|---|---|
| [K] | [mins] | [W] | [W] | kWh/kg |
| 1060 | 110 | 4166 | -985 | 427.7 |
| 1050 | 120 | 3996 | -717 | 447.6 |
| 1040 | 130 | 3848 | -489 | 466.9 |
| 1030 | 142 | 3702 | -272 | 490.6 |
| 1020 | 160 | 3535 | -38 | 527.9 |
| 1010 | 180 | 3386 | 0 | 568.8 |



Figure 5.16: Furnace's atmosphere temperature profile along the furnace length as a function of burner output power ($Q_b$).

In this study, the relation between burner power and the cycle can only be drawn on the available data for a cycle time range of 110 to 180 minutes. To be able to estimate the cycle time outside this range of data, a simulation involving these parameters are required: the rate of carbon diffusion from the inside to the surface of the iron product, rate of cementite decomposition to form graphite (C), and reaction rate between carbon and the atmosphere [43].

# Conclusion and Recommendations

In this study, the technical feasibility of fuel switching of a heat treatment furnace from natural gas to hydrogen was evaluated. The furnace receives the heat from 42 single-ended radiant tube burners, 11.7 kW each. Being a radiant tube burner, the combustion system is completely separated, and only heat transfer interaction might be affected when the fuel is changed. Another important parameter that might be affected is the generation of NOx emission, which could be a problem when using hydrogen fuel.

The evaluation was performed in two systems. The evaluation of the burner system aims to compare the thermal efficiency and NOx emission level between the combustion with natural gas and the burner. The second system is the heat treatment side of the furnace. The aim was to understand the relation between the burner power and the heat transfer inside the furnace and to assess the effect on the furnace performance.

## 6.1 Conclusion

A computational fluid dynamics (CFD) simulation of the burner was performed for the base case (natural gas combustion) and for hydrogen for several conditions. The result suggests that:

1. **The simulation result using the CFD model in this work are in good agreement with measured data of NOx emission for the base case (natural gas combustion).**

The CFD model in this work uses the standard k-ε model to calculate the Reynolds stress tensor, steady flamelet model to describe the combustion, a short version of GRI 3.0 mechanism for the natural gas kinetic mechanism, and a built-in NOx processing in commercial ANSYS Fluent to estimate NOx emission. The simulated NOx emissions are in good agreement with the measured data. The measured NOx emission at 5 kW and 12 kW thermal input powers are 125 ppm and 213 ppm, respectively. The simulated NOx emissions are 127 and 246 ppm, respectively.

2. **Thermal analysis has shown that the burner thermal efficiency is noticeably higher on the hydrogen combustion than the combustion with natural gas.**

Despite having a lower heat recuperation and lower emissivity of combustion products, the operation with hydrogen fuel has higher thermal efficiency than natural gas (add 3 – 4% efficiency). This is because the temperature of the combustion products is higher due to lower mass rate compared to the natural gas case. The higher temperature ensure that the radiant wall temperature is higher than the burner's outside temperature.

3. **The replacement of natural gas with hydrogen fuel on the existing studied burner is predicted to increase the NOx level by more than tenfold.**

The existing burner produces NOx emission at 125 ppm and 213 ppm at thermal input powers of 5 kW and 10.7 kW respectively. A comparable power for hydrogen combustion produces 1607 and 3952 ppm. There are several parameters that influence the thermal NOx formation, most importantly: temperature, radical oxygen concentration, and residence time. Higher NOx emission is mainly caused by higher local temperature for the combustion with hydrogen.

4. **It has been demonstrated that the modification of the existing burner to include internal flue gas recirculation (FGR) reduces NOx emission significantly.**

A modified burner geometry to include internal flue gas circulation was simulated. For the combustion with hydrogen, the NOx emission has reduced from 4493 ppm on the original geometry to 558 ppm on the design with FGR. The emission level in the unit of mg/Nm$^3$ is comparable to the base emission. FGR could reduce NOx emission because of 3 reasons. First, the local temperature was reduced due to the mixing of gases in the combustion zone with the flue gas with a lower temperature and a higher heat capacity. Secondly, it dilutes the oxygen radical concentration in the combustion zone. And third, it reduces residence time due to the large volume of recirculated gas. The result also suggests that the thermal efficiency is increased from 26% on the base case (natural gas) to 32%.

A second system, which is the process side of the furnace, was evaluated by simulating the transient heat transfer between the components (loads, walls, burners) of the furnace. The operation of the existing burner with hydrogen fuel can achieve the same power as the current operation with natural gas. As the supplied power from the burner is indifferent, the heat treatment process in the furnace will not be affected when the fuel is switched to hydrogen. However, different power could be applied in order to comply with the NOx emission level or to increase processing speed. An analysis of heat transfer in the furnace has been performed to understand the effects of having different burner supply power to the temperature of the furnace components. The result suggests that:

5. **The developed model predicts the actual process well.**

The simulation result has been compared to the measured data of furnace atmosphere temperature. The result shows that the simulation result agrees well with the measured data.

6. **The higher the burner power the lower the total heat consumption per ton product.**

A simulation result on different burner power and the atmospheric temperature has been correlated with the available information on the processing speed of the furnace. The result shows that the higher the burner power, the higher the atmospheric temperature, and the faster the processing speed. Due to the faster processing speed, the operation with higher burner power consumes less energy per ton of product.

## 6.1  Recommendations

Recommendation for future work includes:

1. To better capture the heat transfer on the heat exchanger fins, the 3D model shall be used in the burner simulation.
   In this model, the CFD simulation was performed in the 2D domain. The fins in the heat exchanger part were not captured perfectly, therefore could have different convective heat transfer than it should.
2. To improve the furnace model, the variations of burner supply power $Q_b$ over the furnace temperature should be considered. The same applies to the cooling pipe heat rejection power $Q_c$.
   In the furnace simulation, $Q_b$ and $Q_c$ are assumed constant despite the different temperature of the load and other furnace components. This could be improved by taking into account the temperature variable. It could improve the temperature prediction near the front and rear parts of the furnace.
3. A field test is recommended to be done to validate the simulation result to have confidence results.
   All the hydrogen simulation has not been validated. Even though the simulation agrees well with measured data on the natural gas cases, the result of hydrogen combustion could be not similar to the simulation result. However, the trend should be the same.
4. The metallurgical aspect needs to be accounted for to understand the relation of processing speed to burner power on the outside available data.
   In furnace simulation, the relation of processing speed with burner power is possible by having the relation of processing speed with the atmosphere temperature. However, the data is limited up to +10 mins and – 60 mins of the normal cycle time. To be able to find the full potential economic benefit of having higher burner power, the relation should be extended beyond the currently available one.
5. A follow-up study to evaluate and optimize the economic benefit and the associated cost is recommended.
   The study shows that the change to hydrogen fuel would increase the thermal efficiency of the burner. It is also demonstrated that higher burner power would reduce energy use per ton of product. It is recommended to have a follow-up study focusing on the economic feasibility to consider the investment cost, operating and fixed cost as well as the benefit mentioned above, as well as the environmental benefit.

# References

[1] "Data & Statistics - IEA." https://www.iea.org/data-and-statistics?country=WORLD&fuel=Energy consumption&indicator=Electricity final consumption by sector (accessed Mar. 11, 2020).

[2] C. Philibert, "Renewable Energy for Industry: From Green Energy to Green Materials and Fuels," 2017.

[3] A. de Pee, D. Pinner, O. Roelofsen, K. Somers, E. Speelman, and M. Witteveen, "Decarbonization of industrial sectors: the next frontier," *McKinsey Co.*, no. June, p. 68, 2018.

[4] S. Bourne, "The future of fuel: The future of hydrogen," *Fuel Cells Bull.*, vol. 2012, no. 1, pp. 12–15, 2012, doi: *10.1016/S1464-2859(12)70027-5.*

[5] X. J. L. Jr. Baukal, Vladimir Gershtein, Ed., *Computational Fluid Dynamics in Industrial Combustion.* CRC Press, 2000.

[6] D. M. Stefanescu and T. Ohio, "Classification and Basic Types of Cast Iron," *Cast Iron Sci. Technol.*, vol. 1, pp. 12–27, 2018, doi: *10.31399/asm.hb.v01a.a0006294.*

[7] C. E. Baukal, Ed., *Industrial burners: Handbook.* CRC Press, 2003.

[8] A. K. Agarwal, A. Pandey, S. Chaudhuri, and S. Sen, *Modeling and Simulation of Turbulent Combustion.* Springer Singapore, 2018.

[9] J. Warnatz, U. Maas, and R. W. Dibble, *Combustion: Physical and chemical fundamentals, modeling and simulation, experiments, pollutant formation.* Springer Berlin Heidelberg, 2006.

[10] ANSYS® Academic Research Mechanical, "ANSYS Fluent Theory Guide," *ANSYS Inc., USA*, vol. 15317, no. November, pp. 1–759, 2013.

[11] C. E. Baukal and S. Londerville, *The Coen and Hamworthy Combustion Handbook: Fundamentals for Power, Marine & Industrial Applications*, vol. 2. 2013.

[12] J. Hinze, *Turbulence*, 2d ed. New York: McGraw-Hill, 1975.

[13] R. K. Hanson and S. Salimian, "Survey of Rate Constants in the N/H/O System," in *Combustion Chemistry*, Springer New York, 1984, pp. 361–421.

[14] G. G. De Soete, "Overall reaction rates of NO and N2 formation from fuel nitrogen," *Symp. Combust.*, vol. 15, no. 1, pp. 1093–1102, 1975, doi: *10.1016/S0082-0784(75)80374-2.*

[15] M. F. Modest, *Radiative heat transfer, 2nd edition.* Elsevier Inc., 2003.

[16] Jiyuan Tu, Chaoqun Liu, and Guan-Heng Yeoh, *Computational Fluid Dynamics.* Elsevier, 2019.

[17] M. Flamme *et al.*, "Radiant Tube Burners," pp. 511–528, Jul. 2010, doi: *10.1201/EBK1420085280-31.*

[18] Mikron Instrument Company, "Table of Emissivity of Various Surfaces," 2014.

[19] J. Li, Z. Zhao, A. Kazakov, and F. L. Dryer, "An updated comprehensive kinetic model of hydrogen combustion," *Int. J. Chem. Kinet.*, vol. 36, no. 10, pp. 566–575,

2004, doi: *10.1002/kin.20026.*

[20]  X. Shi, J. Y. Chen, and Y. Chen, "Laminar flame speeds of stratified methane, propane, and n-heptane flames," *Combust. Flame*, vol. 176, pp. 38–47, 2017, doi: *10.1016/j.combustflame.2016.10.018.*

[21]  M. Ó Conaire, H. J. Curran, J. M. Simmie, W. J. Pitz, and C. K. Westbrook, "A comprehensive modeling study of hydrogen oxidation," *Int. J. Chem. Kinet.*, vol. 36, no. 11, pp. 603–622, 2004, doi: *10.1002/kin.20036.*

[22]  M. A. Mueller, T. J. Kim, R. A. Yetter, and F. L. Dryer, "Flow reactor studies and kinetic modeling of the H2/O2 reaction," *Int. J. Chem. Kinet.*, vol. 31, no. 2, pp. 113–125, 1999, doi: *10.1002/(SICI)1097-4601(1999)31:2<113::AID-KIN5>3.0.CO;2-0.*

[23]  K. Shimizu, A. Hibi, M. Koshi, Y. Morii, and N. Tsuboi, "Updated kinetic mechanism for high-pressure hydrogen combustion," *J. Propuls. Power*, vol. 27, no. 2, pp. 383–395, 2011, doi: *10.2514/1.48553.*

[24]  Z. Hong, D. F. Davidson, and R. K. Hanson, "An improved H2/O2 mechanism based on recent shock tube/laser absorption measurements," *Combust. Flame*, vol. 158, no. 4, pp. 633–644, 2011, doi: *10.1016/j.combustflame.2010.10.002.*

[25]  LOI Thermprocess, "Internal report: burners maintenance report," 2019.

[26]  T. Weydahl, J. Jamaluddin, M. Seljeskog, and R. Anantharaman, "Pursuing the pre-combustion CCS route in oil refineries - The impact on fired heaters," *Appl. Energy*, vol. 102, no. x, pp. 833–839, 2013, doi: *10.1016/j.apenergy.2012.08.044.*

[27]  "Increase of the Effective Energy from the Radiant Tube Equipped with Regenerative System in Comparison with Conventional Recuperative System." https://www.diva-portal.org/smash/record.jsf?pid=diva2%3A14358&dswid=-2059 (accessed Sep. 18, 2020).

[28]  C. Lowe, N. Brancaccio, D. Batten, C. Leung, and D. Waibel, "Technology assessment of hydrogen firing of process heaters," *Energy Procedia*, vol. 4, pp. 1058–1065, 2011, doi: *10.1016/j.egypro.2011.01.155.*

[29]  M. Ilbas, I. Yilmaz, and Y. Kaplan, "Investigations of hydrogen and hydrogen-hydrocarbon composite fuel combustion and NOx emission characteristics in a model combustor," *Int. J. Hydrogen Energy*, vol. 30, no. 10, pp. 1139–1147, 2005, doi: *10.1016/j.ijhydene.2004.10.016.*

[30]  ENTEC, "Appendix 1 LCPD Emission Limit Values," 2017.

[31]  G. Leek, "Activiteitenbesluit milieubeheer ; Staatsblad 2007 / 415 en bijgewerkt t / m Staatsblad 2019 / 227 Artikelen en voorschriften met toelichting," vol. 1, no. van 2, 2019.

[32]  C. E. Baukal and P. B. Eleazer, "Quantifying NOx for industrial combustion processes," *J. Air Waste Manag. Assoc.*, vol. 48, no. 1, pp. 52–58, 1998, doi: *10.1080/10473289.1998.10463664.*

[33]  C. E. Baukal and P. B. Eleazer, "Quantifying NOx for industrial combustion processes," *J. Air Waste Manag. Assoc.*, vol. 48, no. 1, pp. 52–58, 1998, doi: *10.1080/10473289.1998.10463664.*

[34]  Nefit Industrial, "Proces instructies Gloeierij," 2019.

[35]  Nefit Industrial, "Internal report: energie verbruiken," 2020.

[36]    M. Kaviany, *Principles of Heat Transfer*. New York: Wiley, 2002.

[37]    M. Kaviany, *Essentials of Heat Transfer*. Cambridge: Cambridge University Press, 2011.

[38]    Y. Zhou *et al.*, "Integrated numerical simulation and process optimization for solutionizing of aluminum alloys," *ASM Proc. Heat Treat.*, vol. 2006, pp. 1–8, 2006.

[39]    J. Kang and Y. Rong, "Modeling and simulation of load heating in heat treatment furnaces," *J. Mater. Process. Technol.*, vol. 174, no. 1–3, pp. 109–114, 2006, doi: *10.1016/j.jmatprotec.2005.03.037*.

[40]    J. Kierzenka and L. F. Shampine, "A BVP Solver Based on Residual Control and the MATLAB PSE," *ACM Trans. Math. Softw.*, vol. 27, no. 3, pp. 299–316, Sep. 2001, doi: *10.1145/502800.502801*.

[41]    Jacek Kierzenka, "Tutorial on solving BVPs with BVP4C," *MATLAB File Exchange*. https://nl.mathworks.com/matlabcentral/fileexchange/3819-tutorial-on-solving-bvps-with-bvp4c (accessed Aug. 23, 2020).

[42]    L. F. Shampine, I. Gladwell, and S. Thompson, *Solving ODEs with MATLAB*. Cambridge University Press, 2003.

[43]    M. Pirnat, P. Mrvar, and J. Medved, "A thermodynamic and kinetic study of the solidification and decarburization of malleable cast iron," *Mater. Tehnol.*, vol. 45, no. 6, pp. 529–535, 2011.

[44]    J. B. and M. J. Bibby, *Principles of Metal Manufacturing Processes*. Elsevier, 1999.

[45]    C. M. Hansson, *Cast iron technology*, vol. 114. 1989.

[46]    A. S. T. V. Rajan, C. P. Sharma, *Heat Treatment: Principles and Techniques*. PHI Learning Private Limited, 2011.

[47]    M. M. A. J.M. Smith, H.C. Van Ness, "Introduction To Chemical Engineering Thermodynamics - 7Th Ed - Book - Smith, Van Ness & Abbot.Pdf." 2005.

[48]    D. C. Hamilton and W. . Morgan, "Radiant-interchange configuration factors," *NASA TN 2836*, 1952.

[49]    J. Howell, "A Catalog of Radiation Heat Transfer Configuration Factors - Radiation Configuration Factors C-62." http://www.thermalradiation.net/sectionc/C-62.html (accessed Sep. 09, 2020).

[50]    J. Howell, "A Catalog of Radiation Heat Transfer Configuration Factors - Radiation Configuration Factors C-2." http://www.thermalradiation.net/sectionc/C-2a.htm (accessed Sep. 09, 2020).

[51]    C. H. Forsberg, *Heat Transfer Principles and Applications*. Elsevier, 2020.

[52]    M. Kaviany, *Principles of Heat Transfer*. Wiley, 2001.

[53]    S. W. Churchill and H. H. S. Chu, "Correlating equations for laminar and turbulent free convection from a vertical plate," *Int. J. Heat Mass Transf.*, vol. 18, no. 11, pp. 1323–1329, Nov. 1975, doi: *10.1016/0017-9310(75)90243-4*.

# Metallurgical Information

In this Appendix, additional information about the heat treatment process is described. This is resulted from documentation at Nefit Industrial [34] and a literature study from Bibby et al [44], Hansson et al [45], and Rajan et al [46].

The main use of heat treatment is to improve the mechanical properties of casting compared to those displayed in the as-cast condition. Malleable cast iron is made by heating white cast iron to temperatures in the range of 820-1000 °C for several days. White cast iron consists of cementite ($Fe_3C$) and pearlite. Pearlite is a two-phased, lamellar (or layered) structure composed of alternating layers of mostly ferrite and some cementite. By the process of controlled annealing treatment, the metastable phase ($Fe_3C$) decomposes into free carbon (C) and iron (Fe) as represented by the reaction:

$$Fe_3C \leftrightarrow 3\,Fe + C \qquad \text{Eq. 86}$$

The decomposition of the cementite forms carbon flakes in a perlitic matrix, as shown in Figure A.1. The process changes the structure from cementite into perlite and decarburizes the surface to become ferrite. Malleable cast iron has good shock resistance and machinability, with much-improved strength and ductility compared to white cast iron. [44]
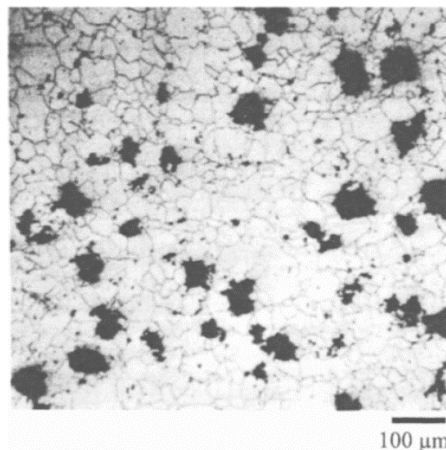


Figure A.1: Microstructure of malleable cast iron; black phase is the carbon flake (graphite). [44]

The microstructure of white-heart malleable cast iron depends on section size. Small sections contain pearlite and temper carbon in a ferritic substrate. Large sections contain three different zones: (1) the surface zone which contains pure ferrite; (2) the

intermediate zone which has ferrite pearlite, and temper carbon; (3) the core zone containing pearlite, temper carbon, and ferritic inclusions. The combination of different microstructure in several zones makes it a good combination of strong and ductile.
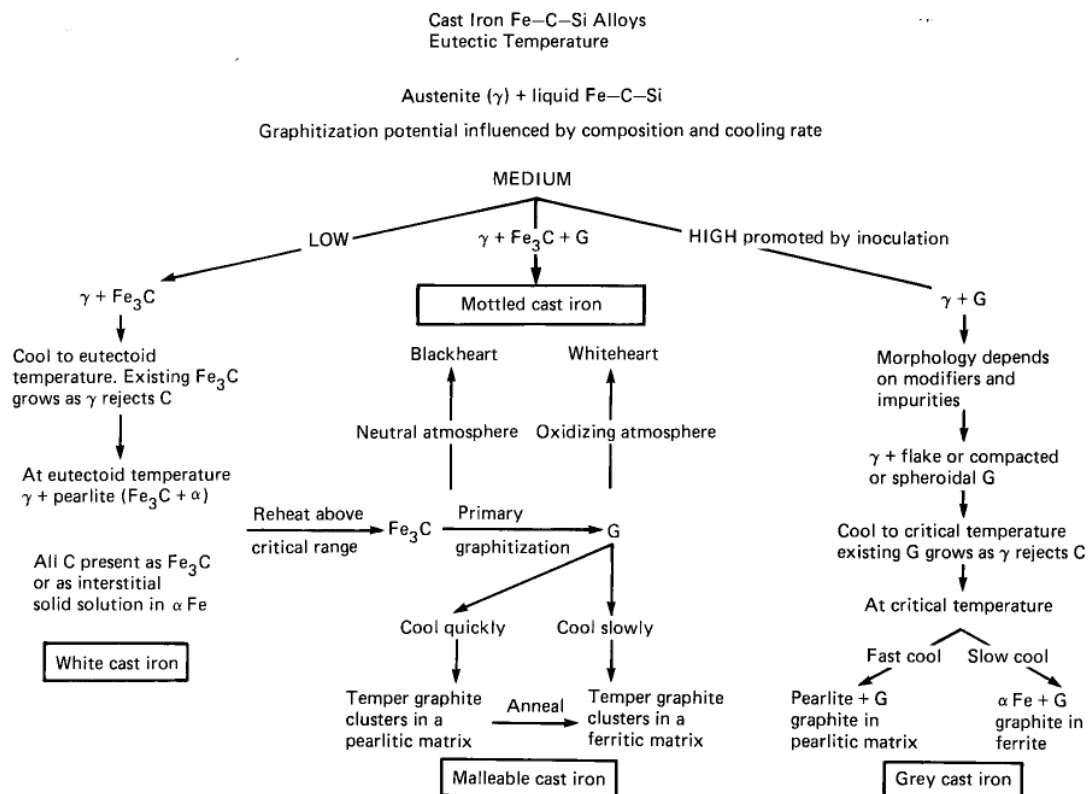


Figure A.2: Basic processing to obtaining common commercial cast irons [6]

Malleablizing is performed in batch-type or continuous furnaces. White-heart malleable irons are annealed in a decarburizing atmosphere. The decarburization reactions remove the carbon (as produced in Eq. 86) in the iron material by reacting it with the atmospheric gases. The decarburization reactions are as follows:

$$C + CO_2 \leftrightarrow 2\,CO \qquad\qquad \text{Eq. 87}$$

$$C + H_2O \leftrightarrow CO + H_2 \qquad\qquad \text{Eq. 88}$$
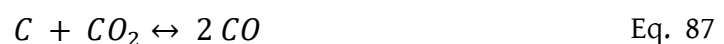
A decarburizing atmosphere for white-heart malleable irons is achieved by controlling the CO/CO2 ratio in the atmosphere. The proportion of gases present in the atmosphere is controlled by the equation:

$$H_2 + CO_2 \leftrightarrow CO + H_2O \qquad\qquad \text{Eq. 89}$$

The equilibrium constant of this reaction at 1060 °C is 2.1. If the $CO/CO_2$ ratio, which is monitored during annealing, is maintained at 2.7, the $H_2/H_2O$ ratio is 1.3, and the atmosphere composition will be 24.5% CO, 9.1% $CO_2$, 6.9% $H_2O$, 9.0% $H_2$, and 50.5% $N_2$ [45]. The heat of reaction for each reaction is tabulated in Table A.1.

Table A.1 Heat of reaction associated with the heat treatment process[43]

| Decarburization (at the iron body) | Heat of reaction [47] |
|---|---|
| $C_{(s)} + CO_{2\,(g)} \rightarrow 2\,CO_{(g)}$ | $\Delta H$ = 172.5 kJ/mol |
| $C_{(s)} + H_2O_{(g)} \rightarrow CO_{(g)} + H_{2\,(g)}$ | $\Delta H$ = 131.3 kJ/mol |
| **Regeneration (at the furnace atmosphere)** | |
| $2\,CO_{(g)} + O_{2\,(g)} \rightarrow 2\,CO_{2\,(g)}$ | $\Delta H$ = -566 kJ/mol |
| $CO_{(g)} + 2\,H_2O_{\,(g)} \rightarrow CO_{2\,(g)} + 2\,H_{2\,(g)}$ | $\Delta H$ = 200.6 kJ/mol |
| $2\,H_{2\,(g)} + O_{2\,(g)} \rightarrow 2\,H_2O_{(g)}$ | $\Delta H$ = -241.8 kJ/mol |

## Furnace Operations

In Nefit Industrial, the heat treatments are performed in three furnaces. Two furnaces (Furnace II and III) operate with natural gas, while the other one (Furnace I) operates with both electricity and natural gas. All the furnaces run 24 hours a day. The furnaces account for roughly 80% of the total natural gas consumption and 12% of total electricity consumption in the factory. In total, they account for around 40% of total energy consumption. Depending on the product quality to be produced, the product is treated into different (combination of) furnaces. Figure A.3 shows a combination of heat treatment furnaces used to achieve different grades of products. The product grades produced in Nefit Industrial according to DIN (Deutsches Institut für Normung) standards are EN-GJMW-400-5, EN-GJMW-450-7, EN-GJMW-360-12, EN-GJMW-550-4.
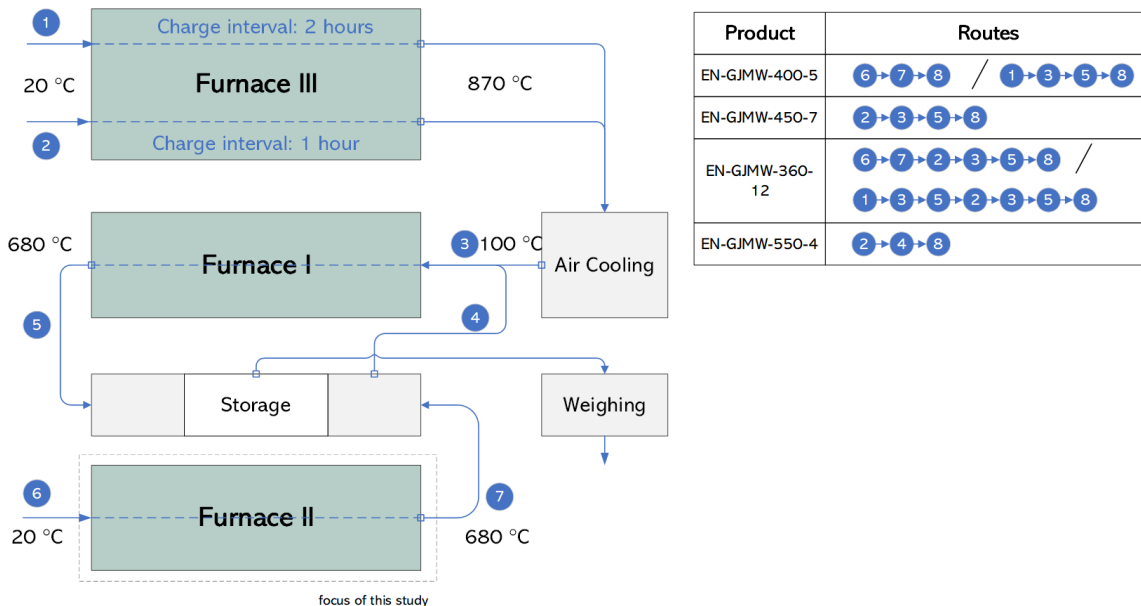


Figure A.3: Flow diagram of the heat treatment process producing white-heart malleable iron with different grades [34]

The decarburization process occurs in Furnace II and III. The oxidizing atmosphere in the furnaces is controlled at certain compositions (as previously mentioned in Sec 2.1).

Meanwhile Furnace I provides additional heat treatment required to get the globular cementite structure. The atmosphere in this furnace consists of protective gases, which means that no decarburization occurs in this furnace. The protective atmospheric gases are obtained and processed from the flue gas from one of the burners in Furnace III.

There are three important parameters affecting the quality of the product, which are temperature, time, and atmosphere composition. The temperature profile and the number of charges in different zones in each furnace are shown in Figure A.4. One charge contains several cast iron products to be heat-treated. The charge is fed into the furnace one at a time with an interval time specified and provided in the figures. All the charges inside the furnace move forward accordingly at the same time once every interval time. In total, there are 42, 40, and 41(x 2) charges in Furnace I, II, and III, respectively.
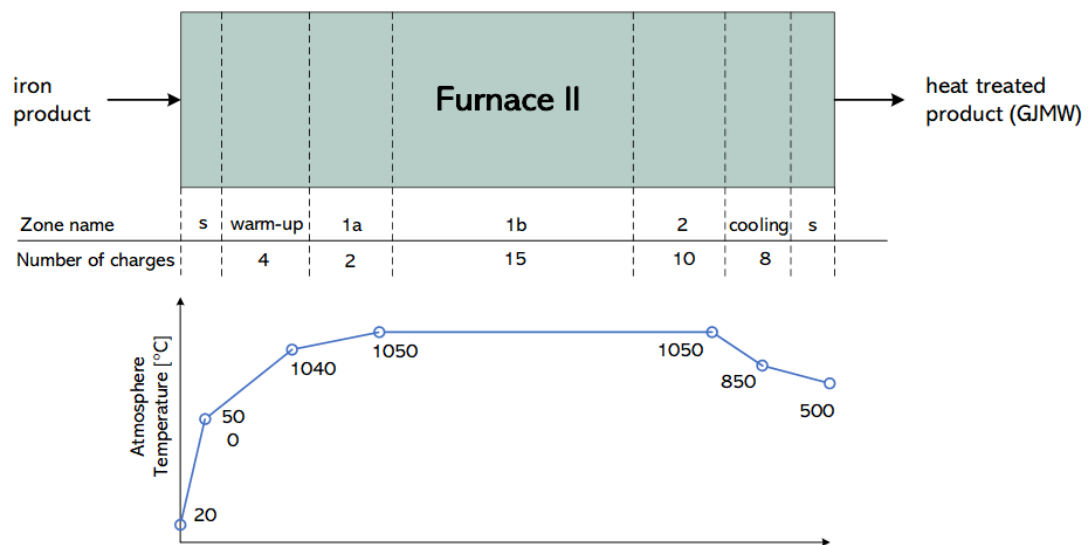


Figure A.4: The scheme for Furnace II [34]

# Detailed dimensions

A simplified burner geometry is used for the simulation in a 2-dimensional (2D) domain as previously described Section in 3.1. The detailed dimension is shown in Figure B.1.
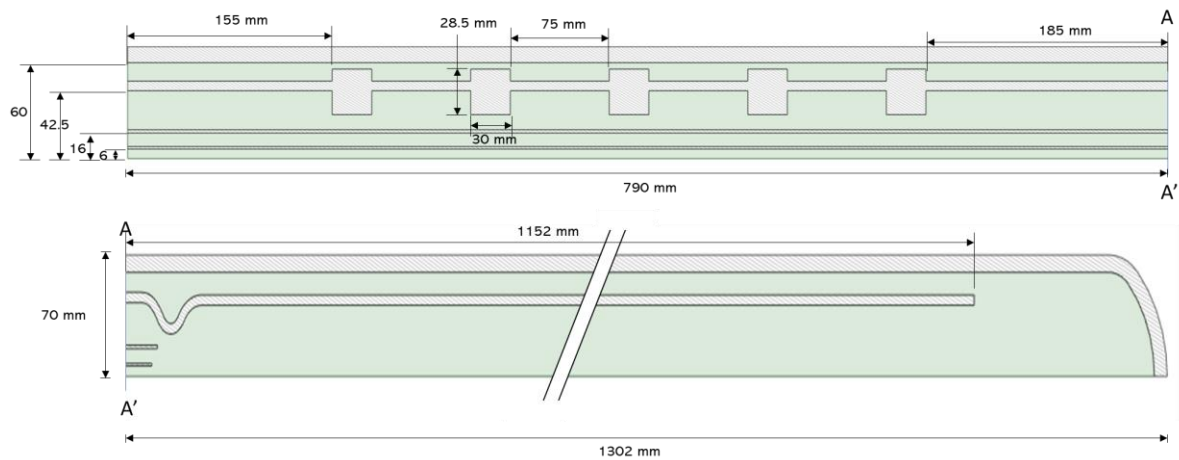


Figure B.1: Dimension for burner simulation domain

The simulation domain was derived from the actual physical domain of a burner in Nefit Industrial. The actual geometry of the burner and the dimensions are shown in Figure B.3,  Figure B.4, and Figure B.4. Figure B.3 and Figure B.3 show the dimensions of the combustion zone and the recuperation zone, respectively.
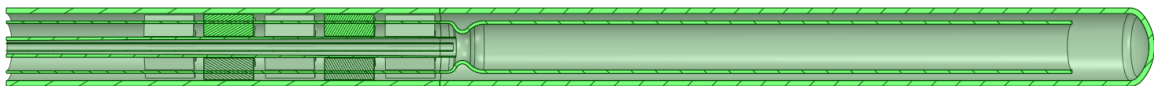


Figure B.2: Complete geometry of the burner
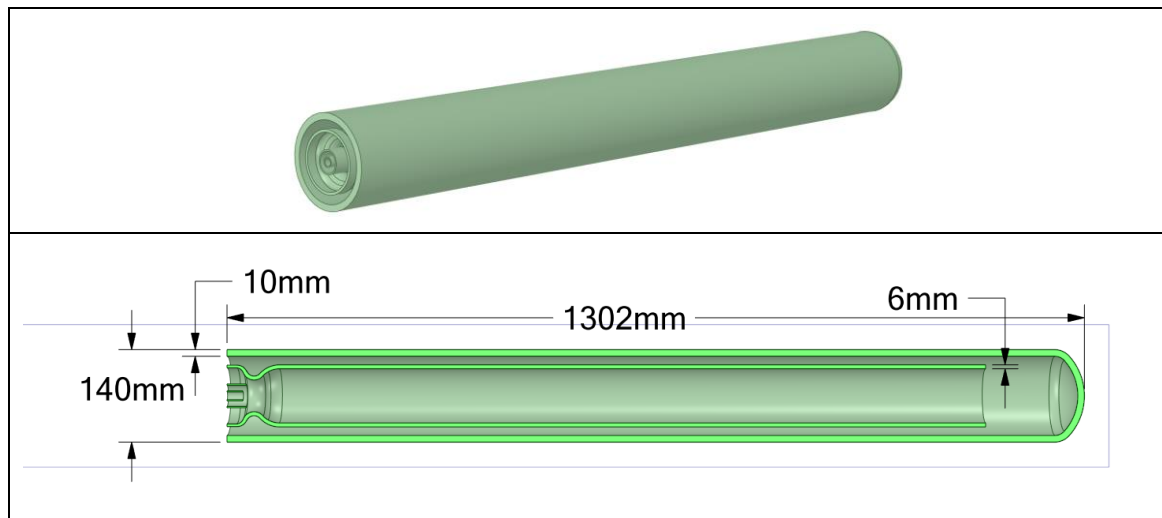
Figure B.3: Dimension of the burner (combustion zone)
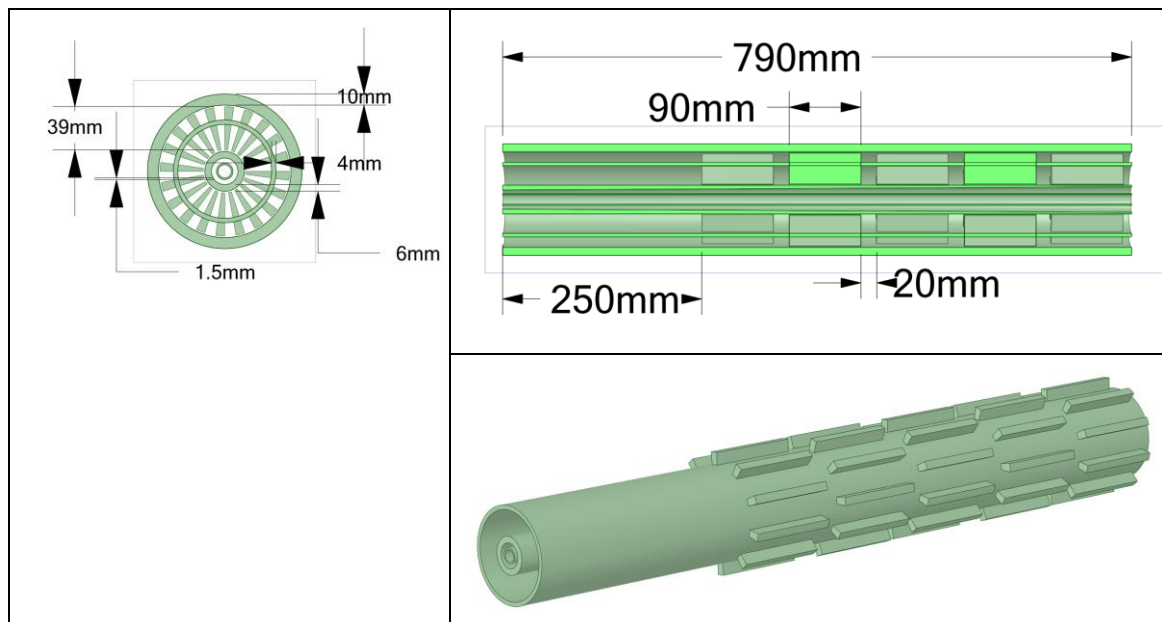


Figure B.4: Dimension of the burner (heat recuperation zone)

The furnace simulation in Chapter 5 was simulated in a 2-dimensional domain. The geometry and dimension represent the actual furnace in Nefit Industrial. The detailed dimension used in the simulation is shown in Figure B.5.
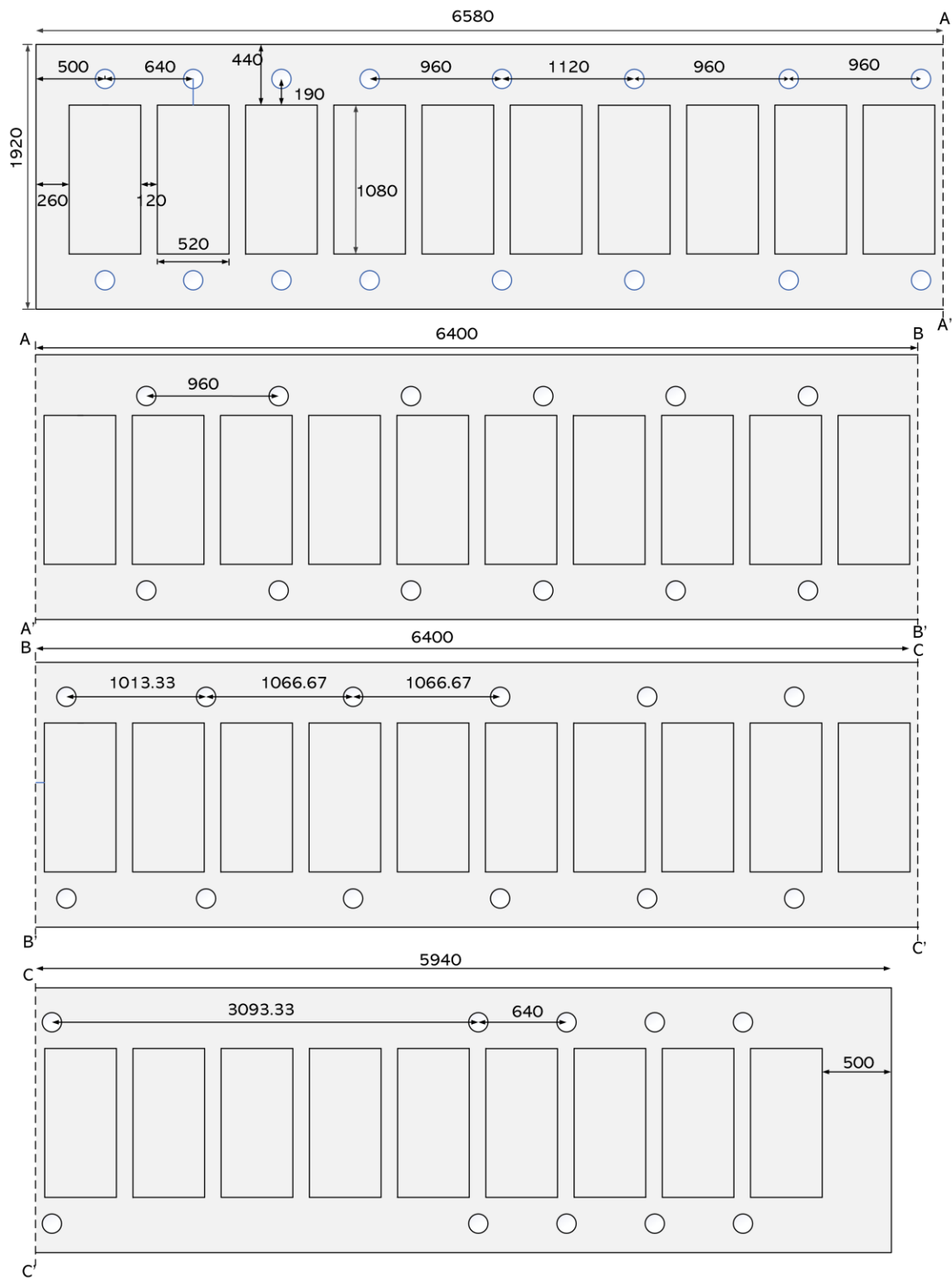
Figure B.5: Representative drawing of the heat treatment furnace

Some dimensions were defined earlier in Section 5.4.1. The values are tabulated in Table B.1.

Table B.1: Dimensions of load, burner, fans used in the furnace simulation

| Parameter | Value | Parameter | Value |
|---|---|---|---|
| Load dimensions | | Furnace dimensions | |
| Length ($L_L$) | 0.52 m | Length ($L_F$) | 25.32 m |
| Width ($W_L$) | 1.08 m | Height ($H_F$) | 0.6 m |
| Height ($H$) | 0.6 m | Width ($W_F$) | 1.92 m |
| Finite volume length ($\Delta x$) | 0.13 m | Fan dimensions | |
| Finite volume width ($\Delta y$) | 0.09 m | Diameter ($D_{fan}$) | 0.64 m |
| Finite volume ($\Delta V$) | 7.02 x 10$^{-3}$ m$^3$ | Height ($H_{fan}$) | 0.11 m |
| Burner dimensions | | Rotation speed ($R_{fan}$) | 1700 rpm |
| Surface Area ($A_B$) | 0.264 m$^2$ | | |
| Height ($H$) | 0.6 m | | |
| Thickness ($t_B$) | 0.1 m | | |
| Outer diameter ($D_B$) | 0.14 m | | |

# Radiation View Factor

In Section 5.4.1, radiative heat transfer between several geometries was developed. The view factor is one of the parameters that determine the rate of radiative heat transfer. A view factor $F_{12}$ is the proportion of the radiation that leaves surface 1 to another surface 2. In this work, the geometry for view factor from burner surface (surface with area A1) to load surface or wall surface (surface with area A2) can be represented as shown in Figure C.1. The view factor is equal to Eq. 90 [48] [49]
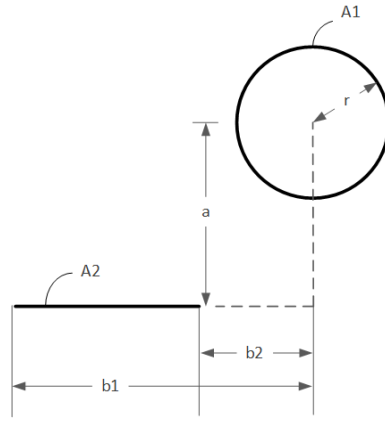


Figure C.1: Dimension for the exterior of an infinitely long cylinder to infinitely long parallel plate

$$F_{12} = \frac{1}{2\pi}(\tan^{-1}(b_1/a) + \tan^{-1}(b_2/a))$$

Eq. 90

The geometry for radiation between wall surface to load surface or between load surface to load surface can be represented as two infinitely long parallel plates (surface A1 and surface A2) as shown in Figure C.2. The view factor equation for these two surfaces is presented in Eq. 91. [50]
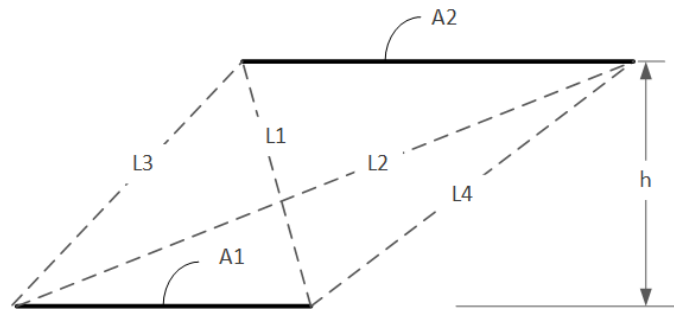
Figure C.2: Dimension for two infinitely long parallel plates

$$F_{12} = \frac{L1 + L2 - L3 - L4}{2\,A1} \qquad \text{Eq. 91}$$

# Nusselt Number Correlation

In Section 5.4.1, the heat transfer equation for the atmosphere was developed. The convective heat transfer between the atmosphere other furnace components (wall, burner, and load) were developed. A Nusselt number correlation is required to determine the convective heat transfer coefficient in Eq. 70. The Nusselt number is calculated by Eq. 92. The coefficients used in the equation are tabulated in Table D.1, and they depend on geometry and Reynolds number $Re_D$. Geometry in row 1 represent the burner, while geometry in row 2 represents wall and load.

$$\langle Nu \rangle_D = a_1 Re_D{}^{a_2} Pr^{1/3} \qquad \text{Eq. 92}$$

$Re_D$ is calculated by Eq. 94. $u_{f,\infty}$ is the fluid velocity and calculated by Eq. 71. $\nu_f$ is the kinematic viscosity of the fluid.

$$Re_D = \frac{u_{f,\infty} D}{\nu_f} \qquad \text{Eq. 93}$$

$Pr$ in Eq. 92 is Prandtl number. It is the ratio of the product of heat capacity, $c_p$, and absolute viscosity, $\mu$, to the thermal conductivity, $k$.

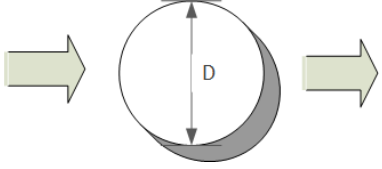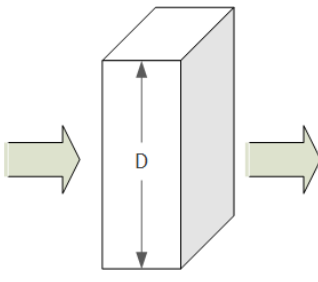$$Pr = \frac{c_p\, \mu}{k} \qquad \text{Eq. 94}$$

## Natural Convection for vertical plates [51]

In Section 5.4.1, heat loss through the wall is formulated. It considers total thermal resistance on the conductivity of wall layers and convective heat transfer from the outer wall surface to the ambient air. The latter happens through the natural convective heat transfer from the vertical wall to the ambient air. The Nusselt number is used to determine the heat transfer coefficient. It is a function of Grashof number $Gr$ and Prandlt number $Pr$.

$$Nu = \frac{hL_c}{k_f} = f(Gr, Pr) \qquad \text{Eq. 95}$$

$k_f$ is the fluid (ambient air) conductivity. $L_c$ is the characteristic length. For a vertical plate, it is equal to the height of the plate.

Table D.1: Nusselt number correlation for geometry used in this work [52]

| No | Geometry | Coefficient for Nusselt number correlation in Eq. 92. | | |
|----|----------|------|------|------|

**1**

| $a_1$ | $a_2$ | $Re_D$ |
|-------|-------|--------|
| 0.683 | 0.466 | $0 - 4 \times 10^{-3}$ |
| 0.193 | 0.618 | $4 \times 10^3 - 4 \times 10^4$ |
| 0.027 | 0.805 | $4 \times 10^4 - 4 \times 10^5$ |

**2**

| $a_1$ | $a_2$ | $Re_D$ |
|-------|-------|--------|
| 0.228 | 0.731 | $4 \times 103 - 2 \times 104$ |

For a constant temperature surface, Churchill and Chu [53] recommend the following correlation equation for a laminar only region i.e., if $Ra_L < 10^9$.

$$Nu = 0.68 + \frac{0.670\, Ra_L^{1/4}}{[1 + (0.492/Pr)^{9/16}]^{4/9}}$$ 

Eq. 96

If there are both laminar and turbulent regions, i.e., if $Ra_L > 10^9$.

$$Nu = \left(0.825 + \frac{0.387 Ra_L^{1/6}}{[1 + (0.492/Pr)^{9/16}]^{8/27}}\right)^2$$

Eq. 97

For natural convection, fluid flow is caused by density gradients in the fluid. Reynolds number is no longer relevant because the flow velocity is less significant than on forced convection. It is replaced with the Grashof number, $Gr_L$. [51]

$$Gr_L = \frac{g\,\beta(T_s - T_\infty)L^3}{v^2}$$

Eq. 98

$\beta$ is the volumetric coefficient of expansion. It is defined as

$$\beta = \frac{1}{V}\left(\frac{\partial V}{\partial T}\right)$$

Eq. 99

For ideal gases $\beta = 1/T$. For non-ideal gases and liquids, β is obtained from property tables.

# Material Properties

Table E.1: Thermal properties of burner and furnace construction material

| Properties | Unit | Cast iron | Brick, Fireclay | Stainless steel GX40CrNiSi25-20 (Nr. 1.4848) |
|---|---|---|---|---|
| Object | [-] | Loads | Walls | Burners |
| Emissivity ($\varepsilon_r$) [18] | [-] | 0.65 | 0.75 | 0.97 |
| Conductivity (k) | [W/m-K] | 42 | 1.6 (@1273 K) [36] | 23 |
| Density ($\rho$) | [kg/m3] | 7500 | 2000 | 7700 |
| Heat conductivity (cp) | [J/kg-K] | 460 | 1.1 | 630 |

Table E.2: Thermal conductivity of furnace walls

| Material | Thermal conductivity [W/m-K] |
|---|---|
| Brick, Fireclay | 1.6 (@1273 K) [36] |
| Kaolin Insulating brick | 0.45 (@1423 K) [36] |
| Glass fiber | 0.035 (@300 K) [36] |
| Steel (AISI-304) | 15 (@300K) [36] |
| Concrete | 0.93 (303 K) [36] |
| Mineral wool | 0.042 (@303K) [36] |

Table E.3: Air properties at temperature of 310 K [36]

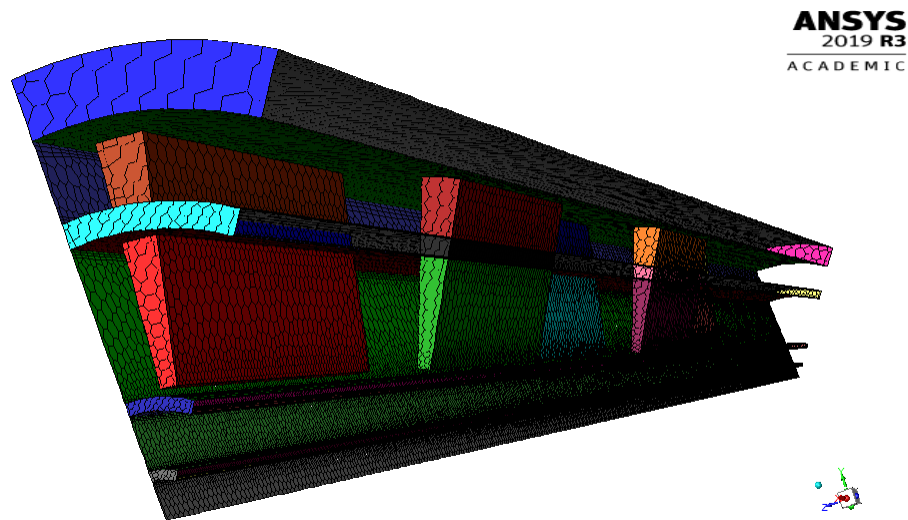| Properties | Value |
|---|---|
| Thermal conductivity (k) | 0.0274 |
| Density | 1.141 |
| Heat capacity | 1005 |
| Kinematic viscosity | $16.54 \times 10^{-6}$ |
| Pr | 0.69 |

# Extra Figures



Figure F.1 3-dimensional domain of the heat recuperation zone